UNIVERSITY OF ROME "TOR VERGATA"

FACULTY OF MECHANICAL ENGINEERING

MATERIAL ENGINEERING PHD

CYCLE XXII

Microstructural evolution after Cellular Precipitation in a high nitrogen austenitic steel

Ludovica Rovatti

A.A. 2009/2010

Tutor: Prof. Roberto Montanari

Acknowledgments

Ringrazio coloro che danno agli altri in modo gratuito,

ringrazio coloro che sanno ascoltare,

ringrazio tutti coloro che hanno permesso che raggiungessi questo traguardo..

" Sapere tante cose non insegna ad avere intelligenza "

Eraclito di Efeso 535 a.c, 475 a.c.

Introduction

The High Nitrogen stainless (HNS) steels are characterized by excellent combination of high strength and corrosion resistance.

Nitrogen in solid solution is a beneficial alloying element to increase strength level, it is also a strong austenite-stabilizing element and improves the resistance to localized corrosion.

The main industrial applications are the engineering plants (Petrochemical, Energy Generation, Paper Production) and the Biomedical field.

In some cases, like for Energy Production applications, the limit of the HNS steels is the microstructural instability: nitride precipitation occurs in the HNS in the temperature range of 500-1050 °C.

Hence it is necessary to monitor the microstructure evolution after exposition at the high temperatures.

The aim of the thesis is to analyze the changes in the mechanical properties of an austenitic HNS steels after precipitation and at the same time deepening the chemical-physical phenomena that drive the transformation process.

Index

CHAPTER 1

Background

1.1 The thermodynamics of nitrogen in the HNS

Compared to Carbon (*C*) the solubility of Nitrogen (*N*) in steel is lower in the melt but higher in the austenite, leading to somehow distinctive HNS manufacturing practices. The equilibrium content of nitrogen in pure iron, in fact, is only 0.045% (wt.%) at 1600°C and atmospheric pressure [1]. As known, the gas solubility in a pure metal depends on the temperature in accordance with the Arrhenius' law :

$$C_g = Be^{-\frac{Q}{RT}} \qquad (1.1)$$

where:
- *B* is a constant
- *R* is a Gas constant
- *T* is a Temperature (K)
- *Q* is the *Activation Energy* to introduce a mole of gas in the metal

and on the pressure following the Sievert relation:

$$C_{gas} = kP^{1/2} \qquad (1.2)$$

where *k* is a constant.

In some cases the behaviour of the solubility is no the same of the Sievert's one. For example, this occurs in the Cr steel for high pressure as shown in figure 1.1.

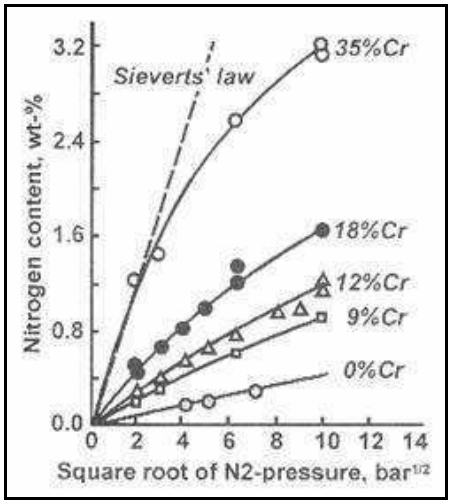

Fig.1.1 Nitrogen solubility at 1873 K **in Fe alloys vs. pressure [1]**

Conventional steel making practice at atmospheric pressure does not allow to introduce high amounts of nitrogen due to its low solubility in the melt and still lower solubility in δ ferrite, as shown in Figure 1.2, leading to nitrogen losses during solidification. Nitrogen cannot remain absorbed in steel unless during the solidification process the L → δ reaction could be suppressed.

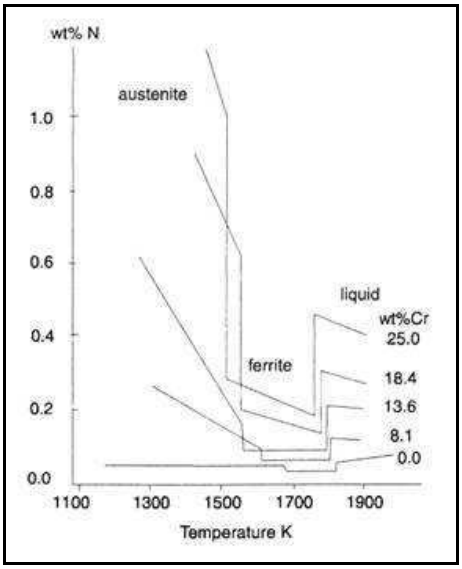

Fig,1.2 Nitrogen solubility in Fe-Cr alloys at 0.1 MPa [2]

Through the increased gas pressure (until 40 bar) and an optimized composition of the steel, the N concentration could be until 2.2 wt.% in the liquid metal (it is very close to the limit of N solubility in Fe γ at 600°C as shown in figure 1.3).

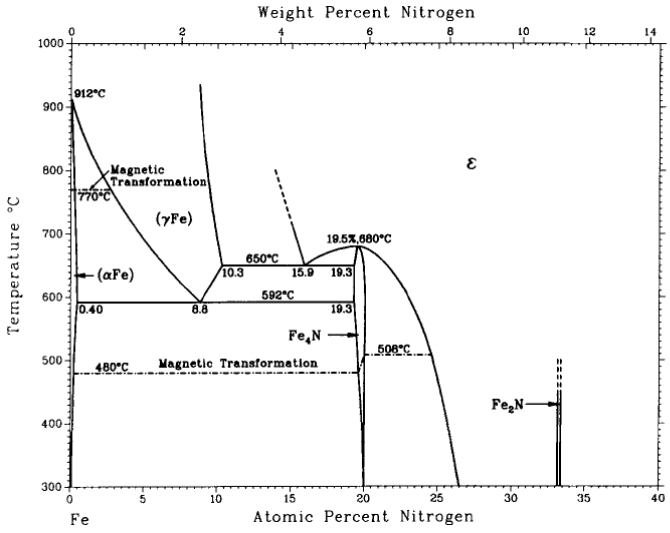

Fig.1.3 Fe-N diagram [3]

When stainless steel is exposed to a nitrogen atmosphere at high temperature, nitrogen may be incorporated in steel through dissolution in the austenitic phase up to its solubility limit, according to equation (1.3):

$$\tfrac{1}{2} N_{2\,(gas)} \Leftrightarrow [N]_{\gamma} \qquad (1.3)$$

but the high pressure can displace the reaction to the right.

Then in condition of equilibrium the reaction $\tfrac{1}{2} N_2$ (gas) $\Leftrightarrow$ [N] γ may be shifted by reactions (1.4) and (1.5) relative to CrN and Cr_2N precipitation.

$$[Cr]_{\gamma} + [N]_{\gamma} \Leftrightarrow CrN \qquad (1.4)$$

$$2[Cr]_{\gamma} + [N]_{\gamma} \Leftrightarrow Cr_2N \qquad (1.5)$$

In order to maximize the N content, elements with high affinity with nitrogen are added in the composition. These elements are **Cr** (Chromium), **Mn** (Manganese), **Mo** (Molybdenum), **V** (Vanadium) [1] that have an electron valence number lower than in iron and this produces a higher solubility of nitrogen. The elements with the contrary effect, instead, are **Co** (Cobalt), **Si** (Silicon), **Ni** (Nickel), **C** (Carbon) with a number of external electrons higher than iron.

However it's necessary to underline that the solutes that produce the highest solubility of nitrogen could cause, at the same time, the precipitation of the nitrides in particular thermal conditions.

As known the nitrogen stabilizes austenitic phase. The figure 1.4 is the modify De Long diagram.

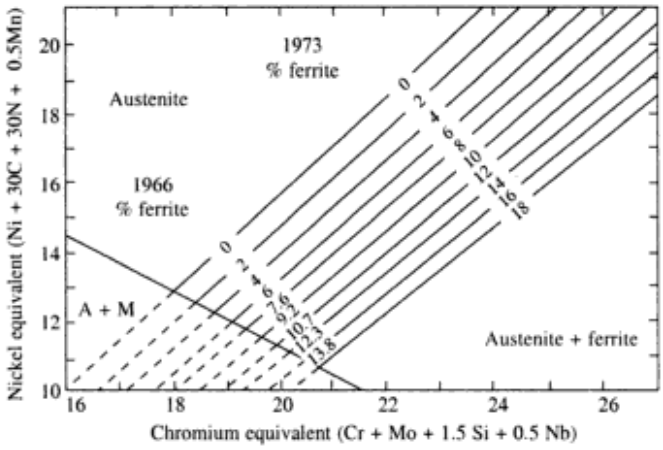

Fig.1.4 De Long diagram

In fact, at atmospheric pressure the nitrogen solubility in the ferritic steels is about 0.08% (wt.%) lower than that in the austenitic ones. In the austenitic steel with a high Nickel percentage the solubility of nitrogen is about 0.2% (wt.%), while in the austenitic steel with high content of Manganese and Chromium this limit is about 0.4 % (wt.%) [4].

1.2 Technologies of HNS steel production

The difficulty in the production of HNS with a high N content is connected to the limit of solubility of the interstitial element in the steel. Therefore, the precipitation of nitrides and the creation of voids are possible for these steel with negative results for the mechanical properties and for the subsequent mechanical workings.

The solution that usually it is adopted is the application of a high pressure in three different way [5]:

1. system with an electrode under-slag where the leakage is made in a nitrogen atmosphere through high pressure
2. Counter pressure method: in an inductive furnace in high pressure the leakage occurs through a difference of pressure between the furnace and the ingot mould
3. ESR: (“Electro Slag Remelting”): a discontinuous method that is based on the remelting of a charge derived from an induction furnace or AOD (Argon oxygen Decarburation). The charge is remelted in the ESR apparatus in a N atmosphere with the addition of nitrides composite (aluminates or silicates). As figure 1.5 shows the electrode is dipped in the electric slag that is both a conductor and a filter for the impurities. The PESR is the same technology but a very high N pressure (until 40 bar) is applied in the step of remelting. The figure 1.5 shows both the methods.

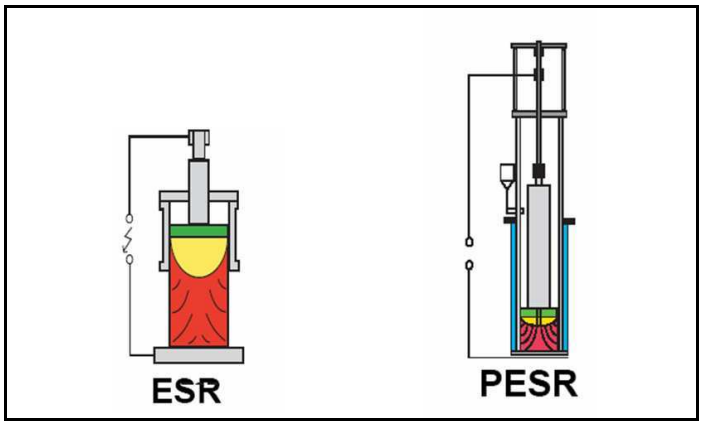

Fig.1.5 ESR and PESR production processes

Other technology, like the powder metallurgy does not use the high N pressure but obtains the required concentration through the nitrogen addition both in the solid [6] and liquid phase. In the second technology the enrichment of N is connected to the atomization of the liquid phase with nitrogen. [7]. The produced powder is sintering with the thermo-mechanical processes as extrusion, isostatic pressing at high temperature and the injection in the metallic mould of the powder with the binding. The goals of this technology of production are:

- absence of the segregation
- high homogeneity
- possibility of thermal treatment for the solubilization of any nitrides.

The PESR, however, with the powder metallurgy gets the highest nitrogen concentrations (until 1 wt. %) and it is the technology used for production of the HNS steel in the present thesis.

In fact through a correct selection of the alloy elements it is possible to rise the thermodyamic limit of solubility, in the solid phase, to 0.08 wt. % for the ferritic steels and 0.4 wt.% for the Cr-Mn austenitic ones [4].

Nowadays the main aim is to create suited and no much expensive production processes in order to extend the area of application of these steels.

1.3 Properties of the High Nitrogen Stainless steels

Nowadays the HNS steel both in the austenitic phase and in the martensitic one are studied in order to increase the already high performances that they could offer. For examples through cold working the σ_r of the HNS austenitic steels can be increased until 2000 Mpa.

One of the advantage of nitrogen is decreasing the differences between the two classes of steels: increasing the mechanical resistance of the austenitic steels and rising the corrosion resistance of the martensitic ones. The N concentration, however, is limited to 1 wt.% to avoid cleavage-like, brittle failures.

The nitrogen strengthening effect in the steel is higher than the carbon for understanding this effect are necessary to introduce some theoretical reasons. This is not result of a dimensional effect in fact the carbon has a higher atomic radius (0.91 Å) than the nitrogen (0.75 Å). By the investigation of the effect of alloying addition on the lattice parameter, in fact, it is clear that the carbon contribute to increase the reticular parameter is higher than the nitrogen one. It was observed that the reticular parameter for the HNS austenitic steel depends in a linear way on the nitrogen concentration until the precipitation [8].

The difference between nitrogen and carbon effects in austenite can not be understood in terms of elastic continuum because nitrogen and carbon atoms cause the same elastic distortions in solid solutions but the difference is in the electronic structure. The N causes the increasing of the conduction electron concentration in austenitic steel compared to carbon. This causes, for high nitrogen content, the increasing of the metallic component of the interatomic bonding solid solutions contributing to influence the mechanical properties [9]. The metallic character of the binding so creates after cold working a short range order and the dislocation planar slip and their consequent piling.

Table 1.1: SFE vs. the nitrogen content

SFE (mJ/m^2)	28	25	13	51	30
N (wt.%)	0.22	0.4	0.5	0.8	0.9

The nitrogen resistance to obstruct the dislocations is stronger than that observed for carbon and the Stacking Fault Energy (SFE) is a function of the N content: SFE decreases until 13 mJ/m^2 for a fixed composition (about 0.5 wt.%) as shown in figure 1.6 [10].

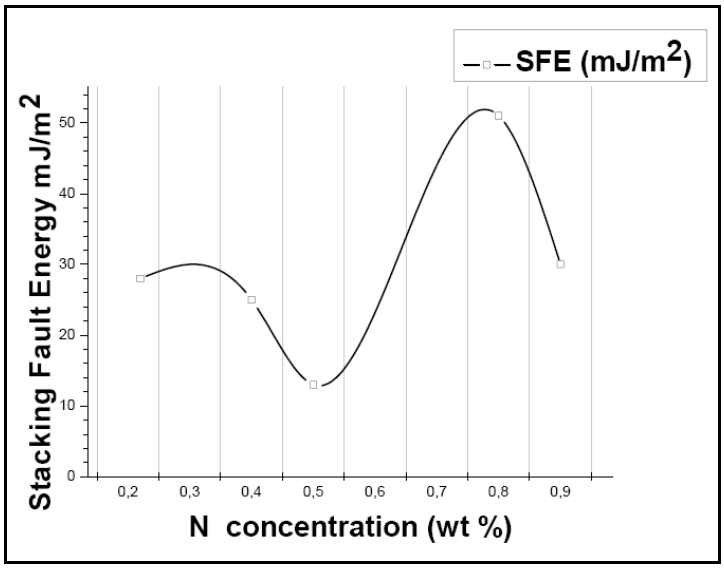

Fig.1.6 Behaviour of the SFE vs. the nitrogen concentration (wt. %)

The nitrogen influence on the stacking fault energy in FCC structure depends on different features: the interaction energy of nitrogen with stacking faults, the interaction energy of nitrogen with substitutional alloying elements in solid solution and the concentration of substitutional alloying elements in solid solution.

For examples alloying with Cr and Mn decreases the density of states at the Fermi level and this increases the SFE, whereas Ni decreases SFE as shown in figure 1.7 [11].

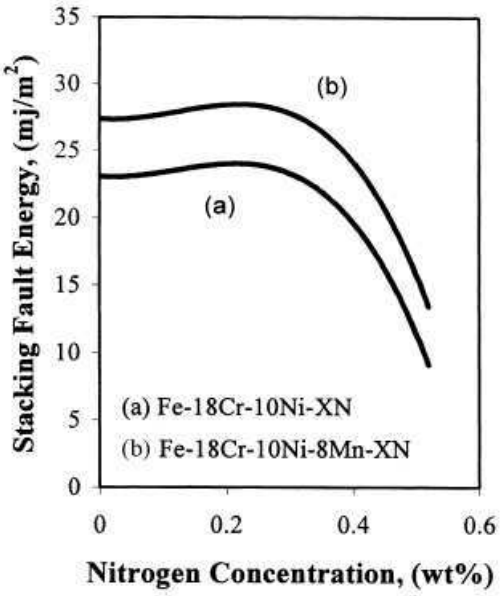

Fig.1.7 SFE vs. N concentration for Cr-Ni-Fe alloys and Cr-Mn-Fe alloys

About corrosion properties it was observed [12] that these steels have good tense-corrosion and pitting corrosion resistance also in aggressive environment as in the presence of chlorides.

The reasons of this behaviour can be connected probably to the screen effect of the interstitial nitrogen against the external agents or to the formation of some ions as NH_4^+ that contribute to the ripassivation where pits are formed [13].

The ”Pitting Resistance Equivalent Number”, PREN of same HNS superaustenitic and duplex steels (table 1.2) is higher than **40** in agreement with the relation (1.6) [14]:

$$PREN = \%\,Cr + 3.3\,\%Mo + \mathbf{16}\,\mathbf{\%N} \qquad (1.6)$$

It is known that nitrogen also is a γ–stabilizer (without the necessity of the addition of Ni) and this contributes to obstruct the formation of intermetallic phases and precipitates even if the secondary phases precipitation could occur when the material is heated or worked.

In the following paragraphs the properties of the different HNS steels will be illustrated and in which way the intermetallic and secondary phases precipitate in the HNS steels.

1.3.1 HNS martensitic steels

HNS martensitic steels are used when are necessary high mechanical properties (at low and high temperatures) and great tribological features. There are numerous martensitic steels with high creep properties and fatigue resistance for the fine and omogeneous distribution of carbides in the martensitic structure [13]. In fact these steels are studied, for example, in substitution of the traditional ones in the spatial applications.
In this case the necessary features are :

- a good subsurface rolling contact fatigue resistance
- sufficient mechanical properties at the temperature of liquid hydrogen (embrittlement risks at 20K)
- a good resistance to oxidation (condensation, possibility of storage without protective oil during several years)
- compatibility as good as possible with the temperature of surface coating processings
- an excellent dimensional stability (in relation with the presence of retained austenite)
- a fine structure free from large carbides and carbide segregation (for corrosion resistance and fatigue life).

In a recent research for the rings and bearing of the liquid hydrogen turbopumps where are used the type X45CrMoV15-2 martensitic steel in spite of X105CrMo17 (AISI 440C) [16].
The results of the study had verified the better results of the HNS steel. In the AISI 440C steel with a high percentage of carbon the precipitation of carbides (size > 10 μm) causes reducing in the corrosion resistance and limiting in the hardening.
On the contrary, the high nitrogen martensitic steel type X45CrMoV15-2 was observed to have less and smaller carbides than the other steel. After high temperature tempering, the microstructure nitrides nanoprecipitates (VC-VN-CrN) a few nm in size have been identified.
For these properties the HNS steels can be used in a wide range of applications like energy production, gas and vapour turbines and are materials adapt to realization of the spherical bearings. There are two other important type of martensitic steels used for the bearings: CRONIDUR 30 (15% Cr, 1% Mo, 0.3% C e 0.4% N) and Bohler. The first

has a cycle-life of five times higher than the M50 (with 15 % Cr) and high corrosion resistance [15].

CONDUR 30 for its toughness results unaffected to the plastic deformations made by the impurities that stay between the contact point and the volvent point (fig. 1.8). The Bohler can be adapted also with low variation of Chromium percentage to different applications: glass manufacturing (13%), plastic fabrication (17%) and cold plastic deformation (15%) [12].

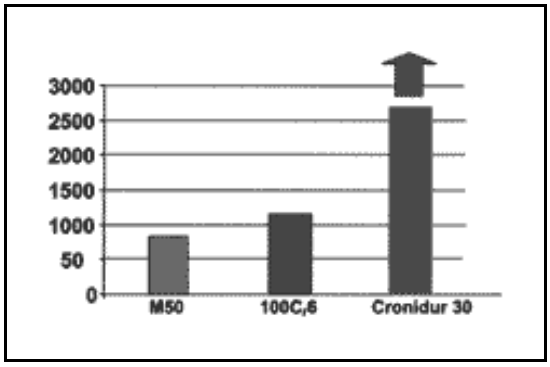

Fig.1.8 Comparison between the fatigue cycle-life for the bearings of: Cronidur 30 ,M50 and 100Cr6, stressed in the same way (superficial tension of 2800 N/mm^2) in a optimal lubrication elastic-dynamic regime [15]

Fig. 1.9 A bearing

The corrosion resistance is higher than in the traditional steels, in particular the uniform and SCC corrosion.

1.3.2 HNS austenitic steels

The HNS austenitic is one of the most used high nitrogen stainless steel for the high mechanical and corrosion performances.

Nitrogen has in the γ-iron a high solubility and induce a straightening for solid solution in the octahedral positions of the austenitic lattice. The relation (1.7) [17]:

$$a(nm) = 0.3578 + 0.00006Cr + 0.000095Mn + 0.0033C + 0.0029N \ \text{(wt.\%)} \qquad (1.7)$$

connect the γ cell parameter to the composition of the steel.

This expression is applicable to the steels which contain Cr, Mn, C and N as alloying elements.

Note that the coefficient of N in the expression is 0.0029, really, this value was obtained for high nitrogen content (about 0.6 wt. %), for lower content (< 0.3 wt. %) in these steel the coefficient was calculated around 0.0022.

To the nitrogen content is connected the stability of the γ iron as it is shown from the Shaeffler diagram (fig. 1.4) and the NE (*Nichel Equivalent*) parameter [18] (1.8) :

$$NE = \%Ni + 30\ \%C + 25\ \%N + 0.5\ \%Mn + 0.3\ \%Cu \qquad (1.8)$$

The yield stress for the austenitic steels at the ambient temperature depends linearly on the nitrogen concentration with a thermical component proportional to $C_N^{\frac{1}{2}}$ [13]. If the steel is alloyed with 0.5 wt.% of nitrogen, the σ_y is about 3 times as high as standard steel Cr18Ni10 (550 MPa against 250 MPa). The main properties of these steels are the high plastic deformation (at least up to 0.5 wt.% the cold workability of austenitic HNS steels has been adequate), low magnetic permeability and the high N content stabilizing γ austenite, the martensite formation can be prevented entirely [13].

These characteristics are necessary in applications where are required high dimensional tolerance and no ferromagnetic materials.

Other features of these steels as for the duplex ones are high SCC corrosion resistance, the decreasing of the time of precipitation of intermetallic phase σ, η, R, χ (nitrogen has not a high solubility in these phases) [13].

The austenitic steels, however, have the following limits: microstructural instability in fixed temperature range, restricted thermal fatigue properties (for a high thermal

dilatation coefficient), welding problems that give lower possibilities than the martenisitic ones for application in high temperature.

The problem of the precipitation of secondary phases and nitrides was widely studied in this research.

During the processing or the exposition at high temperature there are the possible formation of the following phases [19]:

1- Intermetallic phases (σ in the range 800 -900 °C), carbide, nitrides precipitation
2- martensitic phase formation at cryogenic temperatures
3- ferrite δ formation at high temperature

For the hot lamination it was observed that it is negative the formation of δ phase and in particular that this is connected to the Chromium content (that stabilizes α phase). In fact as shown in the figure 1.10 the heavy cracks decrease with lower content of Cr [20].

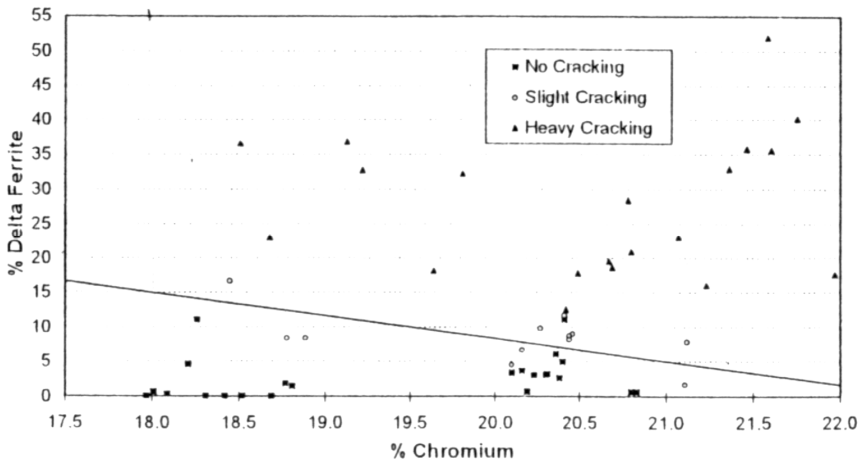

Fig.1.10 Concentration of δ iron vs. Cr content in the CROMANITE steel [21]

An element that it is seen to decrease the hot brittleness in the hot deformations is the B. The optimal concentration is 0.003- 0.006 % where it was observed a diminution of intergranular cracks [22]. In figure 1.11 there is the CSI index of severity of the cracks.

For higher concentration there is the formation of eutectic boride.

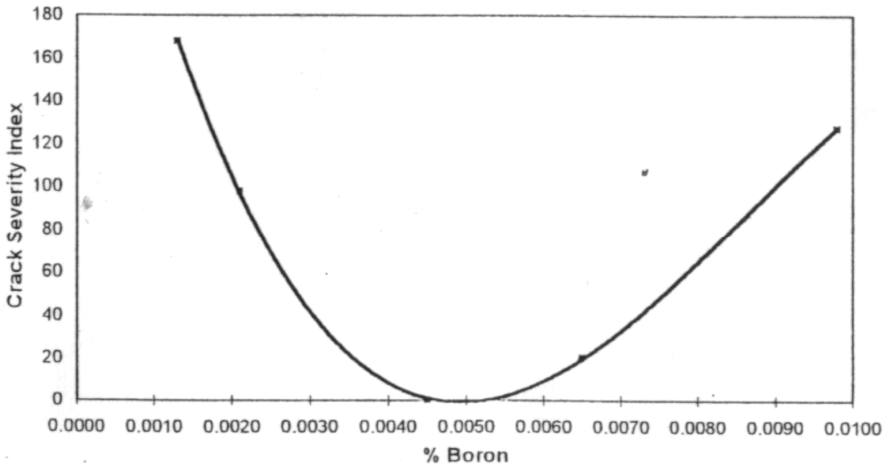

Fig.1.11 Changing of CSI with the B concentration [20]

The applications of these steels in the industrial field are different like the biomedical one for the low Ni content necessary in these steels for the higher biocompatibility than the conventional stainless steels (AISI 316L, AISI 316 LN etc..).

In the transport and storage field the CROMANITE (0.5% N, 0.05% C, 10 % Mn, 19 % Cr) was used for the properties as: high corrosion and tribology properties. Some austenitic steels produced by PESR reach a nitrogen content of 0.9% and so after cold deformation the yeld stress is also 2000 Mpa with a high pitting corrosion resistance. An example of a HNS commercial steel with high mechanical properties is the Bohler P558 (0.6 wt.% N, σ_R of about 2000 MPa after cold working): its properties are comparable with the Co alloys.

Another class of these steel is used in the industrial applications, the superaustenitic steels. They contain high percentage of Ni (N 0.2 - 0.5 wt.%) and these steels are characterized by a high pitting resistance corrosion.

Table 1.2. Superaustenitic steels [12]

Lega	C_{max}	Mn	Cr	Ni	Mo	Cu	N	Altri	PRE	EN	UNS	Marchio commerciale
304	0.08		18	9					18	1.4301	S30400	
316L	0.03		17	12	2				24	1.4404	S31603	
Lega 20	0.05		20	30	2.5	3.5			32	–	–	
20 Cb-3	0.06		20	34	2.5	3.5		Nb, Ta	32	–	N08020	Carpenter Technology
B6, 904L	0.02		20	25	4.5	1.5			35	1.4539	N08904	
Sanicro 28	0.02		27	31	3.5	1			39	1.4563	N08028	Sandvik
NSCD	0.03		17	16	5.5	2.5			35	–	–	Ugine
AL-6X	0.03		20	25	6				40	–	N08366	Allegheny Ludlum
AL-6XN	0.03		20.5	24	6.3		0.22		45	–	N08367	Allegheny Ludlum
1.4439	0.03		17	14	4		0.15		33	1.4439	S31726	
2RE69	0.02		25	22	2		0.12		37	1.4466	S31050	Sandvik
ASN 7W	0.04		18	16	7	2	0.15		43	–	–	Böhler
VEW 963	0.03		17	16	6.3	1.6	0.15		40	–	–	VEW
Antinit 3974	0.03	6	23	17	3		0.40	0.2Nb	39	–	–	Thyssen
254 SMO	0.02		20	18	6.1	0.7	0.2		43	1.4547	S31254	Avesta Sheffield
1925hMo	0.02		20	25	6.2	0.7	0.2		44	1.4529	N08925	VDM
SX	0.02		17.5	20	1	2		5 Si	21	–	S32615	Sandvik
Lega 31	0.02		27	31	6.5	1.2	0.2		52	1.4562	N08031	VDM
934LN	0.02	10	20	15	4.5		0.40		41	–	–	
1.4565	0.03	6	24	18	4.5		0.4		45	1.4565	S34565	
654 SMO	0.02	3	24	22	7.3	0.5	0.5		56	1.4652	S32654	Avesta Sheffield

1.3.3 HNS duplex steel

The high nitrogen duplex steels would be applicable to a wider range of applications than the austenitic ones. The main properties that characterize these steel are the fatigue resistance and the SCC corrosion resistance and the easier welding. In fact N in the welded zone stabilizes the austenitic phase and keeps the ratio between the two phases.
The PREN reaches the value of 40 for the high presence of the Cr and Mo in the ferritic phase [16]. The main industrial applications are the petrolchemical, chemical, food, naval and paper industy. In the offshore field the duplex HNS have similar properties to the superaustenitic ones but the first are cheaper and with higher properties than the others.
The composition of some commercial steels are presented in table 1.3 .The content of nitrogen is not higher than 0.3 wt.% but a lower content of Ni than the commercial austenitic stainless steel.

Table 1.3. Some duplex HNS steel [18]

European and American Nomenclature	Cr	Ni	Mo	N	Altri	PREN
X2CrNi 23-4 - EN 1.4362	22÷24	3,5÷5,5	0,1÷0,6	0,05÷0,2	Cu: 0,1÷0,6	25
X2CrNiMoN 22-5-3 EN 1.4462	21÷23	4,5÷6,5	2,5÷3,5	0,1÷0,22	÷	32÷34
X2CrNiMoCuN 25-6-3 - EN 1.4507	24÷26	5,5÷7,5	2,7÷4	0,15÷0,3	Cu: 1÷2,5	
X2CrNiMoN 25-7-4 - EN 1.4410	24÷26	6÷8	3÷4,5	0,2÷0,35	-	>40
X2CrNiMoCuWN 25-7-4 - EN 1.4501	24÷26	6÷8	3,4	0,2÷0,3	Cu: 0,5÷1 W: 0,5÷1	

The limit in the production of these steels is the possible segregation of nitrogen in the ferritic phase and so there is the necessity to increase the Mn content.

An example of a steel without Ni is RelyNite (21% Cr, 7% Mn, 0.07%C e 0.35 N), used, for example, in the South of Africa in the substitution of the commercial steel both for the cost of Ni and for the necessity of treated treatment in order to have high performance [12].

1.4 Precipitation of secondary phases

1.4.1 The Continuous and Discontinuous precipitation

When an element is in solid solution in a matrix it has a thermodynamic solubility. If at a specific temperature the solute concentration is upper than this limit, the precipitation of second phases could occur.

The possible precipitation that can be observed are: the **continuous** precipitation and the **discontinuous** one.

The continuous precipitation can be illustrated by the reference of the transformation of Fe-C alloy. Many general principles, in fact, are analogues in the systems without the precipitation of transition phases. In this type of precipitation the most important nucleation sites of the equilibrium phases are grain boundaries and the interface between matrix and inclusions.

The parameters that influence the precipitation are:

1- The undercooling velocity

The morphology of the precipitates is influenced by the amplitude of undercooling under the curve A3. In particular for small gap of temperature equiaxed morphologies were obtained or grain-boundary allotriomorphs. On the contrary for higher ranges the precipitates are plate-like (Widmanstatten plates) with a particular crystallographic orientations and with finer structures and characterized by smaller distances between plates at lower temperatures.

2- The austenitic dimension grain

The grain dimension influences the sites of nucleation of the precipitates. In particular in the smallest grains the nucleation of the equilibrium precipitates occurs in the grain boundary because carbon is rejected inside the grain, it is easily the precipitation of Widmanstatten plates. In the inner part of a grain the preferential sites of nucleation of precipitates are the inclusions and the dislocations.

In some systems for definite temperature ranges the grain precipitation doesn't occur in allotriomorphs or Widmanstatten side-plates but in a discontinuous way [23].

This type of precipitation is known as cellular precipitation and the main feature is that the precipitation front moves with the growing of the precipitates.

The difference between cellular precipitation and the continuous one is that in the first there is a discontinuous change of the composition of matrix at the interface between cell and matrix, in the second one the homogeneous distribution of the precipitates decreases the supersaturation of the matrix continuously in the increasing time of treatment.

The cellular precipitation is like to the eutectoidic one. The structure of the precipitates, in fact, is discontinuous with alternate lamellae and secondary phases.

The feature of the cellular precipitation is that the secondary phase has the same reticule of the primary phase but with a lower content of nitrogen.

The reaction that describes this phenomenon is:

$$\alpha' \rightarrow \alpha + \theta \qquad (1.9)$$

where:

- α' is the supersaturated matrix
- α is the secondary phase
- θ is the equilibrium precipitate

The cellular precipitation is observed only in some metallic systems, in specific ranges of temperature and the reasons are not so clear. In particular, there are two relationship that describe the migration rate of the front of the cells related to the solute diffusion with two characteristic equations: Zener and Turnbull relations. The first is connected to the volume diffusion:

$$G = \frac{k_1 D_v}{S} \qquad (1.10)$$

- G is the migration rate of the cell front
- S is the interlamellar spaces between the precipitates in the cell
- D_v is the volume coefficient of diffusion of solute atoms

the second is referred to the intergranular one :

$$G = \frac{k_2 D_B}{S^2}\delta \qquad (1.11)$$

- δ is the dimension of the grain boundary where the solute atoms diffuse

- k_1,k_2 are the constant that depend on the chemical composition of the phases involved in the precipitation

In general the grain boundary diffusion is observed at lower temperature while the intragranular one is visible at higher temperature.

In the substitutional binary systems Pb-Sn, Fe-Sn and Al-Mg, in particular, the features can be summarized in this way:

- the migration rate of the cell boundaries is constant for increasing time of treatment: precipitation with steady growth.
- the composition of the supersatured matrix is constant during the precipitation and the transformation is complete (100 %) involving all the original matrix.

From the relationships (1.10) and (1.11) it is clear that if the interlamellar spaces in the cells are not modified the migration rate of cell boundaries is constant.

In the substitutional system Mg-Al, for examples (equilibrium precipitates: $Mg_{17}Al_{12}$) the cell front of precipitation represents a discontinuous point of the chemical composition. This result points out that the migration occurs in the grain boundaries.

In other alloys, on the contrary, as for the HNS steels, it was observed an intragranular diffusion and not-steady growth precipitation.

1.4.2 Precipitation in the austenitic HNS steels

The precipitation behaviour has been regarded as one of the most important features of HNS stainless steels (as the material studied in thesis), because their mechanical and corrosion properties are profoundly dependent on the formation of the second phases.

Precipitation characteristics, however, have been considered to be very complicated for:

(1) small changes in the chemical composition, thermo-mechanical processing, and aging conditions can significantly influence the formation of second phases;

(2) it is not easy to distinguish one type of precipitate from another only by their morphologies

(3) the crystallographic features of some precipitates are still controversial issues.

Nitrogen has a strong effect on the properties of steels, in particular it induces solid solution strengthening and stabilizes austenite but there is a problem connecting to the precipitation of chromium nitrides in the temperature range of 500 - 1050 °C. Really in this range the precipitation does not occur at the same way: in the range of 700-900

°C the austenitic steels Cr-Ni-N and Cr-Mn-N present cellular precipitation, on the contrary, in the lower and upper ranges the steels are characterized by a continuous precipitation.

For the Cr-Mn austenitic HNS steels the precipitation kinetics is highest at 850 °C: at lower temperatures it is limited by diffusion, at higher temperatures by Recrystallization (fig. 1.12) [24].

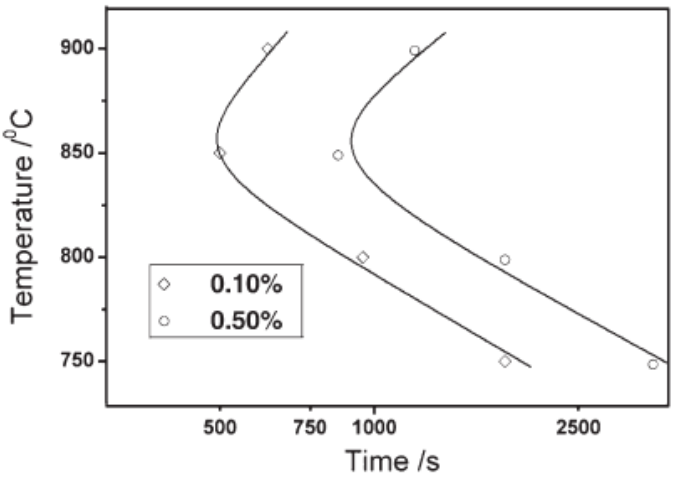

Fig. 1.12 TTP curves of nitride precipitation in a HNS steel Fe–24Mn–18Cr–3Ni–0.62N [24]

In the HNS steels the main precipitates that were observed are the **β hexagonal Cr_2N** (table 1.4).

Table 1.4. Crystallographic data on the secondary phases

Phase	Crystal Structure	Space Group	Lattice parameter (nm)	Orientation Relationship
Cr_2N	*trigonal*	$P\bar{3}1m$	$a = 0.4796$ $c = 0.4470$	$[011]_\gamma // [\bar{1}100]_{Cr_2N}$ $(1\bar{1}1)_\gamma // (0001)_{Cr_2N}$
Sigma (σ)	*bct*	$P4_2/mnm$	$a = 0.8799$ $c = 0.4544$	none
Chi (χ)	*bcc*	$I\bar{4}3m$	$a = 0.8920$	*Kurdjumov–Sachs*
M_7C_3	*orthorhombic*	*Pnma*	$a = 0.4526$ $b = 0.7010$ $c = 1.2142$	$[110]_\gamma // [101]_{M_7C_3}$ $[\bar{1}11]_\gamma // [\bar{1}31]_{M_7C_3}$

The Chromium nitrides precipitate generally along the grain boundary with a thin lenticular shape as shown in figure 1.13 .

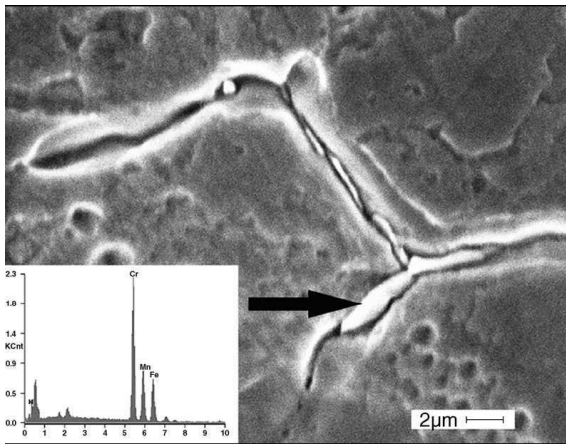

Fig. 1.13 Chromium nitrides at the grain boundary [24]

For the temperature range 700-1000 °C cellular precipitation occurs in HNS steels the precipitates are carbo-nitrides (for simplifying indicated as Cr_2N) and a secondary austenitic phase γ with lower nitrogen content than the γ_S one.

The transformation $\gamma_S \rightarrow \gamma + Cr_2N$ for high nitrogen austenitic steels are described in the following [23].

1. **Temperatures above 950 °C:** mainly coarse grain-boundary (intergranular) Cr_2N

At the highest temperature of 1000 °C, the coarse plate-like precipitates formed along grain boundaries and no cellular precipitation of Cr_2N occurred, which was presumably due to the higher nitrogen solubility at this temperature and the faster growth rate along grain boundaries.

2. **Precipitation in the nose-temperature region (between 800 °C and 900 °C)** nose-temperature region: intergranular $Cr_2N \rightarrow$ cellular $Cr_2N \rightarrow$ intragranular Cr_2N + sigma (σ);

In this temperature range cellular precipitation of Cr_2N (exactly M_2X-type (M = Cr, Mo, Fe, Mn; X = N, C) nitride, simply designated as Cr_2N) was observed after isothermal aging.

Other phases was been observed in this range: the σ phase also precipitated along the grain and in the inner grains on prolonged aging. The morphology of the σ was a coarse

and irregular blocky shape with darker contrast compared to Cr_2N, and the mean size as well as the volume fraction of σ increased with aging time.

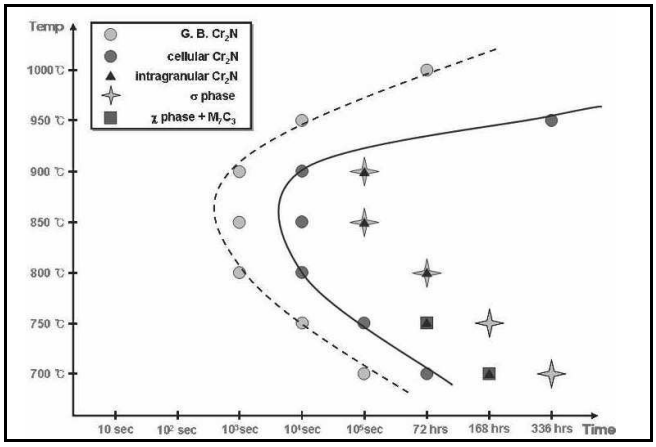

Fig.1.14 TTP diagram of the second phases for a Fe-18Cr-18Mn-2Mo-0.9N steel [23]

The formation of σ phase could be explained by the mechanism that the formation of nitrogen-depleted zone near Cr_2N induced nucleation of σ phase. In fact the σ -phase formation has been reported to occur in γ near the chromium nitride.

3. **Precipitation in low-temperature region (below 750 °C), low-temperature region (below 750 °C):** intergranular Cr_2N→ cellular Cr_2N→ intragranular Cr_2N + σ + χ + M_7C_3 carbide

In this range is reported in scientific literature that after long period aging (above 150 hours) there were a lot of intragranular precipitates identified intragranular Cr_2N with longitudinal rod shape, intermetallic χ phase with an irregular size and morphology; and fine needle-like M_7C_3 carbides.

The formation of carbides is favourite in this range of temperature that it is known as *range of sensitization* of the austenitic steels. The carbides will precipitate, as for the nitrides, if the C content is higher then the limit of thermodynamic solubility. In the austenitic steels this limit it is described by the relation, (1.12) [27]:

$$\log(C)_{ppm} = 7.71 - 6272/T \qquad (1.12)$$

with temperature in K.

In particular (fig. 1.15) at low temperature the C solubility is not much upper then 0.02 wt.% .

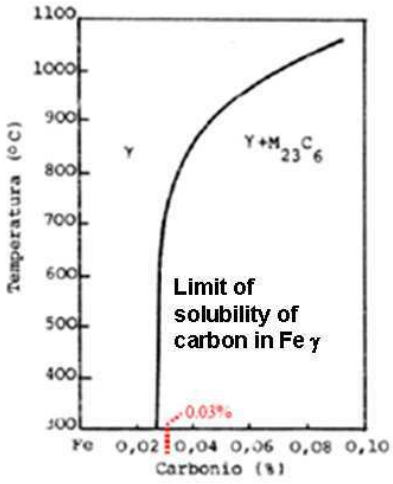

Fig.1.15 Solubility limit of carbon in Fe γ (Fe- Cr (18%)- Ni (8%)) [27]

1.4.3 The "stabilization" of HNS steels

The property deterioration in the aging temperature range (550 to 920°C) is a serious aspect that limits the use of HNS steels for high temperature applications. Hence, alloy designing should aim at development of alloying components that either suppresses the detrimental precipitation or alter the precipitation morphology so that the associated properties damages are contained. The choice of alloying elements for altering the Cr_2N type of precipitation is very limited because most elements form stable carbides or nitrides. Thermodynamic analysis of solubility product of carbides and nitrides in the Fe–Cr–Mn–N austenite could give an idea about the choice of alloying elements (fig. 1.16).

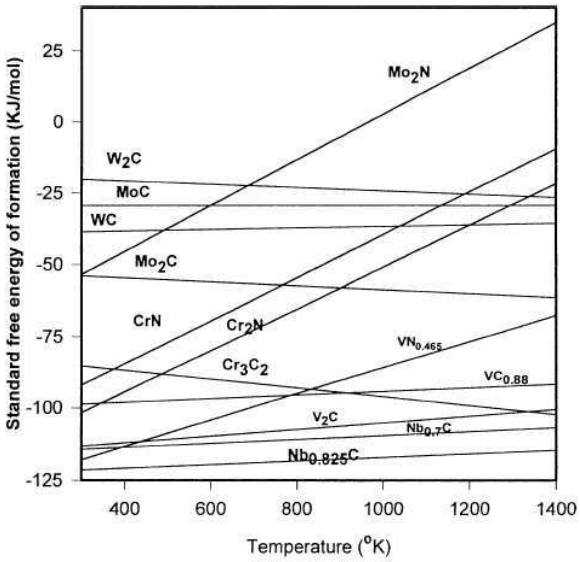

Fig.1.16 Carbides and nitrides free energies of formation vs. temperature[28]

However, the non-availability of solution thermodynamic data restricts precise calculations. In spite of this, an approximation may be arrived from analysis of standard free energy of formation of the various carbides and nitrides as a function of temperature. There are many stable carbide and nitride formers with very high negative free energy of formation. They include TiC, ZrC, VC, TaN, Ta2N, Nb2C ZrN, TiN, $Cr_{23}C_6$ *etc*.. So the possibility of contrasting the formation of the Cr_2N is in the stabilization with alloy elements that have high affinity with nitrogen.

Microadditions of V and Nb have been reported to form carbo-nitride precipitates transgranularly and though they reduced N available for forming lamellar Cr_2N precipitation and retarded it.

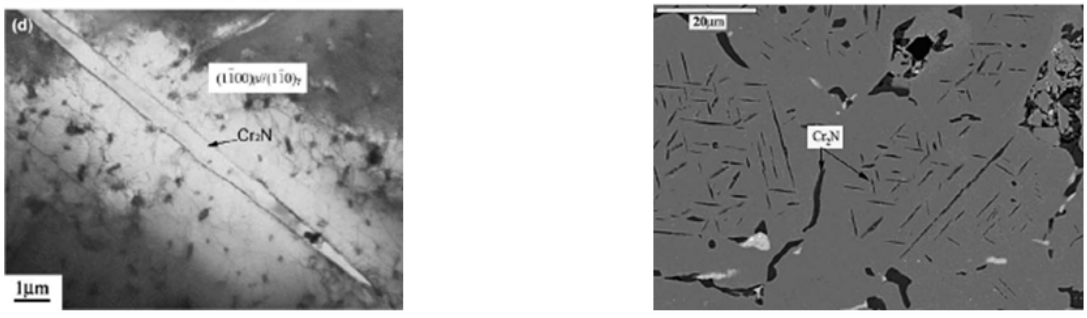

a) ***b)***

Fig. 1.17 Material (type 347 austenitic stainless steels) creep deformed at 800 °C/77.782 h. Micrograph obtained using back scattered electrons showing precipitate distribution in the surface region, b) [29]

An example of the effect of adding Nb it is observed in figure 1.17 that shows a fine distribution of Cr_2N of a HNS stabilized with Nb after long-term heat treatment and creep in air at 700 and 800 °C

1.4.4 Simulation of the kinetic precipitation

The thermo-stability of Fe–Mn–Cr–N series steels, in particular with high manganese content, is rarely reported, and attempts to building a mathematical model are scarce, which is very useful to predict precipitation behaviour for a material of given composition at specific temperature.

A mathematical model of β Cr_2N precipitation dynamics was established by Q.X. Dai et al.[30],and meanwhile proof-tested by the BP artificial neural network.

Alloying element such as Mn, Cr, Ni, N, C, Mo, V and *T* (temperature) are defined as input data and *t* (time, i.e. *t*s) as output. Contents (in wt.%) of each element range as follows: Mn, 1–35; Cr, 12–25; Ni, 0–25; N, 0.05–1.2; C, 0–0.1; Mo, 0–10; V, 0–0.5. *T* ranges from 900 to 1300 K; and *t* from 0 to 1000 min.

The relation was obtained assuming the driving force of the process as the critical ΔG^* before and after the precipitation and it could represent an useful instrumentation for calculating the starting time of precipitation in the HNS steels.

$$\ln t_s = a_0 + \frac{a_1}{1348 - T} + \frac{a_2}{T} + a_3 \frac{Mn}{T} + a_4 \frac{Cr}{T} + a_5 \frac{Ni}{T} + a_6 \frac{(1.2N + C)}{T} + a_7 \frac{Mo}{T} + a_8 \frac{V}{T} \tag{1.13}$$

where alloying element content is in wt.%; the coefficient of N is 1.2 ;T is the Kelvin temperature; *t*s the incubation period of Cr_2N precipitation, which is measured in minutes from the time when the isothermal aging began to the point when 0.5–1.0 vol.% of Cr_2N precipitated along grain boundary.

1.4.5 Intermetallic phases

At high-temperature exposure in the range between 700 °C and 1000 °C also HNS austenitic stainless steels are prone to formation of second phases. Typical second phases are known to be intermetallic phases: sigma (σ) and chi (χ) and different types of carbides such as $M_{23}C_6$, M_6C, and MC.

The main intermetallic phases that can appear in the austenitic steels are listed in the table 1.5.

Table 1.5 . Crystal structure of the intermetallic phases in the austenitic steels [31]

Phase	Unit cell	Atoms per cell	Space group	Lattice parameters (nm)	Composition	Occurrence
Sigma (σ)	bct	30	$P4_2/mnm$	a = 0.87-0.92 c = 0.4554-0.48	$(Fe,Ni)_x(Cr,Mo)_y$	AISI 304; AISI 304L; AISI 316; AISI 316L; AISI 321; AISI 347
Chi (χ)	bcc	58	I43m	a = 0.881-0.895	$(Fe,Ni)_{36}Cr_{12}Mo_{10}$	AISI 316; AISI 316L; AISI 321
Laves (η)	hex.	12	$P6_3/mmc$	a = 0.473-0.483 c = 0.772-0.786	Fe_2Mo; Fe_2Nb; Fe_2Ta; Fe_2Ti; Fe_2W	AISI 316; AISI 316L; AISI 321; AISI 347
G	fcc	116	Fd3m	a = 1.115-1.120	$Ni_{16}Nb_6Si_7$; $Ni_{16}Ti_6Si_7$; $(Ni,Fe,Cr)_{16}(Nb,Ti)_6Si_7$	AISI 308; AISI 310S; AISI 329; Fe-20Cr-25Ni-Nb
R	hex.	53 (159)	R3	a = 1.090; c = 1.934	$Fe_{22}Mo_{18}Cr_{13}$; $(Fe,Ni)_{10}Cr_5Mo_3Si_2$	Duplex Fe-22Cr-8Ni-3Mo; Superaustenitic UNS S32654; Maraging Fe-12Cr-9Ni-4Mo
Mu (μ)	rhomboh edral	13	R3m	a = 0.4762; c = 2.5015	$(Fe,Co)_7(Mo,W)_6$; $(Cr,Fe)_7(Mo)_2(Cr,Fe,Mo)_4$	Fe-17Cr-14Ni-6W; Fe-15Cr-40Ni-4W-2Mo-Al-Ti
γ'	fcc	4	Pm3m	a = 0.3565-0.3601	$(Ni,Co,Fe,Cr)_3(Al,Ti)$	Incoloy 800 and alloy A-286
γ''	bct	8	$P4_2/mnm$ I4/mmm	a = 0.3624; c = 0.7406	Ni_3Nb	Inconel 718
η	hex.	8	$P6_3/mmc$	a = 0.5109; c = 0.8299	Ni_3Ti	Overaged Incoloy 800 and alloy A-286
δ	orthorom bic	8	Pmmn	a = 0.5116 b = 0.4259 c = 0.4565	Ni_3Nb	Overaged Inconel 718

1.4.5.1 The properties and precipitation of the σ phase in HNS steels

The sigma is an intermetallic, not magnetizable [32] and brittle phase (with high hardness) of Fe-Cr (Mo) that is observed in the austenitic, ferritic, and ferritic–austenitic stainless steels after ageing in the range of temperatures 500-800 °C. The highest kinetics of transformation is at the temperature of about 850 °C [23].

Being an intermetallic phase σ exhibits not only metallic bonds, but also a high covalent bond share, therefore its mechanical properties display ceramic characteristics. It is important to know the type of bonds because it influences the chemical-physical properties of the material. In fact this phase has a higher hardness than iron [33] and has a different electrochemical behaviour. In scientific literature it was observed that the phase dissolve electrolytically depending on the potential condition and the solution used for the extraction of the phase. In particular condition of electrolytical dissolution: 3.6 N of H_2SO_4 and 0.1N of NH_4SCN in a specific range of potential (between -55mV and - 140mV), the phase doesn't dissolve as it can be observed in figure 1.18 [34], on the contrary, it is necessary just 1 hour for the σ phase dissolution in the 10 % HCl in methanol solution.

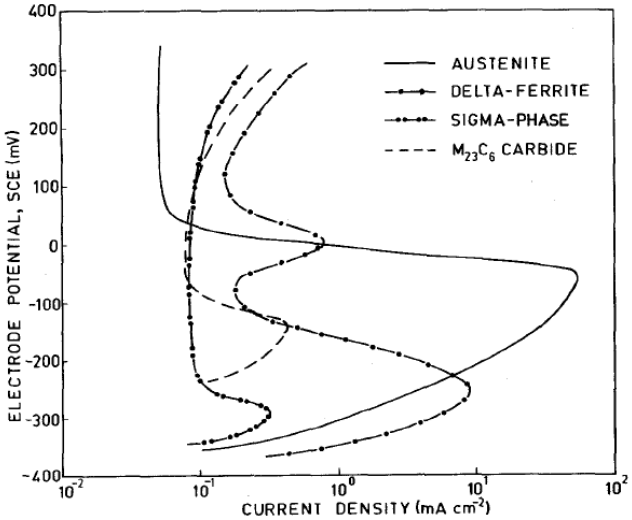

Fig.1.18 Anodic polarization curves in 3.6N H_2SO_4 containing 0.1 M NH_4SCN

The alloy element that contribute to the formation of these phases are for example Cr, Mo, Si, Mn, Si, Mo and W that increase the range of σ existence, on the contrary C and N have an opposite effect. Nitrogen has the property to obstruct the formation of the

intermetallic phases but it is only correct for the presence of N in interstitial sites in iron.

The cold and hot mechanical stresses have also the effect to promote the σ precipitation. The aspect that is not so clear is the way of nucleation of this phase. In the case of duplex stainless steels precipitation the precipitation starts at the γ/α interface and moves into the ferrite grain and may be completed within a few hours and consumes nearly all ferrite of the microstructure. Precipitation in this case can be represented by a eutectoid type reaction: $\alpha \rightarrow \gamma' + \sigma$ where γ'' is known as new austenite.

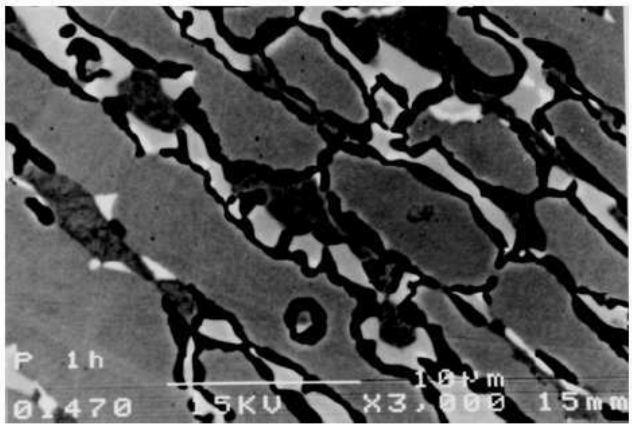

Fig.1.19 Localized corrosion in the interface of austenite/ sigma phases in the AV2205 steel treated 1 h at 850 °C after potenzidynamic cyclic test, SEM primary electrons [25]

In the austenitic steel some authors propose that the precipitation occurs directly from austenite but after precipitation of carbides.

For a high nitrogen austenitic steel (0.9% N, 18 %Cr, 19 %Mn, 0.06 %C in wt. %) was been observed the formation of the sigma phase also directly by the austenite for the heat treatment above 800 °C probably connected to the nitrides precipitation.

In the case of an austenitic HNS the crystallographic structure that was been observed is the tetragonal one with the parameters: c=0.4555nm, a=b=0.88 nm and the chemical composition is $Fe_{0.5}Cr_{0.33}Mn_{0.17}$.

The mechanism of the nucleation is not so clear. However some properties were pointed out [35]:

- the nucleation time is about 10 hours at 800 °C
- the precipitation of the phase is next to the chromium nitride at the outline of the cells

Sigma-phase can also forms out of delta-ferrite, because in high alloyed Cr-Ni-steels the composition of the delta-ferrite is similar.

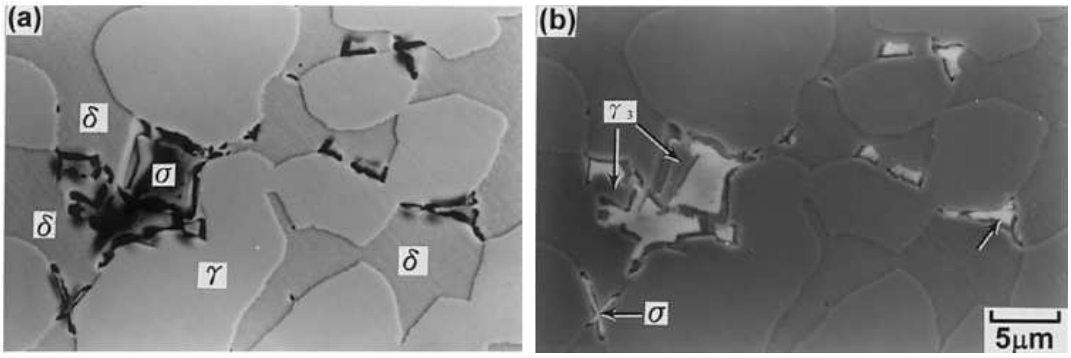

Fig. 1.20 SEM micrographies of the phase a) secondary electrons, b) BS [26]

Other researches show that the formation occurs simply from austenite with the reaction: $\gamma \rightarrow \gamma'' + \sigma$ where y'' is a chromium- and molybdenum-depleted austenite compared to the original austenite. Precipitation occurs predominantly at grain boundaries, especially at triple points. However all the mechanisms were observed and it depends on the thermal condition of ageing and the steel composition that can favourite the different type of precipitation.

So as it was explained previously in the range of formation of σ phase its nucleation is favourite when the precipitation of Chromium nitrides occurs in the HNS steels. In fact in this case the depletion of nitrogen in solid solution contributes to the σ phase stability and to promote its nucleation [35].

The precipitation of the sigma phase does not only cause losses of ductility and toughness of the steel, but also reduces its corrosion resistance by removing chromium and molybdenum from the austenitic matrix [36].

1.4.5.2 The properties and precipitation of the χ phase in HNS steels

The phase was observed in the range temperature: 700-900 °C and the content of this phase is lower than that of sigma phase. In fact the *C* curve is moved related to the sigma one to lower times and temperatures [37].

At long time of treatment the only phase that is observed is the σ phase because the χ phase is a metastable phase and so it is a precursory phase of σ.

Its cubic unit cell with lattice parameter a_χ = 0.892 nm contains 58 atoms, 24 of them

having a 13 coordination number. The χ-phase is found in several binary systems involving transition metals. It frequently occurs in steels, as a ternary compound containing Fe, Cr and Mo, according to the composition $Fe_{36}Cr_{12}Mo_{10}$ [JCPDS-ICDD 31-401].

Some OM and SEM images of χ phase are shown in figures 1.21, 1.22.

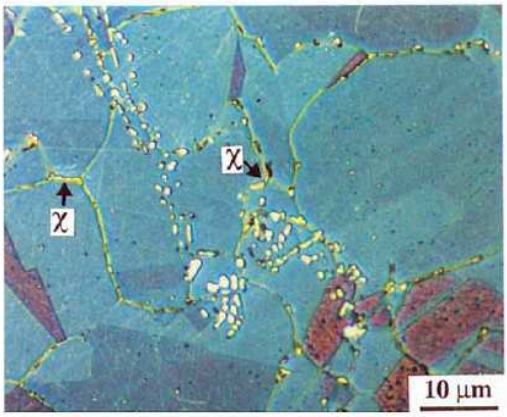

Fig. 1.21 Optical micrography shows the intergranular presence of χ phase [38]

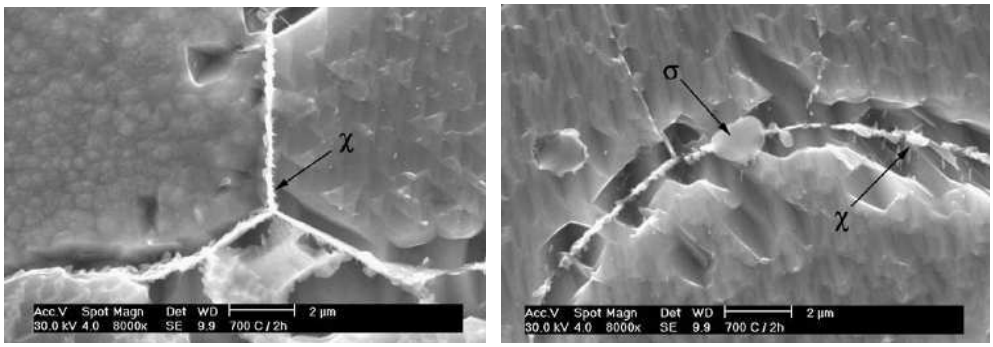

Fig. 1.22 SEM images show the formation on the grain boundary of σ and χ phase [38]

The precipitation of the χ-phase is increased by cold working [40]. The nucleation sites are the grain boundaries, the incoherent twin boundaries and the intragranular dislocations. Occasionally, it also nucleates at coherent twin boundaries. Frequently, the χ-phase grows from $M_{23}C_6$ carbides, which dissolve after ageing at high temperatures. It is well established that the precipitation of the χ-phase leads to a reduction of the creep ductility due to a good resistance to brittle microcrackings. It has also a reverse effect on the toughness and corrosion properties. A substantial depletion of solid

solution strengtheners (like Cr, Mo, C and N) mainly due to a copious precipitation of the χ-phase beyond one hundred hours results in a strong decrease of the yield strength. For the mechanical effect of this phase on the steels with nitrogen as interstitial solute, it was observed for a 316 LN steel [39] that at 1123 K there is a decreasing of the Yeld stress (fig. 1.23) after heat treatments.

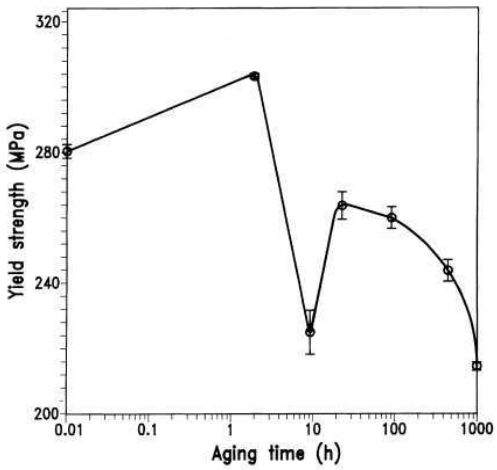

Fig. 1.23 Evolution of YS of the 316LN steel after heat treatment at 1123 K

This behaviour can be associated to the precipitation of Cr_2N and χ phase that was confirmed by XRD measurements of the extracted residue that show also that the content of the χ phase increases with the aging time as observed by Shankar et al. (table 1.6) [39].

Table 1.6. Residue extracted from 316 LN steel after heat treatments at 1123 K

Ratio of XRD peak intensities for two different phases as a function of aging time

Aging time (h)	25	100	500	1000	2000
$Cr_2N/M_{23}C_6$	3.098	2.74	2.0664	1.9388	1.675
Cr_2N/chi	6.73	4.27	2.645	2.11	0.8272

1.4.6 Not complete precipitation in the HNS

The discontinuous precipitation typical of HNS steels has a not-steady state character in contrast to the steady state character of growth features typically observed during cellular precipitation in the binary substitutional systems.

In scientific literature there are experimental results confirming the not-steady conditions of the precipitation in HNS steels. The rate of migration of the cell boundaries was observed decreasing with the treatment time of treatment (fig. 1.24) [35].

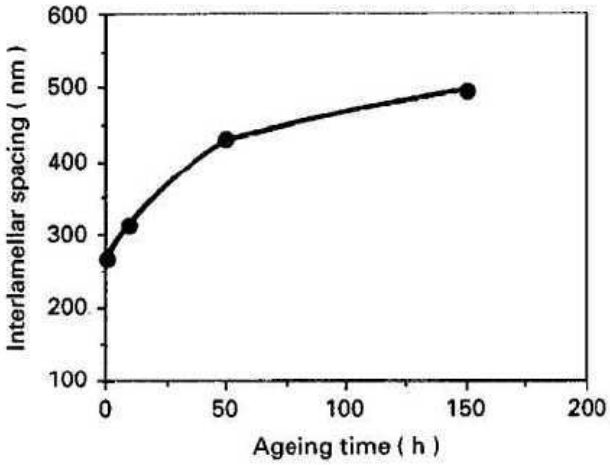

Fig. 1.24 Increasing of interlamellar spacing *S* at 800°C vs. time of treatment for a HNS austenitic steel with N content of 0.9 % [35]

Figure 1.25 also is related to the evolution of precipitation of a HNS steel (0.09% C, 17.54% Cr, 17.81% Mn, 0.37% Ni,0.43% N, 0.022% Al, 0.05% V, and Fe balance) where it can be observed that the volume fraction of the cellular precipitates is not complete also after long times of treatment [41].

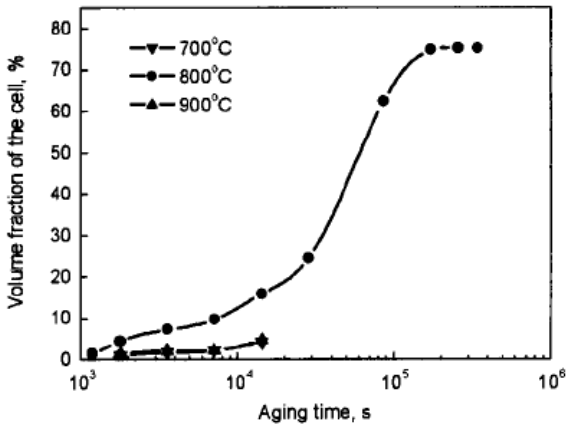

Fig.1.25 Relationship of volume fraction of the cell *vs*. aging time at different aging temperatures [41]

The features of the cellular precipitation for the HNS in particular [17] could so summarized :

- migration rate of the interface between the untrasformed zone – transformed one decreasing with increasing time of treatment
- the volume fraction of precipitate that remains lower than 100 % also after long time of treatment.

Some researchers supposed that the changing in the migration rate of the cell boundary is connected to the nitrogen long range migration, otherwise the stop of the precipitation occurs for the low volume diffusion of the substitutional elements as Chromium [42].

In the present research this phenomenon was studied and the explanation of the incomplete precipitation was given. In particular it was demonstrated that the diffusion of Cr doesn't restrict the precipitation in these steels.

One of the scope of this research is to find the way of diffusion of the solute elements (in particular for N) that characterized the Cr- Mn-N system focusing on the nitrogen and Chromium content in the cell and in the matrix of the steel with the evolution of the precipitation.

1.5 Internal friction in BCC and FCC alloys

1.5.1 Snoek peak in BCC alloys

In the BCC reticule the interstitial atoms are in the octahedral positions (so called for the positions of the atoms that form an octahedral, as shown in fig.1.26).

In an unstressed reticule the positions are equivalent but as it can be observed in fig.1.26 the X interstitial atom is surrounded by four atoms with a different geometrical configuration related to the positions of the four atoms under and up to the interstitial one. This asymmetry is called tetragonal symmetry of the defect. This means that if a stress is applied in a parallel direction to a side of the cell there is a tension in this direction while a compression in the orthogonal one. For this reason the interstitial positions after the stress applied are not the same but there will be easier positions and the atom will occupy those positions.

For cyclic stresses the atom will jump to a position to the other producing a reversible energy dissipation that create a internal friction peak (called **Snoek Peak**).

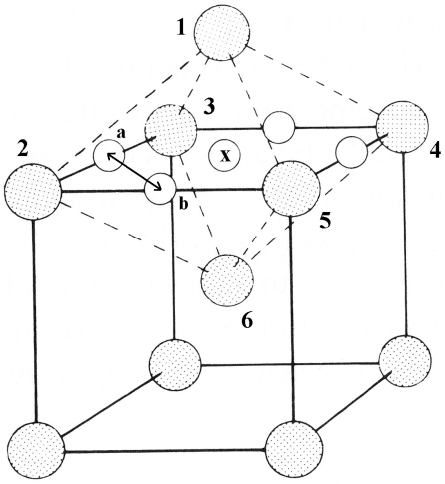

Fig.1.26 Interstitial atoms in octahedral positions of a BCC reticule

For this reason the FI technique can be used to predict the content of a interstitial atoms (C, N, O and H) in the steels with a high precision and no other analysis can able to do. The other tests, in fact, give the total content of an interstitial atoms undistinguishing between the content in solid solution from, that for examples, present in precipitates or in other phases. Knowing which is the energy for the single process connected to an

atom it is possible to calculate the number of atoms that take part in the relaxation process.

1.5.2 Internal fiction in FCC metals and in HNS steels

As well known, the Snoek peak is characteristic for BCC metals. The FCC or EC metals are not characterized by these relaxation phenomena for the symmetry of the interstitial defects. However it must be considered that the alloys haven't the symmetry of the pure metals and so also FCC and EC alloys could present anelastic phenomena.

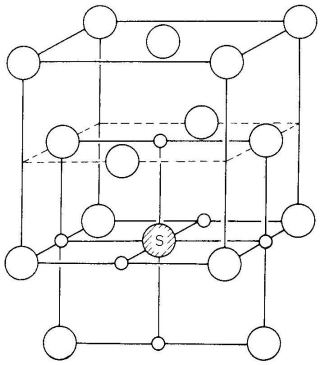

Fig.1.27 Pairs of substitutional – interstitial atom in FCC reticule

So the IF technique could be used also for studying the behaviour of the interstitial atoms in the HNS as it was done in this thesis.

The peaks characteristic for the FCC alloys are called **Snoek-like peaks** and they are caused, for examples, by the riorentation of pairs i-s formed by an interstitial atom and a substitutional one (fig. 1.27). In the BCC lattice this phenomenon is more complex because the Snoek relaxation phenomenon can overput on the Snoek-like process. In addition in a BCC reticule the riorentation of i-s pairs can' t occur only with a "single jump" of the interstitial atom in order to recover the configuration of the pair (fig.1.28) .

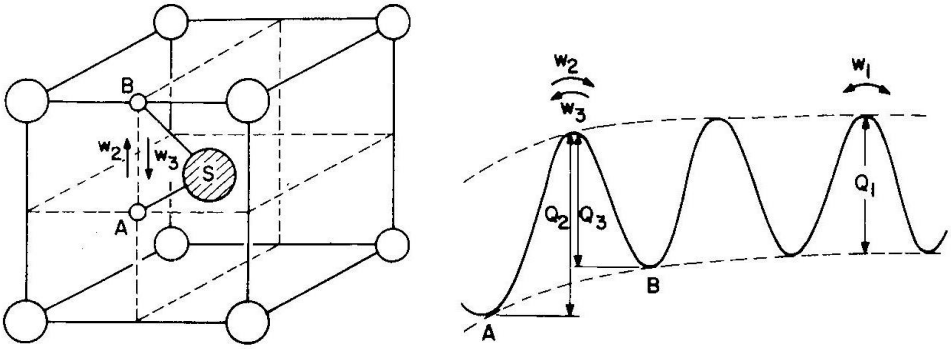

Fig. 1.28 Pairs of substitutional – interstitial atom in BCC reticule

An example of the Snoek-like relaxation process in a FCC reticule is shown in figure 1.29. The steel contains Mn (18.5 %) and different carbon weight percentage 012, 0.37, 0.70, 0.95 e 1.34 %.

It is easy to verify that changing the C content the height of the peak are different. This process can be explained considering the riorentation of the Mn-C pairs: the Mn content is the same in the different measurements while the C concentration changes and this means that the relaxation process is connected to the number of C atoms in solid solution. The interpretation of the phenomenon is also confirmed by another result: the energy activation of the relaxation is exactly the diffusivity of the carbon in Fe γ (1.5 eV).

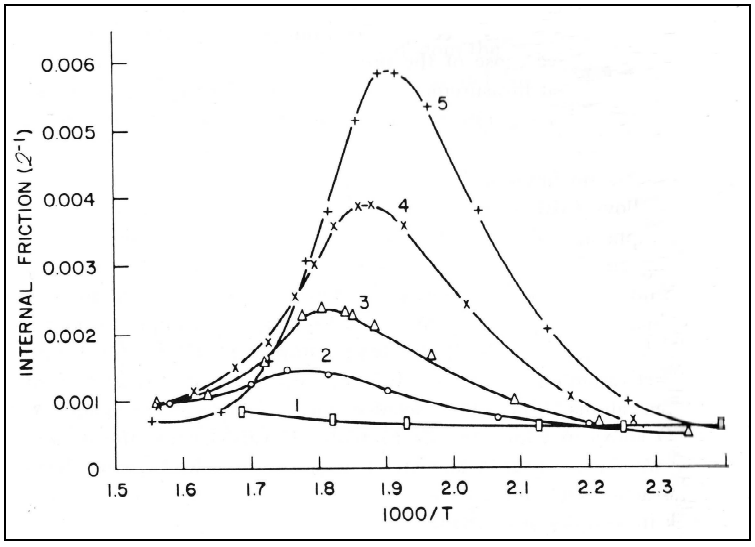

Fig.1.29 Internal fiction peak for a steel with a Mn content of 18.5 % with different concentration of C: 012, 0.37, 0.70, 0.95 and 1.34% respectively [43]

In addition, as shown in figure 1.29, a broadening of the peaks is observed for lower concentrations. In scientific literature not much researches were done on the HNS steels, however the following are the main results obtained.

Banov et al. observed relaxation peaks in steels with high nitrogen content due to the riorentation of the substitutional – interstitial atoms. Banov et al. analysed an austenitic HNS with the composition Fe-Cr (18)-Mn (4)-N (**0.4**) and it was identified a relaxation peak at 625 K and 1 Hz as resonance frequency. For this peak was calculated an activation energy of about 142 KJ/mol (1.47 eV).

Gavriljuk et al. examined a high nitrogen austenitic steel with a different N contents (Cr18Ni16Mn10; 0.07 0.13, 0.21, 0.32, 0.37, 0.44 wt.% of N) obtaining different IF behaviours as observed in figure 1.30 [44].

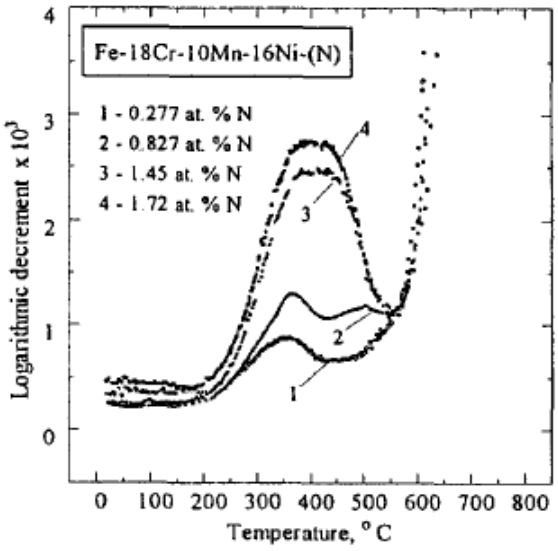

Fig. 1.30 IF data for different HNS steels with four different atomic contents of Nitrogen [44]

It can be observed is that for lower concentrations of nitrogen the peaks split into two peaks for and the correspondent activation energies are 1.1 eV and 1.41 eV as supposed by Banov et al. (fig. 1.32 [44]).

Moreover Banov et al. observed an asymmetry of the peaks with lower interstitial concentration and a high substitutional atoms and they supposed that the typology of the defects in this case can be orthorombic characterizing by two time of relaxations (fig.1.31) while for a higher interstitial contents the defect is tetragonal [44].

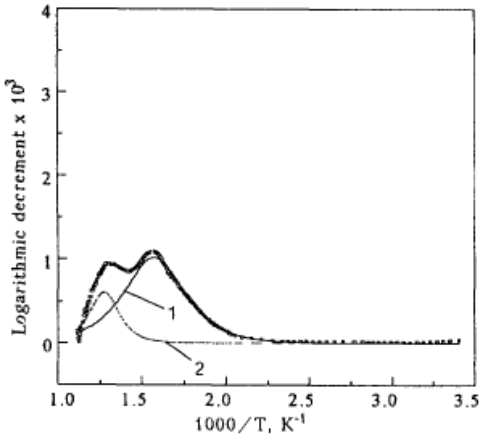

Fig. 1.31 IF data, treated with Arrhenius co-ordinates for a steel (Cr18Ni16Mn10) containing 0.21wt.% of nitrogen [44]

The Snoek like peaks in the FCC steels are mainly connected to the i-s reorientation pairs but there are other hypothesis: i-i or i-vacation riorentations are supposed [44].
The relationship between two interstitial atoms involve that the peak intensity is a quadratic function of the nitrogen concentration but from measurements on these materials it is not observed this behaviour. As shown in figure 1.32 there is a linear behaviour of the Snoek-like intensity vs the nitrogen concentration. A square-like concentration dependence on the relaxation strength is usually observed in carbon austenites, which gives a rise to hypotheses base on the reorientation of i-i pairs [44].

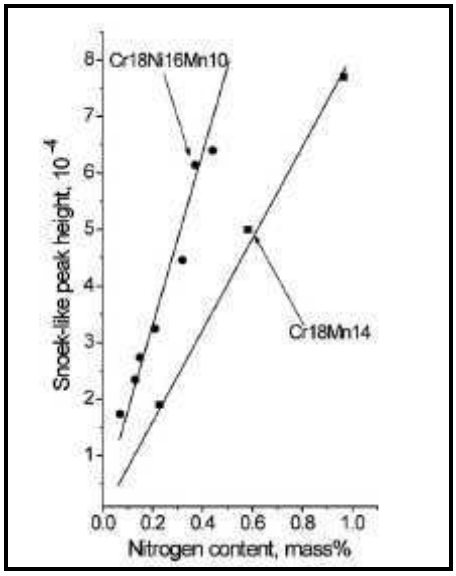

Fig. 1.32 Relationship between the intensity of the Snoek-like peak and the nitrogen concentration in HNS steels [45]

So the best hypothesis for these relaxation phenomena is the i-s pairs riorentation.
The Snoek-like peaks in case of the austenitic steels are called **Finkelshtein- Rosin** peaks and the main properties can be summarized as [46]:

- the activation energy of the relaxation process is near to the diffusivity activation energy of the interstitial atoms
- the peak intensity is proportional to the interstitial atom concentration

In the present thesis the IF measurement on a HNS austenitic steel was carried out.

CHAPTER 2

Experimental Techniques

2.1 SEM, Scanning Electron Microscope

The Scanning Electron Microscope is not based on the light as source of radiations but on the electron beam. The use of the electrons and not photons is connected to the power of resolution. Since the electrons have a lower wavelength related to the photons the power of resolution is higher of some orders of magnitude.

The scheme of a SEM microscope is the following: a W (or La exaboride, more expensive but with a higher energetic efficiency) filament was heated up to 1000 °C and so for a thermionic effect there is a production of electrons. The beam is accelerated through a potential difference of 0.3-30 KV and was deflected in order to generate the scanning and finally deviated on the sample. Typical energies of the SEM are 20-30 KeV.

The least resolution power of a SEM microscope with a W cathode is 5 nm. The sample in order to be analyzed must be conductive (electrostatic charges influence the electron detection). The pressure is low, about 10^{-2} Pa, otherwise there is interaction between the particles produced and the molecules in the camera. The dimension of the beam is about some nm.

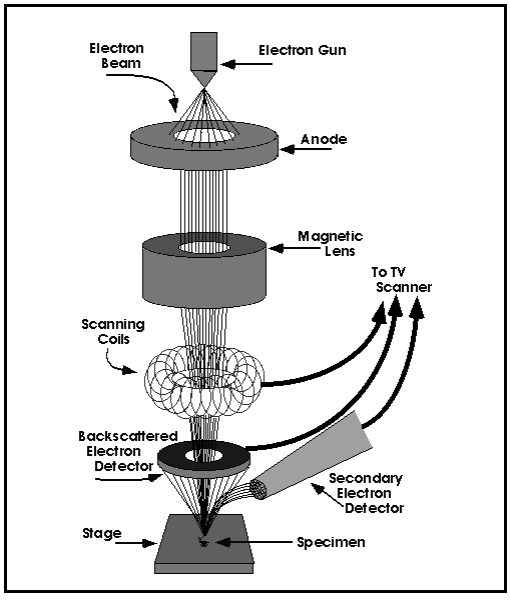

Fig. 2.1 Scheme of a SEM Microscope

The main effects connecting to the interactions between the electrons and the sample are:

- X-ray emissions
- Backscattered electrons
- Secondary electrons
- Auger electrons

Backscattered electrons are produced by the elastic collisions of primary electrons with the sample. For this reason they have a high energy as 20 - 30 KeV.
The event of the elastic collisions (represented by the parameter Q (cm^2), collision section, is proportional to the atomic number (Z). So the elements with high atomic number there is higher possibility to produce elastic collisions and backscattered electrons. These electrons give information about the chemical composition of the sample.
The spatial resolution is higher than the dimension of the beam because the angles of emission from the sample are > 90°. The interaction volume is higher than the same volume of the secondary electrons and is about some hundreds of nm.
The primary electrons diffuse in the sample interacting with the external electrons of the atoms of the sample. Secondary electrons have a low energy and so it is possible that they derive only from the more superficial layers of the sample with a lower interaction volume (0.05 nm) related to the backscattered electrons).
The concentration of these electrons does not depend on the chemical composition but on the morphological structure of the sample. The spatial resolution is better than that for the backscattered electrons and it is very close to the beam dimension [47]. The EDX and WDS spectroscopy are connected to the X-ray production. Both the spectroscopy are based on the X-ray emission produced by a beam of electrons against the sample. When the beam hits the sample electrons from the K and L atomic layers are produced and the system arrive in a not equilibrium condition. So for a relaxation process in which an electron goes from a L orbital in a free orbital K (or from a M orbital to L one) with an emission of energy. This energy can produce two different effects: the emission of a X photon or an ejection of a Auger electron (photoelectric effect). The instrumentation is mainly composed of a detector that can be WDS (Wave Dispersive Spectroscopy) or EDS (Energy Dispersive Spectroscopy) type.

- **WDS detector**: it is based on the selection of the characteristic wavelengths X-ray. It is made of analytical crystal, the sample and detector on the Rowland circle. As it is described by Bragg's law, the reflection occurs only for a single wavelength but it is possible the change moving the detector. The limit of detection is higher than the EDS, it is possible also detecting light elements (Z=4). The limit depends on the electrical current that controls the efficiency of detection.

- **EDS detector**: it is represented by a single-crystal of Si, dopped with Li or high purity Ge crystal, that allows to obtain a better discrimination of the different energies of the X photons. The limit of detection and the resolution is lower than the WDS (it is not possible to detect elements in traces, <1%) but the EDS efficiency is higher than the other X-ray spectroscopy.

2.2 Transmission Electron Microscope

A transmission electron microscope is constituted of: (1) two or three condenser lenses to focus the electron beam on the sample, (2) an objective lens to form the diffraction in the back focal plane and the image of the sample in the image plane, (3) some intermediate lenses to magnify the image or the diffraction pattern on the screen. TEM specimen must be approximately 1000 Å or less in thickness in the area of interest. The power of resolution is higher than SEM, in particular it is about 0.2 nm so five hundreds than the human resolution. The TEM used, in the same way of SEM, a beam of electrons and not of photons.
The samples are put on a plate of Cu or Ni (of about some millimetres) slashed in order to observe the sample without using glass (as in the optical microscope) otherwise the electrons do not go across it. The electrons hit against a flourescent screen projecting on it a real image that is a very high magnification of a portion of the sample.

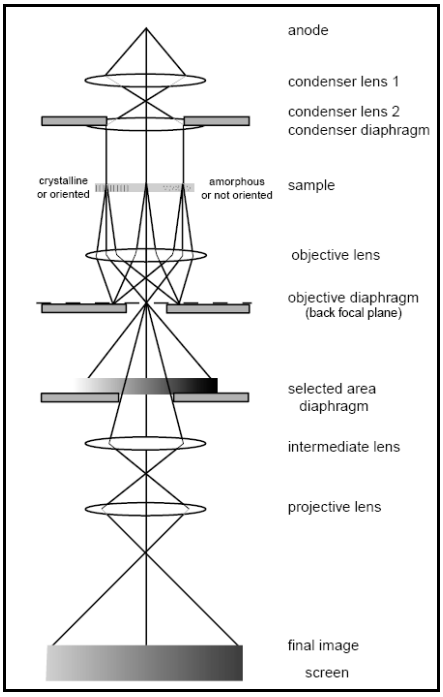

Fig. 2.2 TEM Microscope: Scheme of a transmission electron microscope in image mode. In diffraction mode, an other intermediate lens is inserted to image on the screen the diffraction pattern of the back focal plane.

2.3 Methods of analyzing of non metallic inclusions in the steels

Different methods are applicable to extract particles from a metal, but some of them can not be used for the fine dimensions of the inclusions [48]. These methods are also used in order to study and control steel cleanliness: as known that the type and the dimension of the inclusions in the steels must be strictly controlled (table 2.1, 2.2).

Table 2.1. The effect of some alloy elements in the steels

Element	Form	Mechanical properties affected
S,O	Sulfide and oxide inclusions	• Ductility, Charpy impact value, anisotropy • Formability (elongation, reduction of area and bendability) • Cold forgeability, drawability • Low temperature toughness • Fatigue strength
C,N	Solid solution	• Solid solubility (enhanced), hardenability
	Settled dislocation	• Strain aging (enhanced), ductility and toughness (lowered)
	Pearlite and cementite	• Dispersion (enhanced), ductility and toughness (lowered)
	Carbide and nitride precipitates	• Precipitation, grain refining (enhanced), toughness (enhanced) • Embrittlement by intergranular precipitation
P	Solid solution	• Solid solubility (enhanced), hardenability (enhanced) • Temper brittleness • Separation, secondary work embrittlement

Table 2.2. The dimensional tolerances of some inclusions in the steels

Steel product	Maximum impurity fraction	Maximum inclusion size
IF steel Automotive & deep-drawing Sheet	[C]≤30ppm, [N]≤40ppm, T.O≤40ppm [7], [C]≤10ppm[8], [N]≤50ppm[9] C]≤30ppm, [N]≤30ppm [10]	 100μm [10, 11]
Drawn and Ironed cans	[C]≤30ppm, [N]≤30ppm, T.O≤20ppm [10]	20μm[10]
Alloy steel for Pressure vessels	[P]≤70ppm[12]	
Alloy steel bars	[H]≤2ppm, [N]≤10-20ppm, T.O≤10ppm [13]	
HIC resistant steel (sour gas tubes)	[P]≤50ppm, [S]≤10ppm[12, 14]	
Line pipe	[S]≤30ppm [12], [N]≤35ppm, T.O≤30ppm [13], [N]≤50ppm[9]	100μm[10]
Sheet for continuous annealing	[N]≤20ppm[12]	
Plate for welding	[H]≤1.5ppm[12]	
Bearings	T.O≤10ppm[12, 15]	15μm[13, 15]
Tire cord	[H]≤2ppm, [N]≤40ppm, T.O≤15ppm[13]	10μm[13]
Non-grain-orientated Magnetic Sheet	[N]≤30ppm [9]	
Heavy plate steel	[H]≤2ppm, [N]30-40ppm, T.O≤20ppm[13]	Single inclusion 13μm[10] Cluster 200μm[10]
Wire	[N]≤60ppm, T.O≤30ppm[13]	20μm[13]

The following techniques are used:

- OM (optical microscope) with imaging analyzing

- SEM (scanning microscope) with EDS microanalysis

- Electrolytical or chemical dissolution (it can be carried out through a heated (80-100 °C) acid solution).

- Ultrasounds (inclusions > 20 μm) and **MIDAS** (*Mannesmann Inclusion Detection by Analysis Surfboards)* that underlines the presence of pores

- **EB** (*Electron Beam Melting*): the sample is melted and the inclusions float in surface

- **FTD** (*Fractional Thermal Decomposition*)for the oxided particles: the metal is reduced at high temperature and the oxygen produced give information about the oxides.

- **LIMCA**: Instrument that finds the presence of inclusions basing on the resistance of the liquid

- **LAMMS** (*Laser Microprobe Cleanliness Analizer*): the inner material can be observed through a little probe

- X-ray Photoelectron Spectroscopy **(XPS) : t**his method uses X-rays to map the chemical state of inclusions larger than 10 μm; Auger Electron Spectroscopy **(AES)** – This method use electron beams to map the chemical state of Photo Scattering Method

- Laser-Diffraction Particle Size Analyzer **(LDPSA):** This laser technique can evaluate the size distribution of inclusions that have been extracted from a steel using another method such as slime.

One of easy methods, without necessity of melting material, is the electrolytical dissolution and the XRD measurement on the extracted and this is the method adopted in this thesis.
The steps used for these techniques are the followings:

- polishing of the sample
- dissolution of the metallic matrix with a chemical or electrochemical dissolution
- filtering through polymeric filters of controlled dimension

The electrochemical method is a dissolution of the sample that represents the anode of an electrochemical battery that it is dissolved through an external potential.

2.3.1 Extraction technique employed

In the thesis the extraction of the precipitates is carried out through an electrolysis that is realized with an acid solution (80 % methanol and 20 % hydrochloric acid, fuming at 37 wt.%) and a stainless steel sample as cathode.

After the dissolution, the solution obtained is filtered with a Millipore apparatus that is characterized by a vacuum and filter system (the filters used are pore dimensions of 0.1-0.5 μm).

The figure 2.3 shows the system.

The potential used is **1.5 V** and the range of electrical current measured is **0.1-0.4 A** .

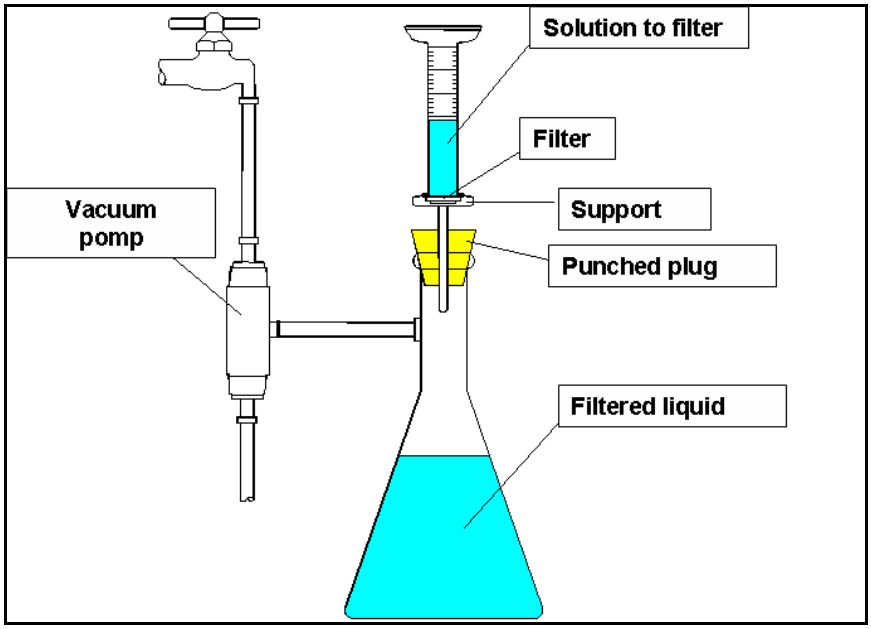

Fig. 2.3 Experimental apparatus for extracting precipitates

After the filtering the dried extracted residue is analyzed through XRD.

2.4 X-ray diffraction

The XRD technique is based on the physical phenomenon of the diffraction: the crystal material has a cell parameter of the same order of magnitude of the wavelength of the X-rays.

It is possible to determinate with this technique different information: the amount, the residual stress and the texture of the crystalline phases.

In agreement with Bragg's law the interference of X-rays is constructive when the phase shift verifies the relation:

$$n\lambda = 2\,d sen\,\Theta \qquad (2.1)$$

where n is an integer, λ is the wavelenght of the X-rays, d is the spacing between the planes in the atomic lattice, and θ is the angle between the incident ray and the scattering planes.

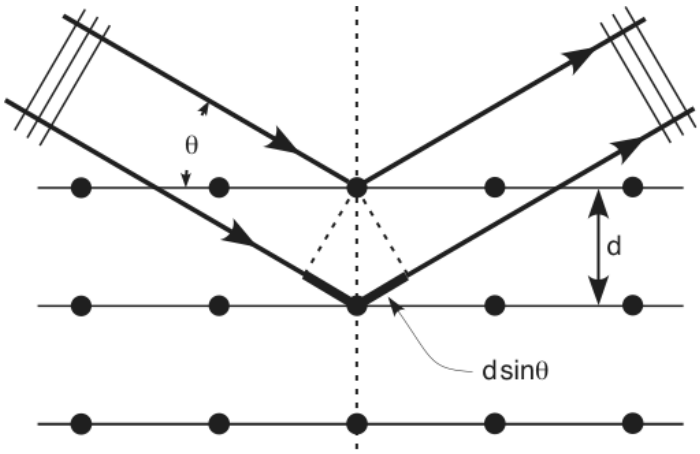

Fig. 2.4 X-ray diffraction for a crystalline phase

The Bragg's law is a necessary but not sufficient condition for the presence of a X-ray reflection. In fact there is also a physical condition that depends on *F* (*Structure Factor)* of the crystalline structure. The table 2.3 shows the conditions of allowed planes for a CCC and CFC lattice.

Table 2.3. Allowed planes for the CCC and CFC lattice

Lattice	**Planes allowed**	**Possible Series**
CCC	**(h+k+l)= evens**	**2,4,6,8,10,12,14,16,..**
CFC	**h,k,l, all odds or evens**	**3,4,8,11,12,16,..**

For a cubic lattice it is possible to connect easily the interplanar distance with the reticular parameter:

$$d_{hkl} = \frac{a}{\sqrt{h^2 + k^2 + l^2}}$$

Using Bragg's law it is obtained :

$$sen^2\Theta = \frac{\lambda^2(h^2 + k^2 + l^2)}{4a^2}$$

In order to obtain a XRD spectrum it is necessary to remove the B*remsstrahlung* contiunuous radiation with proper filter.

2.5 Microhardness

The Vickers microhardness concerns to the measurement of the diagonals of a rhombohedral trace, obtained with a diamond indenter with an angle of 136 °.

It is possible to obtain the HV through the values of the average diagonal, measured on the basis of the relation:

$$HV = \frac{P}{S} = \frac{P0.102}{\frac{d^2/2}{sen(136/2)}} = 0.189\frac{P}{d^2} \qquad (2.2)$$

The load applied is in the range 100 - 500 g and the accuracy is about 1/1000 mm.

2.6 Mechanical Spectrometry

2.6.1 Internal Friction and Dynamic elastic Modulus

The Hooke Law describes the linear behaviour between the stress and the strain so all the energy absorbed is released when the load is stopped (reversible phenomenon).
In the real strain the load is not carried out in an infinite slowly way and so the strain doesn't change together to the stress but with a displacement of a range of time. Since a displacement (δ) occurs between σ and ε for physical reasons there is a dissipation of energy, that in a complete cycle of load and unload is called Internal Energy.

2.6.2 The linear standard solid

If the temporal changing of the stresses and the strains are considered, the Hooke's law is $\sigma(t) = M\epsilon(t)$

where the relationship between the σ and ε is linear.
In the real strain process, instead, it is important the rate of the load application: it is necessary to introduce the first and second derivatives of the σ and ε as the relation (2.3) shows.

$$a_1\sigma + a_2\dot{\sigma} = b_1\epsilon + b_2\dot{\epsilon} \tag{2.3}$$

The solid described by the equation (2.2) is called linear standard solid (S.L.S.).

The relation (2.3) can be also written as the equation (2.3):

$$\sigma + \tau_\epsilon\dot{\sigma} = M_r(\epsilon + \tau_\sigma\dot{\epsilon}) \tag{2.4}$$

where τ_ε is the relaxation time of stress at a constant ε, while τ_σ is the relaxation time of strain at a constant σ, M_r is the elastic modulus relaxed.
If a **constant stress** σ_0 is applied to a S.L.S. at time zero the (2.4) is written:

$$M_r\epsilon + M_r\tau_\sigma\dot{\epsilon} = \sigma_0 \tag{2.5}$$

The solution is the equation:

$$\epsilon(t) = \frac{\sigma_0}{M_r} + (\epsilon_0 - \frac{\sigma_0}{M_r})e^{-t/\tau_\sigma} \qquad (2.6)$$

The figure 2.5 shows the behaviour of $\varepsilon(t)$ vs. time.

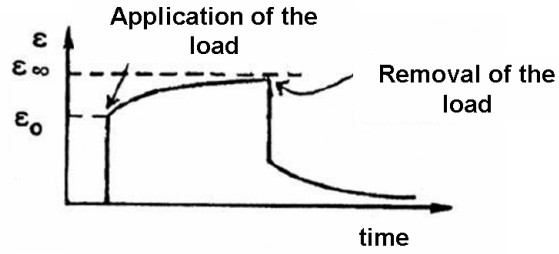

Fig. 2.5 Behaviour of ε (t) vs. time

At the load application ε goes up immediately to the value ε_0 and then increases to the value $e_\infty = \sigma/M_r$ where M_r and M_n are the modulus respectively relaxed and not relaxed. So $M_n = \sigma_0/\varepsilon_0$ describes the relation between the stress and the strain for t=0, while the M_r connects the stress to the strain after the relaxation.

When the load is removed the strain returns to zero with an exponential law.

The relation in the **constant strain** is described by the relation (2.7):

$$\sigma + \tau_\epsilon \dot{\sigma} = M_r \epsilon_0 \qquad (2.7)$$

And the solution is equation (2.8):

$$\sigma(t) = M_r \epsilon 0 + (\sigma_0 - M_r \epsilon 0) e^{-t/\tau_\epsilon} \qquad (2.8)$$

The figure 2.6 represents the behaviour of the stress vs. time and τ_σ and τ_ε represent the rate of the system to the thermodynamic equilibrium with an exponential law.

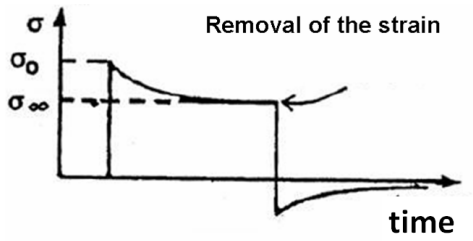

Fig. 2.6 Behaviuor of σ vs. time

In order to obtain the relation between σ and ε before the relaxation the limit of the ratio $\Delta\sigma/\Delta\varepsilon$ is done while the range of the time is going to zero and it is obtained the relations (2.9, 2.10):

$$\tau_\epsilon \Delta\sigma = M_r \tau_\sigma \Delta\epsilon \quad (2.9)$$

and :

$$\Delta\sigma / \Delta\varepsilon = M_r \frac{\tau_\sigma}{\tau_\varepsilon} \quad (2.10)$$

If the M_n (= $\Delta\sigma/\Delta\varepsilon$) is the not relaxed modulus so the (2.10) relation is written:

$$M_n = M_r \frac{\tau_\sigma}{\tau_\varepsilon} \quad (2.11)$$

Since $\tau_\sigma >> \tau_\varepsilon$, therefore the relaxed modulus is always lower than the not relaxed one. Considering $M^2 = M_n M_r$, the defect of the modulus is the ratio: $(M_n - M_r)/\overline{M}$.

2.6.3 Analyzing of the Internal friction for cyclic stresses

When a sample is stressed in the elastic field with a sinusoidal stress, the σ and ε are:

$$\sigma(t) = \sigma_0 e^{\iota\omega t} \quad (2.12)$$

$$\epsilon(t) = \epsilon_0 e^{\iota\omega t} \quad (2.13)$$

Substituting in the relation (2.4) the previous relations, the equation (2.14) is obtained:

$$\sigma_0 = (1 + \iota\omega\tau_\epsilon) = M_r(1 + \iota\omega\tau_\sigma)\epsilon_0 \quad (2.14)$$

So the stress and strain are connected to the complex modulus M_c:

$$M_c = M_r (1+i\omega\tau_\sigma)/(1+i\omega\tau_\varepsilon) \quad (2.15)$$

As the M_c is a complex parameter σ and ε are not in phase and δ is the angle displacement. This parameter has a central importance because it is represents the Internal Energy displaced:

$$\tan\delta = \mathrm{Im}(M_c)/\mathrm{Re}(M_c) \quad (2.16)$$

If it is divided the real and imaginary part of M_c the relation (2.16) can be written as:

$$\tan\delta = \mathrm{Im}(M_c)/\mathrm{Re}(M_c) = \omega(\tau_\sigma - \tau_\varepsilon)/(1 + \omega^2\tau_\sigma\tau_\varepsilon) = \omega\Delta\tau/(1 + \omega^2\tau^{-2}) \quad (2.17)$$

Considering that:
$\Delta\tau = \tau_\sigma - \tau_\varepsilon$ and $\tau_\sigma \tau_\varepsilon = \tau^2$

The relation (2.17) becomes:

$$\tan\delta = (\omega\bar{\tau}/(1+\omega^2\bar{\tau}^{-2}))(M_n - M_r)/\overline{M} \qquad (2.18)$$

if it is considered that $\Delta\tau = (M_n - M_r)\bar{\tau}/\overline{M}$.

The first factor represents the relationship of the Internal Friction and the frequency. So the highest value of this factor is ½ when $\omega\tau = 1$.
The second factor is the measurement of the relative changing of the strain and the stress during the relaxation. The figure 2.7 shows this condition.

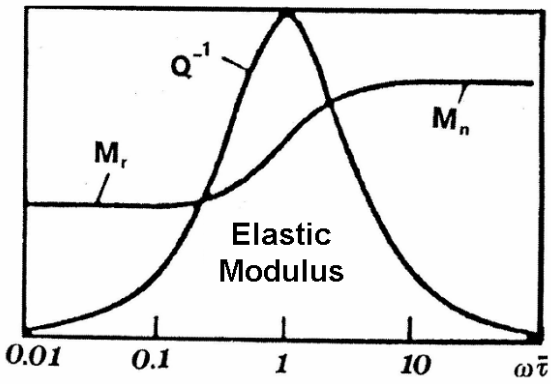

Fig. 2.7 The behaviour of the M_ω and tan δ vs. the frequency.

The modulus dynamic (M_ω) is the real part of the M_c and so the component of the complex modulus of the strain in phase displacement with stress:

$$M_\omega = M_r(1+\omega^2\bar{\tau}^{-2}) \qquad (2.19)$$

As $M_n = Mr\ \tau_\sigma/\tau_\varepsilon$ the relation (2.19) can be written:

$$M_\omega = M_n - (M_n - M_r)/(1+\omega^2\bar{\tau}^2) \qquad (2.10)$$

So it is obtained that M_ω:

- is M_r when $\omega\tau << 1$
- is M_n when $\omega\tau >> 1$

The conclusions are the followings:

- at the low frequency the dissipation of Internal Energy is not observed and the modulus is M_r: the strain has time to follow the stress

- at high frequency the dissipation of Internal Energy is zero for the high rate of the application of the stress so the modulus is M_n
- at the intermediate frequency, when $\omega \tau = 1$, so the amplitude of the internal friction is the highest and the modulus has a value contained in the range between M_r and M_n.

2.6.4 Measurement of dissipation Internal Energy (Q^{-1})

There are different methods for measuring the Q^{-1}, one of the most consistent is the method of Frequency Modulation. This technique is based on the electrical conversion of a mechanical vibration: the sample is excited assuming a mechanical vibration through an electrode, so the changing in the capacity electrode-sample (as a capacitor) modulates an oscillator. The change of the capacity then modulates an electrical signal in frequency.

The change in pulsation of the carrier is agreement with the equation (2.21) :

$$\Delta\omega = -\frac{1}{2}\omega_h \frac{\Delta C}{C} \qquad (2.21)$$

Where the ω_h is the pulsation of the carrier and the amplitude of the modulation is proportional to the factor $\Delta C/C$.

When the excitation on the sample is deleted, the mechanical vibrations decrease and the electrical signal in exit has the behaviour of a sinusoidal drop shot. The equation (2.22) expresses the relation between the Energy and the logarithmic decreasing of signal in the half-cycle:

$$Q^{-1} = \frac{d}{\pi} \qquad (2.22)$$

Where $d = \frac{1}{n}\frac{V_o}{V_n}$ is the logarithmic decrement and V_0, V_n are the amplitudes.

Another important definition is the relation (2.23):

$$Q^{-1} = tan\delta = \frac{d}{\pi} = \frac{1}{2\pi}\frac{\Delta E}{E} = \frac{\omega_2 - \omega_1}{\omega_0} \qquad (2.23)$$

where the Q^{-1} is connected to the pulsations: ω is the Resonance frequency, ω_1 and ω_2 are the pulsations related to the highest amplitudes/ $\sqrt{2}$.
The figure 2.8 summarized all the relations written.

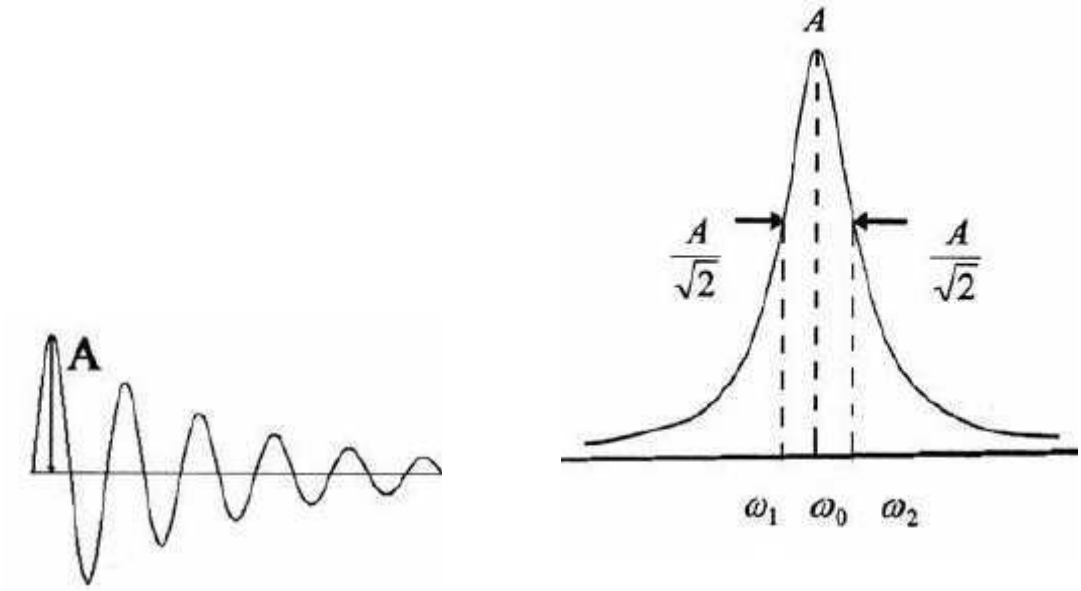

Fig.2.8 Q^{-1} measurements through the pulsations or calculated through the logarithmic decrement.

In the experimental way if the Q^{-1} is higher than 10^{-2} the measurement is carried out through the pulsations, otherwise it is calculated through the logarithmic decrement.

Since at $\omega\tau = 1$ there is a maximum of dissipation of internal energy, it is possible to connect the Resonance frequency (at a specific temperature) to the Activation Energy of the phenomenon that causes the relaxation process:

$$\omega\tau = \omega\tau_0 e^{\frac{H}{RT}} = 1 \qquad (2.24)$$

where:

- H and τ_0 are respectively the Activation Energy and the relaxation time of the physical phenomenon connected to the relaxation
- R constant of perfect gas
- T the temperature (K)

Through the Arrhenius plot, $ln\ \omega\tau$ vs. $1/T_P$ it is in this way possible to calculate the activation energy of the phenomenon.

2.6.5 Elastic Modulus measurement

The existing methods to measure E (in agreement with the Hook's law, $\sigma=E\varepsilon$ where E is a constant) are different:

- Tensile stress test
- Ultrasound (it is a dynamic technique through the measurement of the sound velocity that is function of density and elastic modulus)
- The frequency of a sample with a known geometry.

For the last method in the case of a cantilever the system in figure 2.9 is considered.

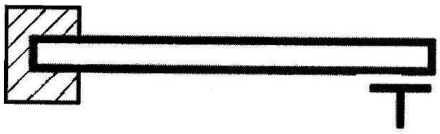

Fig. 2.9 A cantilever

The boundary values allow to obtain the equation:

$$\cos(H_i L)\cosh(H_i L) = -1$$

and the first solutions are

$$H_1 L = 1.875 \text{ e } H_2 L = 4.694$$

If the value $H_iL=m$, it is possible to write the formula where the Resonance frequency is connect to the modulus (2.25)

$$f = \frac{m^2 h}{2\pi\sqrt{12}L^2}\sqrt{\frac{E}{\rho}} \qquad (2.25)$$

- ρ is density
- h is the thickness
- L is the free length

So the relation of the Modulus expression is obtained:

$$E = \rho(\frac{f2\pi\sqrt{12}L^2}{m^2h})^2$$

2.6.6 Internal Friction instrumentation

The IF experimental apparatus is the VRA 1604 Vibrating Reed Analyzer: it is made of a central unity and of some external components that are connected to the central part as shown in figure 2.10.

The external parts are:

- rotary pomp
- aspiration pomp for the liquid nitrogen;
- heat system with a DC alimentation
- a PC for the control and acquisition of the data

The external component without alimentation are:

- cylinder at compress air for opening camera
- water alimentation and water discharging
- hydrogen liquid as cooling system.

a) ***b)***

Fig.2.10 Experimental apparatus VRA 1604 (a) and control panel of VRA 1604 (b)

All the external components are connected to the main unity with a panel, as shown in figure 2.10, through it they are controlled and they are fed.
In order to start a test with the VRA system the following steps are necessary:

- set of the started positions and collocation of the sample
- making empty
- choosing the using measurement system
- set the geometry and physical proprieties (density,..) of the sample
- set the distance between the sample and the electrode
- set the voltage range of the signal and controlling the stability of the sample excited.

After the starting steps, it is possible to monitor the behaviour of the test trough a PC and controlling the fixed parameters, if the test are not satisfactory it is possible to stop testing and modify the parameters.
The reception of the signal depends on the principle of the transmission of the radio waves.
The capacity of the system sample- electrode is modulated in frequency by the oscillation of the sample. This signal modulated in amplitude is expressed as:

$$A(t) = A_0 \cos\omega_s t \qquad (2.26)$$

Where ω_s is the pulse of the vibration of the sample through a receiving circuit tuning with the oscillator. In the starting phase it is important to make the tuning in order to acquire the results in a correct way.

2.7 Micro-chemical spectroscopic techniques

The spectroscopic techniques utilize the electron emission processes caused by an electrons source (AES and SEM) or by a photons source (XPS) with an appropriate energy. The differences between these spectroscopic techniques is in different processes of quantum nature that involve the system studied [49]. These techniques carry out investigations on different portions of the specific studied surface (Fig.2.11).

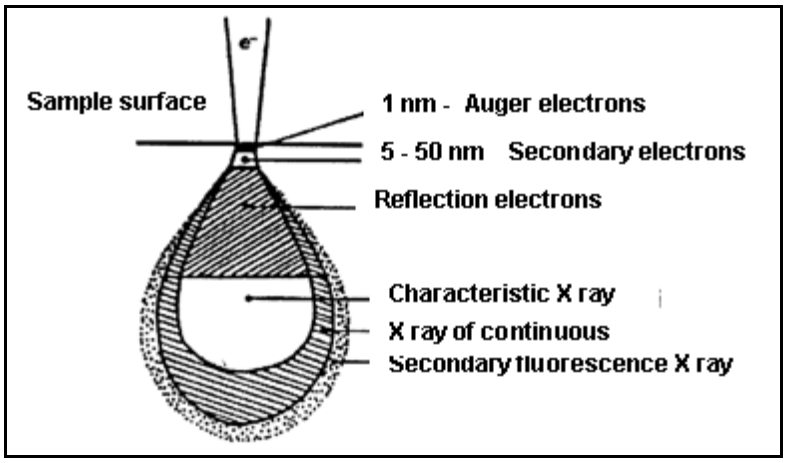

Fig.2.11 Pattern of particles involved in emission in the sample volume

2.7.1 X-ray Photoelectron Spectroscopy (XPS)

The XPS spectroscopy uses the photoelectric effect to obtain informations. As known the photoelectric effect arises by the interaction between radiation-material. The photoemission is based on the following process: a photon is absorbed by the atom A, which in turn discharges an electron in a vacuum. By an appropriate collection and dispersal system the kinetic energy of electronics photoemission is measured. The process, therefore, can be shown as:

$$A + h\nu \rightarrow A^{+} + e^{-} \qquad (2.27)$$

The conservation law of total energy requires that:

$$E(A) + h\nu = E(A^{+}) + E_k(e^{-}) \qquad (2.28)$$

By arrangement:

$$E_k(e^{-}) = h\nu + [E(A^{+}) - E(A)] \qquad (2.29)$$

The difference in energy between the final ionized state and that initial neutral is called Binding Energy (BE) of electronics photoemission. The equation (2.29) is not complete because the factor ϕ is introduced (work function) that considers the necessary work to bring the electron in a vacuum.

$$E_k = h\nu - E_b - \phi \qquad (2.30)$$

E_k is the is the photoemission kinetic energy, $h\nu$ exciting radiation and E_b is the electron binding energy in the solid.

The equation (2.30) is valid in the photoemission process of elastic type. The binding energy depends on the ion chemical nature, on the type of atomic orbital in that the gap has created. If comparing the experimental values of electronic BE levels of an atom with the orbital energy theory, it should be noted that the first refer to the Fermi level of the solid and the second to the vacuum level.

The photoemission process is anelastic if the photo-electron have a change of its energy (usually a loss) between the photoemission and collecting in the spectrometer. The loss of energy can occur through a series of mechanisms that will be discussed later. The effect of radiation photoemission due to the Bremsstrahlung radiation is dominant at low BE, while the effect related to the secondary electrons, resulting by anelastic photoemission, is dominant in low kinetic energy. The spectroscopic range of each element is characterized by the presence of a number of photoemission peaks, in relation to the number of core present electrons (inner electrons). H and He does not possess Core electrons, can not be identified by XPS spectroscopy.

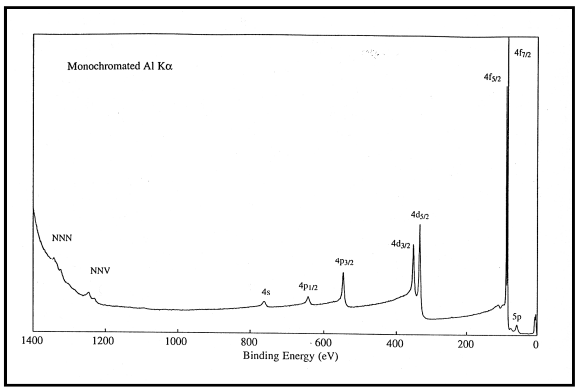

Fig2.12 Full scan spectrum of Au excited with a source of Al Kα

In figure 2.12 is given the full Au spectrum. That spectrum is characterized by a background in which there are peaks, each of which is identified by the specific atomic orbital in according to the bonding energy. In addition to the peaks due to the photoemission process, there are also spikes caused by the process called Auger (NNV, NNN in Fig.2.12), which mechanism will be discussed in the next paragraph.

2.7.1.1 Qualitative analysis

Carrying a spectrum in a large BE range, it can be identified all the components of the investigated surface. In most cases, the peaks are well resolved and a certain

identification allowed, if the element is present in concentrations greater than 0.1 % atomic.

Photoemission spectroscopy offers the possibility to obtain informations on the status of a chemical element through the binding energy changing, better known as “chemical shift”.

About that the theoretic concepts is not easy to describe, but fortunately the determination of the chemical shift is much easier. This deals to determine the BE value of a signal of an element and to compare it with the BE value of the same elements in a different context. But comparing BE is not as immediate as it seems. The photoemission physical process, as already mentioned, is a ionization process. The extract electron generates in the initial neutral system a positive charge, with the consequent loading of the sample. Of course, wanting to measure BE system neutral, loading must be limited and, if possible, avoided. For this reason, during data acquisition, on the sample a electron flow must be guaranteed that neutralizes the charge. However the definition of zero in the scale of binding energies, is univocal only for conductive samples, as their electrical coupling allows to determine as the zero value for that is experimentally obtained the “Fermi edge”, i.e. the Fermi level position, by a carefully cleaned in place by a metal such as Ag.

The obstacle of a not-conductive material can be overcome through using a reference signal to a fixed location and well known. Normally it takes as a reference the signal of C 1s rising by the carbon contamination (285.0 eV). In some cases, a flow of low-energy electrons is used to neutralize the charge that forms during the photoemission.

The presence of signals arising from the processes of secondary nature makes the spectrum acquisition by XPS more complex, also if the presence of secondary structures has the advantage of obtaining additional informations on the nature of the sample investigated.

2.7.1.2 Quantitative analysis

The quantitative determination of the various chemical species, expressed as percentages of nuclear and/or atomic relations, is connects to the relationship between the main areas of the reviewed peaks. This intensity ratio must be correct for the impact section of photoemission, characteristic for all levels of the individual elements.

The methods used for quantitative analysis are two:

- Method of the sensitivity factors

- Method of fundamental principles.

The first method is still widely used. It consists to compare the relative intensity of the elements under consideration with those of the peak F1s and C1s (taken as unit), measured directly or indirectly in known stoichiometry compounds. Through these values the measured intensity are correct for the compound under consideration.

The second method allows to get plenty of different atomic species by inductive way. It must take into account several factors: the average free electron path, all compensation due to the trajectories of elastic diffusion, instrumental factors, etc.. The general formula describing the relationship between the current of photoelectrons from a level of an element and the presence of this element in the sample is analyzed as follows:

$$I(E_k, X) = \sigma_i(h\nu, \gamma, X) S(E_k, E_a) \varphi(h\nu) \int_{x=-x_f}^{x_f} \int_{y=-y_f}^{y} \int_{z=0}^{\infty} N_i(x, y, z) \exp\left[-\frac{z}{\lambda(E_k) \cos\theta} \right] dx dy dz \qquad (2.31)$$

where:

- $I(E_k,X)$ is the peak intensity on the level of the considered orbital X:
- E_k is the kinetic energy of photoelectrons;
- φ is the flow of ionizing photons;
- σ_i the differential photo-ionization cross section;
- λ is the anelastic average free path of photoelectrons;
- S is the instrumental factor, takes into account both the geometry and the acquisition mode. In this variable is included transmission analyzer and its resolving power, and its sampled area. This feature is specific to each instrument and operating conditions, and it must be determined experimentally;
- N_i is the distribution of the element i into the sample.

Only about λ (free medium path) it is possible to say that the value depends mainly by electron kinetic energy and marginally by the chemical and structural nature of the material.

The trend of λ reported as function of photo-electron kinetic energy provides a “universal”

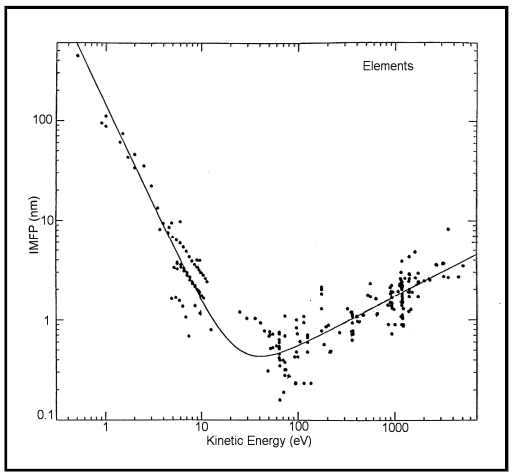

Fig.2.13 IMFP trend vs. KE

curve (Fig.2.13). If the probability function of electron escape is integrated from zero to 3λ, it be got that 95% of the signal comes from this depth. The difference between the two methods is that there may be factors of sensitivity for each geometry, operating conditions and instrument class, which is not possible for the first method that is for one specific situation. Over the estimation of these parameters is more accurate and the result is reliable.

2.7.1.3 Depth profile

As discussed above, the photoemission spectroscopy XPS obtains information about the chemical and physical nature of the first 1-10 nm of the sample surface. The experimentation may be extended to greater depths by different experimental approaches:

Non destructive process:

A) Fig.2.13 shows the correlation between the photo-electron kinetic energy and the depth that comes out. It is possible to study the photoelectrons with a greater kinetic energy;

B) If the report to the intensity is expressed as:

$$I_d = I_\infty [1 - exp (- d/\lambda sen\theta)] \qquad (2.32)$$

Where I_d and I_∞ is the intensity of the peak for the thickness d and for infinite. Changing the angle of photoelectron collection, it is obtained different depths of the samples.

Destructive process:

C) the sample is bombarded by ions of noble gases (with an less energy than 10 keV) which erodes the material, giving the opportunity to study the structure below. Alternating cycles of ion sputtering (this is called the ionic erosion process) by XPS scansion, it is possible to build the depth profile. This procedure involves a careful analysis of the effects that may affect the investigation:

1) preferential sputtering: atoms can be removed with a different rate of erosion, the procedure would produce a variation of artificial stoichiometry of the sample;
2) reduction in the oxidation number of an induced on bombardment, for example $Cu^{2+} \rightarrow Cu^{+}$ or $Sn^{4+} \rightarrow Sn^{0}$;
3) not uniform erosion due to the shade effects for the sample roughness or the presence of surface contamination; uneven distribution of ion beam; bad geometry between the ion beam and the X-ray beam.

By ionic sputtering gives a concentration profile versus erosion time of the sample.

2.7.2 Auger Electron Spectroscopy (AES)

Auger spectroscopy is a two-stage process. The first involves the formation of an electronically excited ion, $A^{+*,}$ following the exposure of the sample to a X-rays or electron beam. With an electron beam the excitation reaction can be written as:

$$A + e^{-} \rightarrow A^{+*} + e^{-} + e^{-}_{A} \qquad (2.33)$$

where e^{-} is the incident electron from the source, and e^{-}_{A} is an electron that has been issued by an internal orbital of *A.* An atom with an internal electronic gap is unstable, then the process to eliminate this gap begins: an electron from a higher level to the lower level will fall filling the gap, but still leaving the system with a vacancy.

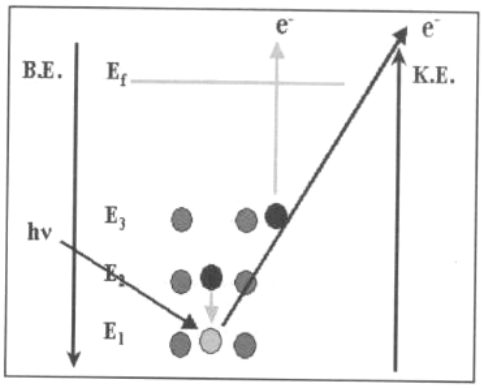

Fig.2.14 Auger effect

The relaxation process can take place by two mechanisms in competition with each other:

A) the ion loses another electron from a higher level:

$$A^{+*} \rightarrow A^{2+} + e^{-`}_{A} \qquad (2.34)$$

The $e^{-`}_{A}$ is connected to the kinetic energy of Auger electron. In the relation (2.35), all the atomic levels involved in the process are shown: the level K, which was issued the first electron, the level L_1, from which comes the electron to fill the gap created and the level $L_{2,3}$ of the second electron ejected:

$$E_{KL1L2,3} = E_K - E_{L1} - E^{*}_{L2,3} \qquad (2.35)$$

$E_{*L2,3}$ is the binding energy level of $L_{2,3}$ in the presence of a potential hole in the internal level L_1.

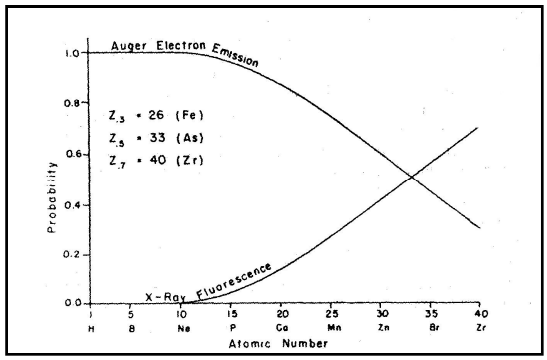

Fig.2.15 Probability of relaxation through the release of an Auger electron or through the emission of a photon of X-ray energy feature

B) the fluorescence X: the photon emission whose energy is equal to E_K - E_{L1}.

The occurrence probability of one or other process is described by Fig.2.15 Auger spectroscopy is characterized by its high sensitivity for light atoms ($3 < z < 15$), the explanation is connected to the etching of the *core* electrons that is simpler for the light elements while the fluorescence effect is easier for the heavy ones. Important characteristics of this analysis are: its minimal matrix effects and a high spatial resolution (0.2 μm) which allows to perform detailed examinations of solid surfaces.

Aim of the Research

The role of N in the austenitic steels is increasing the γ stability (substituting Ni) and rising the corrosion and mechanical properties through solid solution strengthening.

For broadening the fields of application of these steels however it is necessary knowing the material behaviour in all environment conditions.

The property deterioration in the aging temperature range (550 to 920°C) is a serious problem that limits the use of HNS steels for high temperature applications.

In particular the thermal instability could produce mechanical changes not suitable to application at high temperature.

This thesis has the purpose to investigate the evolution of a HNS austenitic steel as prepared and after heat treatments (at 800°C and 850 °C) in order to establish the limits of the microstructural stability.

The samples as prepared and after the heat treatments were analyzed through optical microscopy (OM), scanning electron microscopy (SEM), transmission electron microscopy (TEM), energy dispersion spectroscopy (EDS) and Auger electron spectroscopy (AES).

To investigate better the phenomenon of the nitride precipitation IF measurements and XPS spatially resolved analysis were carried out.

CHAPTER 3

Experimental Results

3.1 Microstructural characterization of the HNS austenitic steel

The examined material is a high-nitrogen austenitic stainless steel produced by Pressurized Electroslag Remelting (PESR) at Centro Sviluppo Materiali (CSM). Its chemical composition in wt.% is: 20 Cr, 2.5 Mo, 17 Mn, 0.2 C, 0.8 N, balance Fe.

The microstructural changes of the material were examined at two different temperatures: 800 and 850 °C in successive steps up to 23 hours.

These temperatures were chosen in order to know which is the temperature of the highest kinetic of precipitation of Cr_2N.

3.1.1 The as-prepared material

The as prepared material, before the heat treatments, was characterized by different experimental techniques. After mechanical polishing, the material has been etched in a water solution of 10% HCl, $K_2S_2O_5$ (10 g/l) and NH_4HF_2 (24 g/l) (fig. 3.1 b), and through an electrolytical etching (3.1 a) [50-51]. The examination was carried out by optical microscopy (OM), scanning electron microscopy (SEM), transmission electron microscopy (TEM), energy dispersion spectroscopy (EDS) and Auger electron spectroscopy (AES).

The average grain size is about 50 μm and some twins are observed (fig. 3.1).

a) ***b)***

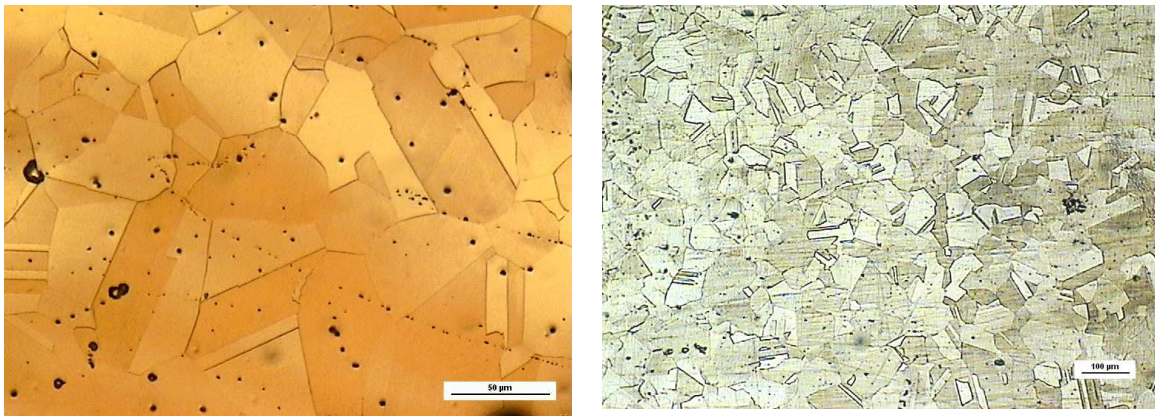

Fig. 3.1 As prepared material a) electrochemical etching, b) chemical etching

The as-prepared material is not properly solubilized for the presence of precipitates with a homogeneous distribution in the inner and at the grain boundaries.

The particles were identified (through TEM diffraction and EDX analysis) as precipitates of AlN (aluminium nitrides), probably connected to the addition of aluminates in the remelting process of the steel. The dimensions of the particles can reach the length of several microns.

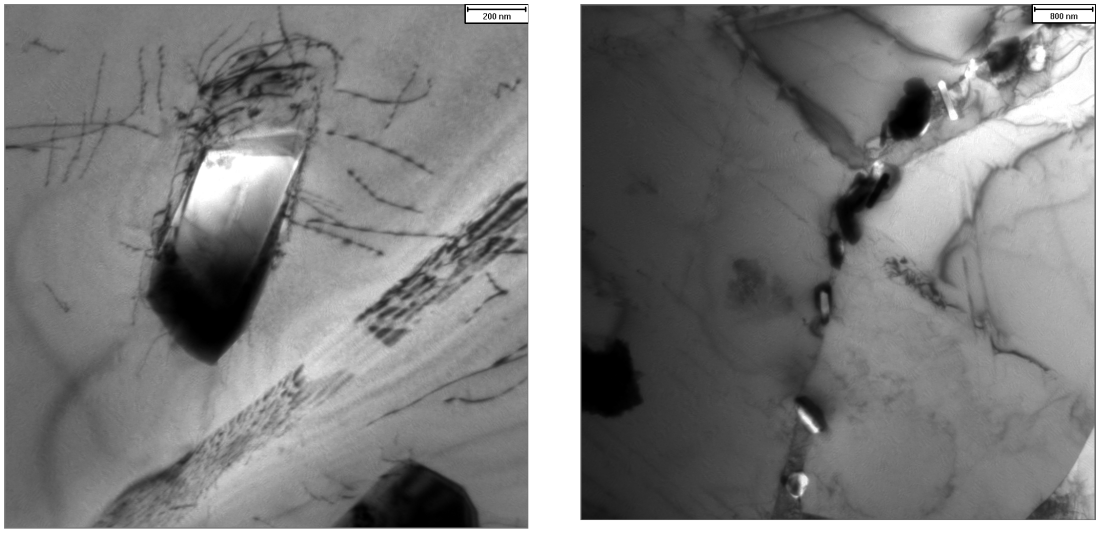

a) ***b)***

Fig, 3.2 AlN precipitates at the grain boundary

TEM micrographies (3.2 a, b) show a typical dislocation structure near to some precipitates found in the as prepared material: the dislocations can go over the AlN precipitates only with the Orowan mechanism (Fig. 3.3).

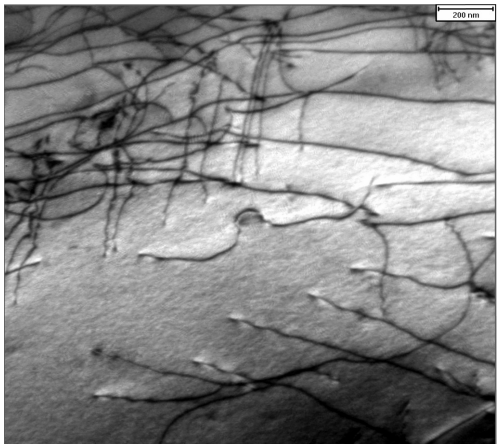

Fig. 3.3 Dislocations around AlN particles

In order to control the degree of solubilization of the as-prepared steel, the material was dissolved by an electrochemical method: solution (80% methylic alcohol - 20% HCl), stainless steel cathode and potential of 1.5 V. Filters with pores of 0.1 μm have been employed for the extraction of the particles from the liquid. The XRD results of the extracted residue have confirmed the absence of Chromium nitrides in the as-prepared material but verifying the presence of AlN.

3.1.2 Treated material

The steel was investigated after successive steps of heat treatment at two different temperatures (800 and 850 °C) for increasing time.

After each step of heating the material has been examined by X-ray diffraction (XRD), optical microscopy (OM), transmission electron microscopy (TEM), Auger electron spectroscopy (AES), microhardness tests and electrolytical extraction.

3.1.2.1 MO, SEM, TEM

Cellular precipitation (fig.3.4) occurs in heat treated samples: carbo-nitrides (for simplifying indicated as Cr_2N) and a secondary austenitic phase γ with a lower nitrogen content than the γ_S one. The transformation:

$$\gamma_S \rightarrow \gamma + Cr_2N \qquad (3.1)$$

is the typical discontinuous precipitation of the Cr-Mn-N system in the temperature range of 700-900 °C [30].

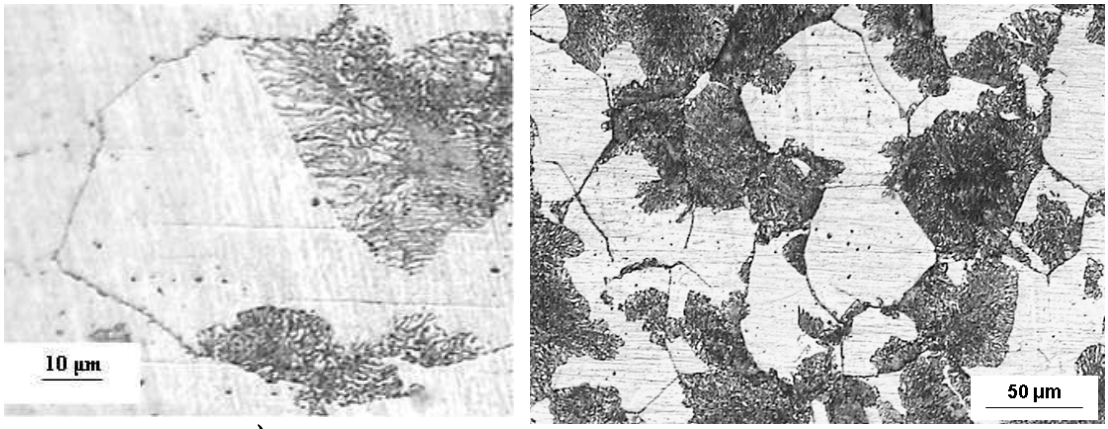

a) ***b)***

Fig. 3.4 Cellular precipitation after heat treatments

In the optical micrographies as shown (figure 3.5, a, b) the cellular precipitation can be observed. It is clear that the precipitation starts at the grain boundary and goes on to the inner of the grain (3.5, a). In the figures 3.5 a, b SEM – SE (*secondary*) electrons image and SEM–BS (*backscattered*) one are shown.

Even after long time treatments (23 hours at 850°C) the size of the Cr_2N is about few microns (fig. 3.5 c, d) even if in the optical micrographies (3.4 a, b) the precipitate length seems higher because it is no possible to distinguish one precipitate to the each other. The figure 3.5 d shows carbo-nitrides with a lengthened shapes and a parallel orientation to each others.

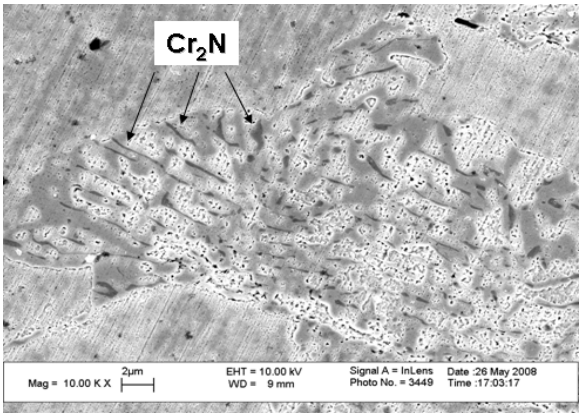

a)

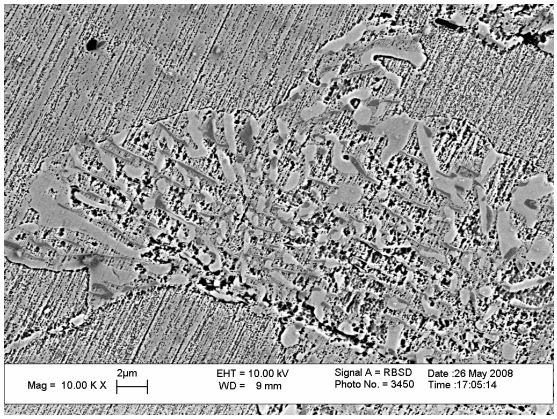

b)

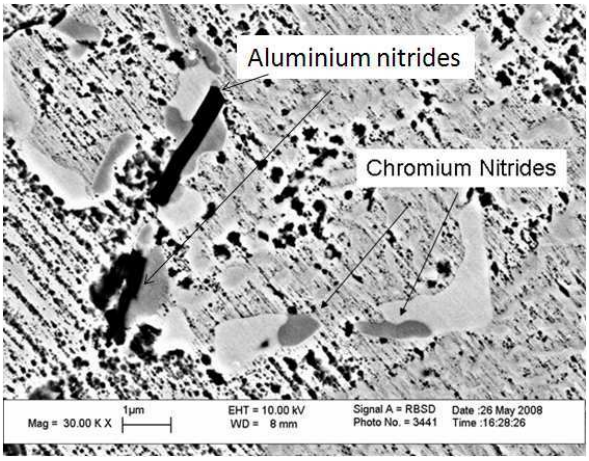

c)

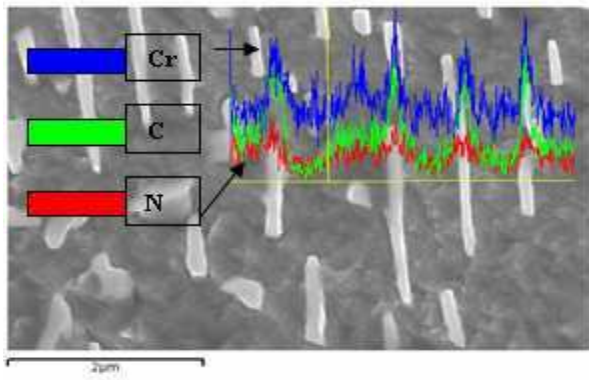

d)

Fig. 3.5 Cellular precipitation after the heat treatments : a) 23 hours at 800°C (SEM secondary electrons), b)SEM–BS (*backscattered*) c) Chromium nitrides (the smallest) and AlN (the darkest) in a sample treated 23 hours at 800°C (SEM-backscattered), d) EDS microanalytical profiles of sample treated 5 h a 850°C (SEM)

The black particles of figure 3.5, c) are not Cr_2N but aluminium nitrides with higher dimension than the carbon- nitrides.

EDS microanalytical profiles (fig. 3.5, d) confirm the enrichment of N and Cr in the lamallae while a decreasing of these elements in the next zones.

The figures 3.5, a, b shows that there is a preferential etching the grain boundaries and the decreasing of the Cr content in the interface between transformed and not transformed zones after precipitation can be the reason of this phenomenon.

Through TEM micrographies it was possible to analyze the lamellar structure of the transformed zone related to the temperature.

The interlamellar spacing depends, in fact, on the treatment temperature: the distances are smaller for lower temperatures: ~190 nm at 800 °C and ~260 nm at 850 °C (figs. 3.6 a-b).

The lamellar growth generally takes place in the advancing interface between the transformed and the untransformed zone.

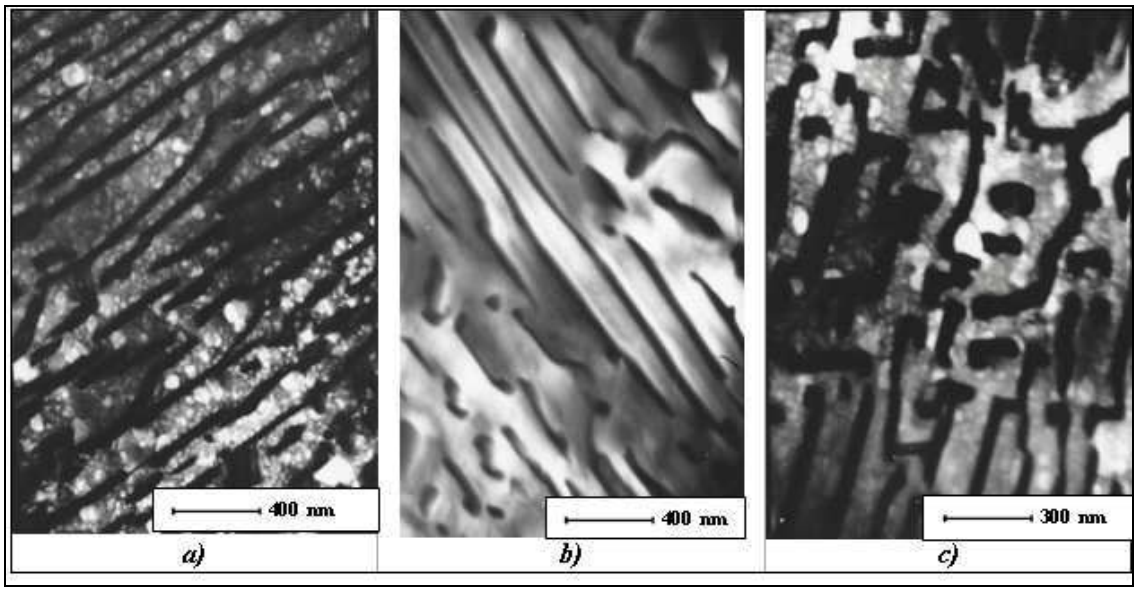

Fig. 3.6 TEM micrographies of samples treated 23 hours at 800 and 850 °C.

However, when a large part of the material is involved in the cellular precipitation, the mobile interface stops and the growth goes on in the direction orthogonal to the initial one (fig. 3.6 c). This feature has been also observed by other investigators [30].

3.1.2.2 Electrolytical extraction of precipitates of the treated material

The treated steel was dissolved by the electrochemical method. To identify the precipitates, they were extracted from the treated matrix (after 23 hours at 800 °C) and examined by XRD and SEM (figs. 3.7, 3.8).

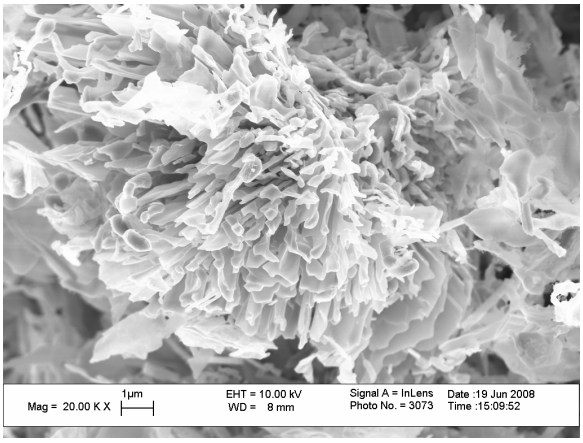

Fig. 3.7 SEM image of a precipitate extracted from the sample treated 23 hours at 800 °C

As shown in figure 3.8 the peaks were identified as the reflections of CrN (JCPDS-ICDD 11-65), Cr_2N (JCPDS-ICDD 35-803) e $Cr_{23}C_6$ (JCPDS-ICDD 35-783).

The angular positions are little shifted related to the database reflections and it can be pointed out that in the nitrides there is also the presence of the carbon. These results are in agreement with the EDX chemical line profiles on the precipitates in the transformed zone (fig. 3.5, d).

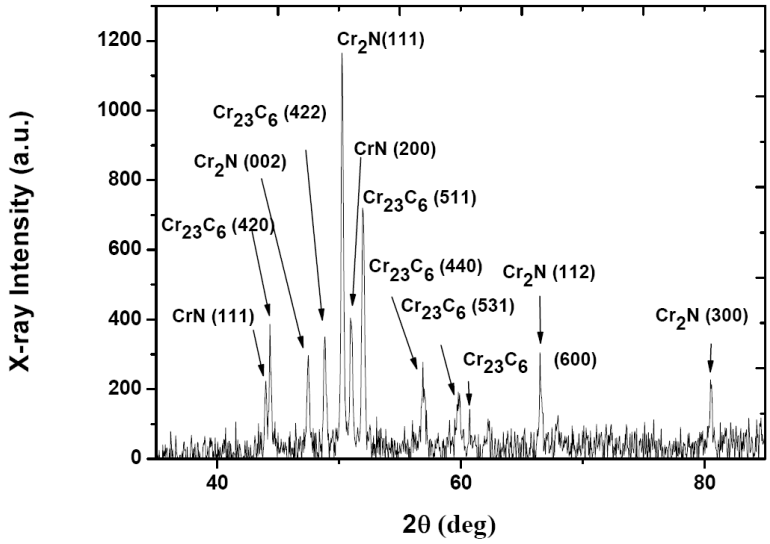

Fig. 3.8 XRD spectrum of the extracted residue from the sample treated 23 hours at 800 °C

From the XRD spectrum (fig. 3.8) it can be observed that there are not intermetallic phases in the extracted residue. However it is not an evidence of the absence of these phases in the treated steel.

It is reasonable that the phases were dissolved during the electrolytical extraction. From the scientific literature, in fact, as known that the σ phase was observed for heat treatments at 800 °C [23], but it was dissolved in a chemical solution like to the used one [52].

3.1.2.3 XRD Results

In as-prepared condition and after each heating step the samples have been analyzed by X-ray diffraction (XRD) using Co Kα radiation (λ = 1.789 Å). The spectra were collected in step-scanning mode with 2Θ steps of 0.05° and counting time of 2 s per step in the angular range of 40° - 95°. High precision peak profiles of the most intense reflections were recorded with 2Θ steps of 0.005° and counting time of 20 s per step.

The XRD spectrum of the as-prepared material shows only the presence of the nitrogen supersaturated austenitic phase γ_S (fig. 3.9). The letter *S* is refered to the sovrasaturation of interstitial nitrogen (0.8 wt%) in the not transformed matrix.

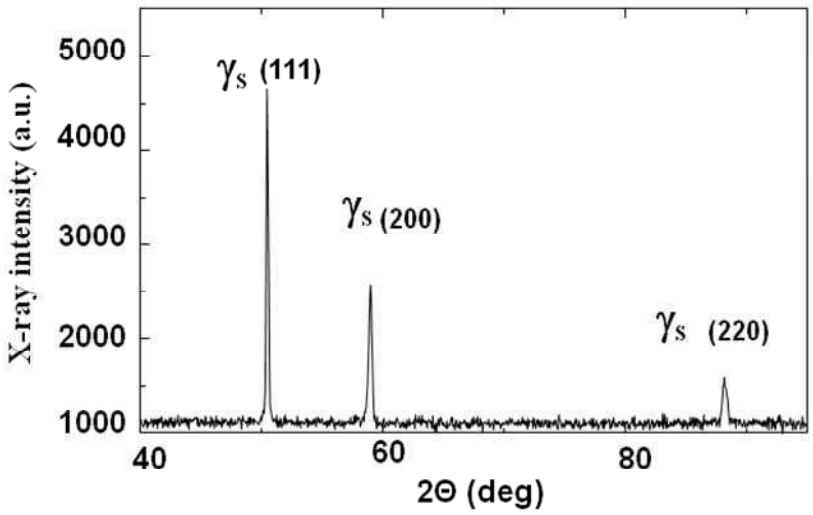

Fig. 3.9 XRD spectrum of as-prepared material

After heat treatments XRD spectrum shows a splitting of the austenite peaks indicating that a secondary γ phase has formed. For example, fig. 3.10 displays two well-separated peaks corresponding to the {111} reflections of the γ (secondary) and γ_S (supersaturated austenitic) phases.

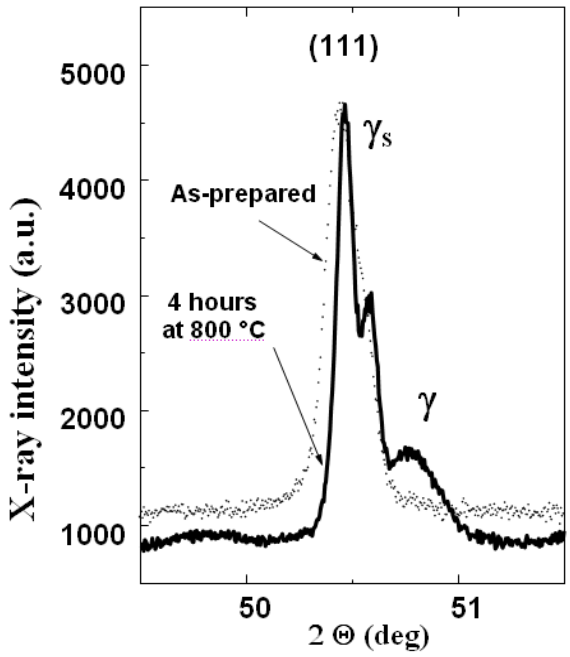

Fig. 3.10 High accuracy spectrum of the material treated 4 hours at 800 °C

For each step of treatment it was identified through a precision XRD spectrum the positions of the peaks of the two austenitic phases with increasing times. In this way it was possible to observe that the cell parameter of the secondary γ is constant with increasing time and lower than the γ_s cell parameter, while the cell parameter of the γ_s decreasing with increasing time of treatment (fig. 3.11). As shown in the tables 3.1 and 3.2 the γ_s lattice parameter values decreasing with increasing time.

This result is in agreement with the contraction of the γ_S lattice for the decreasing of the N content in solid solution. The γ phase, on the contrary, is characterized by a lower nitrogen content than γ_S, thus its unit cell is smaller and the diffraction lines are shifted to higher angles.

Table 3.1. Planes, cell parameters measured for the supersatured austenite at 800°C at different times of treatment

t (h)	2 Θ (111)	2 Θ (200)	d (111)	a (111)	d (200)	a (200)
0	50,445	58,990	2,1003	3,6378	1,8178	3,6356
3	50,470	59,020	2,0993	3,6361	1,8170	3,6340
4	50,465	58,990	2,0995	3,6364	1,8178	3,6356
8	50,500	59,025	2,0981	3,6341	1,8168	3,6337
15	50,515	59,055	2,0976	3,6331	1,8160	3,6320
23	50,520	59,100	2,0974	3,6327	1,8147	3,6295

Table 3.2. Planes, cell parameters measured for the supersatured austenite at 850°C at different times of treatment

t (h)	2 Θ (111)	2 Θ (200)	d (111)	a (111)	d (200)	a (200)
3	50,51	59,035	2,0977	3,6334	1,8166	3,6331
4	50,54	59,07	2,0966	3,6314	1,8156	3,6312
8	50,6	59,15	2,0943	3,6274	1,8133	3,6267
15	50,52	59,11	2,0974	3,6327	1,8145	3,6289
23	50,55	59,15	2,0962	3,6307	1,8133	3,6267

Considering the behaviour of the supersaturated matrix cell parameter vs. the increasing times it was possible to obtain the behaviour in figure 3.11. It is so measured that the decreasing of the γ cell parameter is higher at 850 °C than at 800°C.

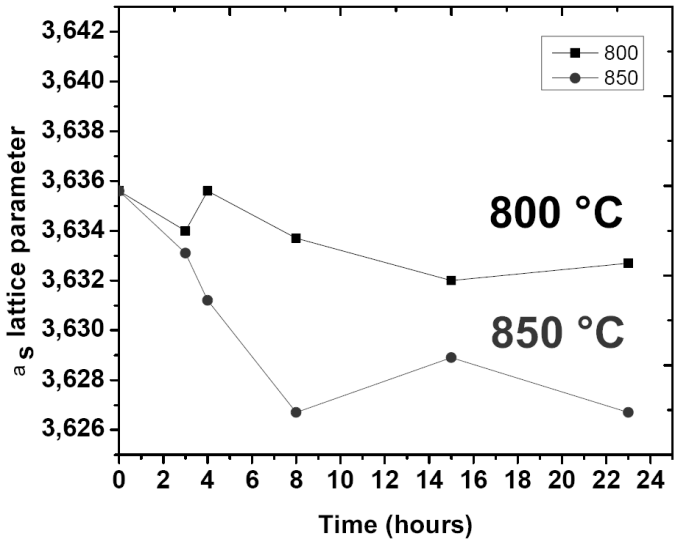

Fig. 3.11 Behaviour of the cell parameter of the supersatured austenite vs. time of treatment

The cell parameter value of the starting γ_s obtained is **3.6356 Å**. This lattice parameter, measured in the as-prepared steel, corresponds well to that obtained by the empirical equation for the HNS steel composition, (1.7) [19]:

$$a(nm) = 0.3578 + 0.00006Cr + 0.000095Mn + 0.0033C + 0.0029N \text{ (wt.\%)}.$$

that is **3.6359 Å**.

This value is also in agreement with the value of the cell parameter of the γ Iron that is **3.592 Å.**

The higher value for the HNS steel studied depends on the high concentration of solute atoms in solid solution.

The lower error to calculate the reticular parameter is at the highest angles, so for measuring the cell parameter of the secondary γ it was considered the reflection related to the plane (200) and it was obtained the value of **3.615 Å**.

Through the cell parameter of the secondary austenite it would be possible to calculate the content of nitrogen but, really, it is necessary measuring all the element content (including C concentration) in the secondary austenitic phase.

However it is possible saying reasonably that the N content must be lower than the solubility of nitrogen in iron for the composition of this HNS steel (about **0.4 wt.%** [19]).

Through XPS spatially resolved it was possible to measure an approximate N content of nitrogen in the interlamellar space (par. 3.3.2) .

It was calculated in adding the percentage amounts of the two phases in function of the steps of treatments (fig. 3.12).

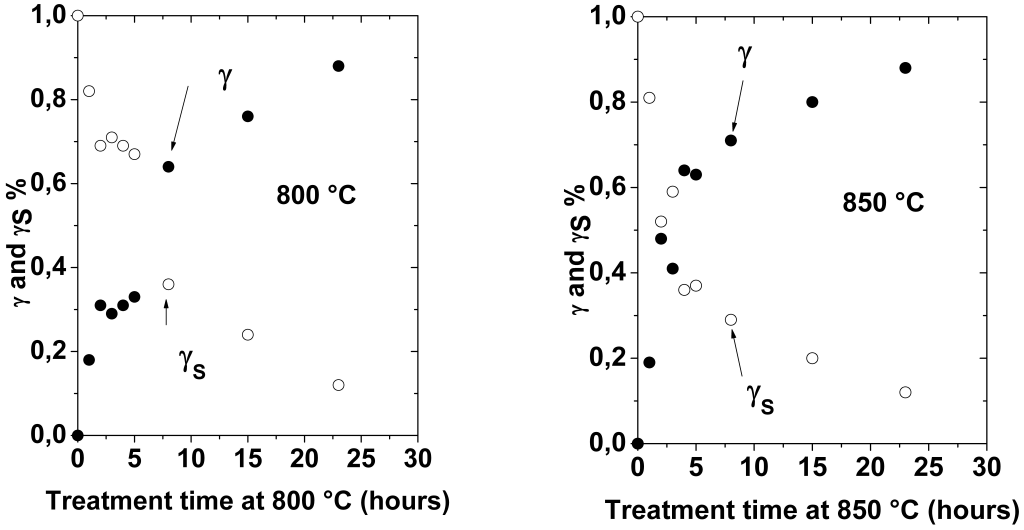

Fig. 3.12 Content of the two austenites vs. steps of treatment time at 800 and 850 °C

The γ phase appears after the first step of treatment with a period of incubation of about $3*10^3$ s, then its amount progressively increases up to ~ 90 % for the longer times of treatment. From the comparison of the curves in figs. 3.12 a), b) and table 3.3 it is clear that the transformation occurs faster at the higher temperature (850°C).

Table 3.3. Percentages of primary austenite γ_s and secondary γ vs. treatment time

T (°C)	1 hour	2 hours	3 hours	4 hours	5 hours	8 hours	15 hours	23 hours
γ_s at 800 °C	82 %	69 %	71 %	69 %	67 %	36 %	24 %	12 %
γ_s at 850 °C	81 %	52 %	59 %	36 %	37 %	29 %	20 %	12 %
γ at 800 °C	18%	31%	29%	31%	33%	64%	76%	88%
γ at 850 °C	19%	48%	61%	64%	63%	71%	80%	88%

3.1.2.4 Microhardness results

Vickers (300 g) micro-hardness tests have been carried out on the transformed and untransformed zones. The micro-hardness trend of the untransformed austenite after successive steps of treatment at 800 and 850 °C is shown in fig.3.13. The data are averaged on 20 experimental values: hardness of γ_S phase decreases as treatment time increases.

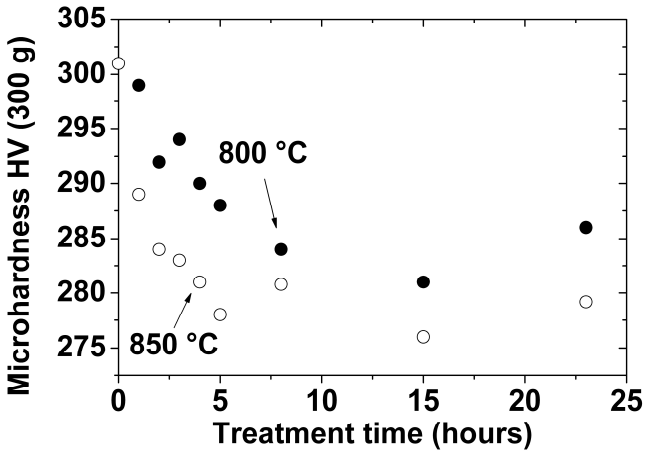

Fig. 3.13 Supersatured austenite microhardness vs. the treatment time at 800 °C and 850 °C

The transformed matrix instead shows an increasing hardness after successive treatment steps (fig. 3.14). The reason of this hardness changing with the increasing time of treatment can be researched in the hypothesis, also supported by other researchers, of the not-steady character of the cellular precipitation connected to the long range diffusion of the interstitial atoms in the HNS steels.

This phenomenon could explain the hardness behaviour as it will explain better in the following.

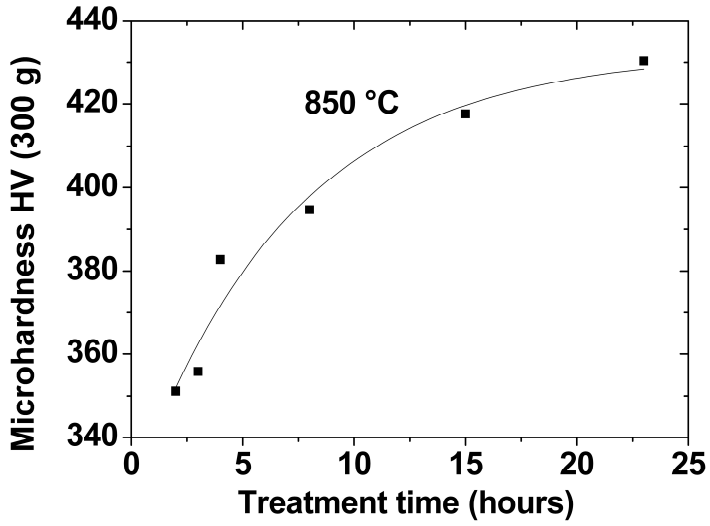

Fig. 3.14 Behaviour of the secondary austenite vs. the treatment time at 850 ° C

Nitrogen gives to a solid solution strengthening of the austenite so a lower content of N in the interstitial positions of γ_S phase could lead to a weakening of this phase; on the contrary in the transformed phase the increasing of the fraction of precipitates following successive steps of heat treatment could cause a rising of the hardness.

The progressive reduction of the hardness in γ_S phase and the increasing of the same parameter in the transformed zone could support the hypothesis of nitrogen migration from the untransformed zones to the transformed ones.

In order to verify the phenomenon of the long range migration of nitrogen, upheld also by other investigators [25,26], EDS, AES and XPS spatially resolved measurements were carried out on heat treated samples (23 hours at 850 °C).

3.2 Internal Friction results

The HNS steels material object of this study has a FCC reticulum and so it can't be characterized by Snoek relaxation peak.
In order to monitor the microstructural changes after Cr_2N precipitation verifying in addition the possibility of relaxation peaks, IF measurements were carried out [53].

IF and dynamic modulus measurements have been carried out on bar-shaped samples (13.4 x 6 x 0.26 mm^3) using the method of frequency modulation The VRA 1604 apparatus employed in [54]. Q^{-1} values have been determined from logarithmic decay of flexural vibrations. The resonance frequencies were in the range of kHz and strain amplitude was kept lower than 1 x 10^{-5}.
The samples have been heated from room temperature to 800 °C with heating rate of 1.7 x 10^{-2} °C s^{-1}. Since the modulus E is proportional to $f^{2,}$ (2.25):

$$f = \frac{m^2 h}{2\pi\sqrt{12}L^2}\sqrt{\frac{E}{\rho}}$$

its evolution vs. temperature is described by $(f/f_0)^2$ where f_0 is the initial resonance frequency at room temperature.
In eq. (2.25) m is a constant (m=1.875), L and h the length and the thickness of the sample, ρ the material density.
During each cycle (heating and cooling) of IF measurement the samples cross a temperature range (500-800 °C) where the precipitation of chromium nitrides (Cr_2N) takes place. Therefore, repeated test runs have been performed on the same samples to investigate their microstructural evolution. For example, Fig. 3.15 shows that part of the original N supersaturated austenite has transformed after five IF test runs.

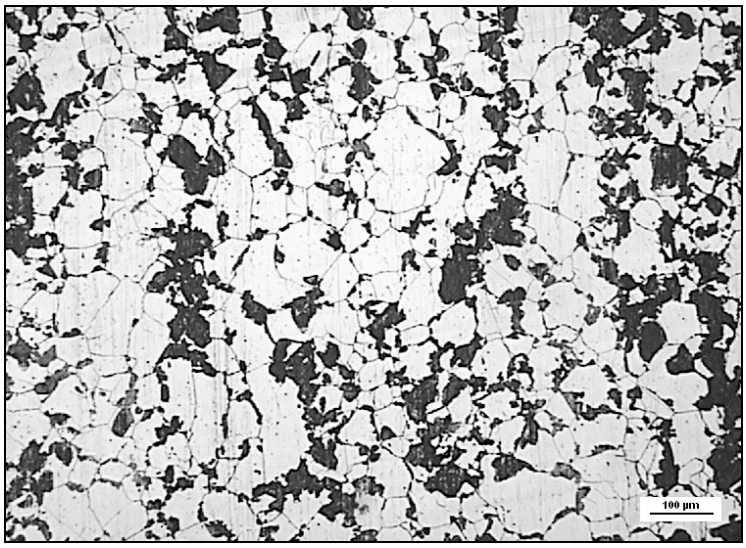

Fig.3.15 Microstructure of the steel after five cycle of internal friction

From the IF measurements carried out it was found an Internal Friction peak and the tests were repeated with two different resonance frequencies verifying that the peaks are present at two different temperatures and the values obtained are about 723 K at 760 Hz, 773 K at 1860 Hz (fig. 3.16).

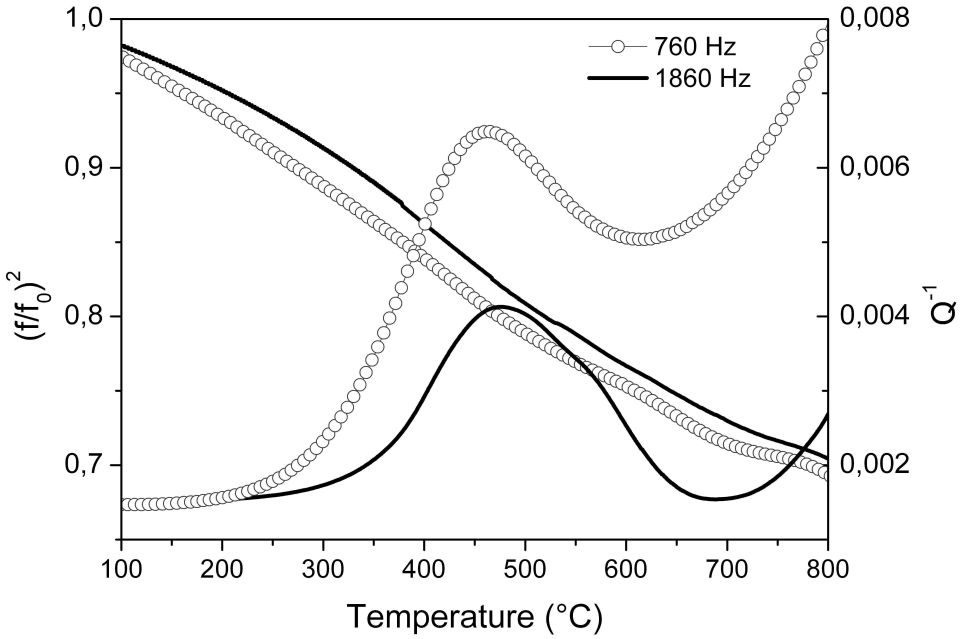

Fig.3.16 As prepared HNS steel: Q^{-1} *e di* $(f/f_0)^2$ vs. *T* trends obtained in tests with two different resonance frequencies (760 and 1860 Hz)

For a relaxation peak, the temperature of peak maximum T_P depends on the resonance frequency *f*, (2.24) :

$$\omega\tau = 2\pi f \tau_0 e^{\frac{H}{RT_P}} = 1$$

where *H* is the activation energy, *R* the gas constant. From the Arrhenius plot, *ln* $\omega\tau$ vs. $1/T_P$, the activation energy ***H* = 1.76 eV** and the relaxation time τ_0 = 2.23 x 10^{-16} s have been obtained.

The steel in as-prepared condition consists of a single N supersaturated austenitic phase and the activation energy determined is very close to that of N diffusion in γ-iron (1.74 eV [55]) and as already explained (par. 1.5) this is a feature of a **Finkelshtein- Rosin peak.**

The main substitutional elements are Cr and Mn thus both of them could form the pairs with the interstitial atoms (N and C). However, fig. 3.17 shows that the intensity of IF peak is very similar in as-prepared condition and after five runs, when a significant part of Cr has been removed from solid solution by Cr_2N precipitation. This suggests that only Mn atoms contribute to form pairs with N and C.

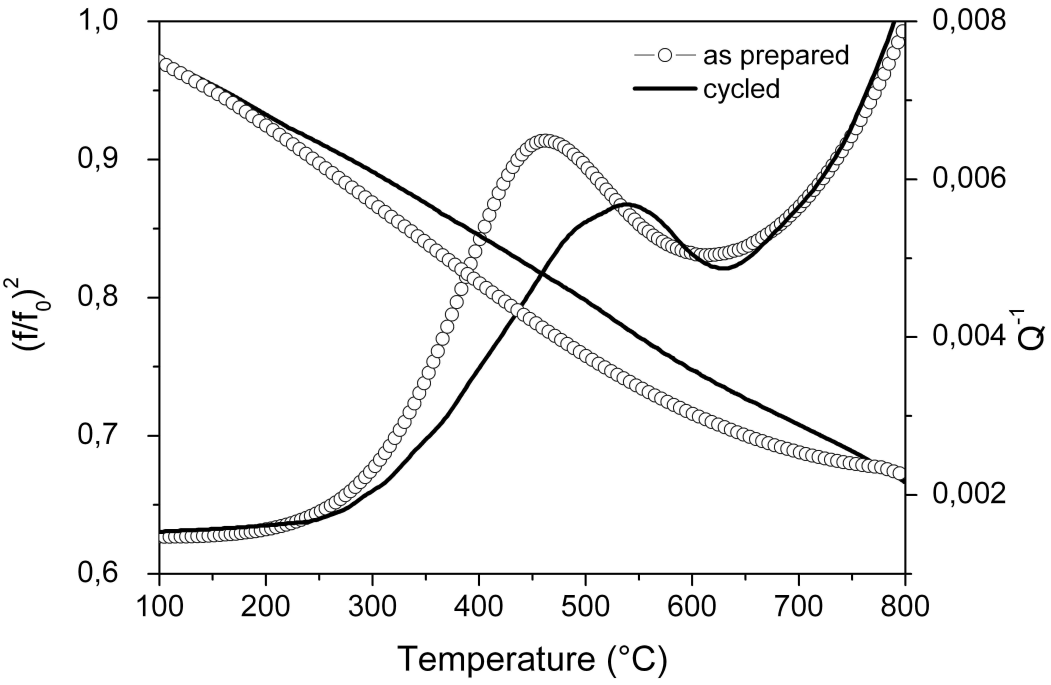

Fig.3.17 Comparing between the behaviour of $Q^{-1}$and of $(f/f_0)^2$ for the as-prepared sample and five cyclated one

On these grounds two Debye peaks due to the re-orientation of N-Mn and C-Mn pairs have been considered to fit the experimental data, after subtraction of the background. A Debye peak is described by the relationship (3.2):

$$Q^{-1}(T) = \frac{\Delta}{2}\sec h\frac{H}{R}\left(\frac{1}{T} - \frac{1}{T_P}\right) \qquad (3.2)$$

being $\Delta/2$ the peak maximum. For the the re-orientation of N-Mn pairs, H = 1.76 eV and τ_0 = 2.23 x 10^{-16} s have been taken. For the second relaxation process (re-orientation of *C-Mn* pairs) the values H =**1.50 eV** and τ_0 = 2.69 x 10^{-15} s, determined by Kê & Tsien have been assumed [43].

This attempt of fitting failed because the experimental IF peak is too wide. So, we considered that each process was characterized by a single activation energy and a discrete distribution of relaxation times $(\tau_0)_n$. This reflects changes in the environment of the species responsible for the relaxation, in particular the distribution of substitutional atoms or the presence of interstitial clusters in the neighbourhood of the i-s pairs reorienting under the external applied stress.

The central τ_0 distribution values are those used in the previous fitting, namely 2.23 x 10^{-16} s for N-Mn and 2.69 x 10^{-15} s for C-Mn. Positions and magnitudes of the remaining $(\tau_0)_n$ have been fixed to get the best fit displayed in fig. 3.18.

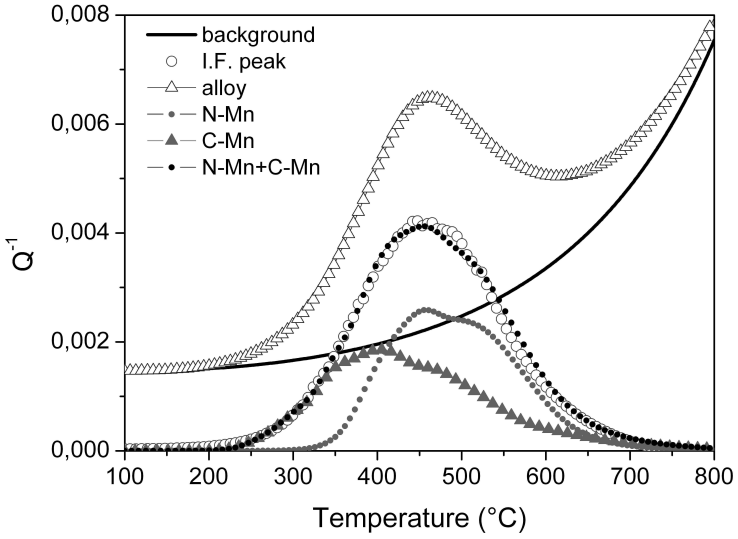

Fig.3.18 Fitting of the IF data of as-prepared steel

The distributions of relaxation times $(\tau_0)_n$, normalized to the central value, are shown in fig. 3.19 a) and b).

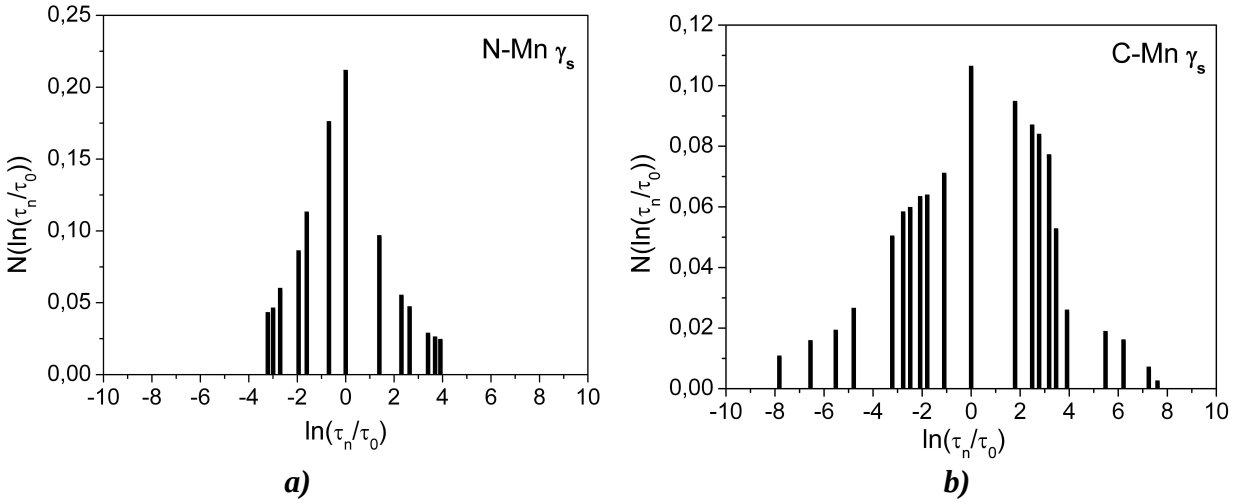

Fig.3.19 Distributions of relaxation times $(\tau_0)_n$ used to get the best fit displayed in a), b)

In the samples already submitted to IF test runs part of the material has been transformed, the transformed fraction depends on the number of runs. The reason of this change is must be connected to the precipitation of Cr_2N.

After the Cr_2N precipitation there are two austenitic phases with two different reticular parameters: the lattice parameter of the secondary austenite γ is smaller (3.615 Å) than that of the supersaturated austenite γ_S (3.6356 Å) [50].

Therefore, it is reasonable that a "new" peak shift to higher temperatures observed in cycled samples (fig. 3.15) depends on anaelastic process, namely the re-orientation of N-Mn pairs in the lattice of the secondary phase γ which is not present in the as-prepared steel (fig. 3.18). The activation energy of this process has been determined to be **1.92 eV**.

A value for the diffusion of the nitrogen was previously determined in a steel with a N wt.% concentration of 0.5 % [56] and this value is about 1.95 eV, very close to the N solubility in the Cr-Mn HNS steels [4] that is the value expected for the secondary equilibrium austenite. EDX and XPS measurements were carried out in order to know the nitrogen concentration in the secondary austenite (par. 3.3).

For the complete fitting of the cyclated material it must be considered all phenomena that generate the relaxation and so two activation energies for N-Mn pairs in γ and γ_S

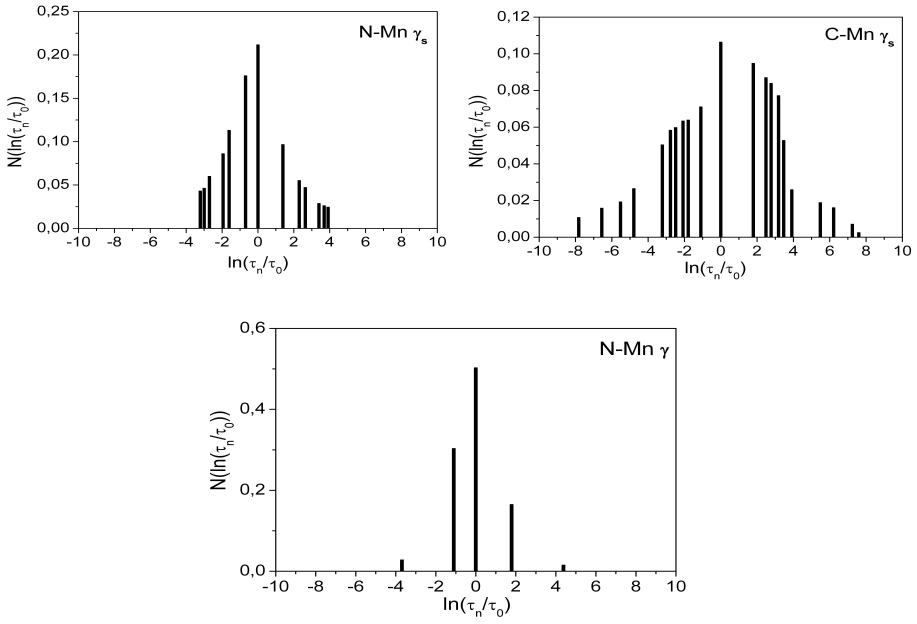

Fig.3.17 Distribution of relaxation time for the sample five runs cyclated

have been considered with the corresponding distribution of times of relaxation (fig. 3.17).

The complete fitting can be observed in figure 3.18.

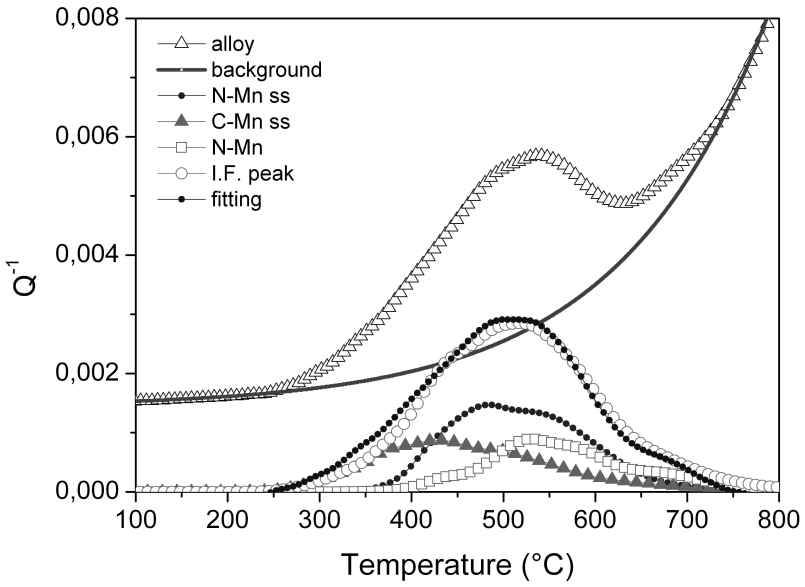

Fig.3.18 Fitting of the sample cyclated for five runs

In order to know how much austenite is transformed in the secondary phase γ image analysis was made. It was done through the *Lucia* program that shows that the transformed austenite is lower than the matrix (fig. 3.15). The fraction of γ is about 25 %.

This result is coherent with the IF behaviour in fact as can be observed in figure 3.18 the peak connected to the secondary phase is smaller than the peak of the supersaturated austenite.

3.3 XPS and Auger results

Aim of the following tests was to characterize the composition of the material after precipitation and in particular to measure the N gradient between the two zones formed after the precipitation. The sample that was analysed was treated at 850°C for 23 hours.
X-ray photoelectron and Auger spectra were collected by using an Escalab Mk II spectrometer (VG Scientific) equipped with 5-channeltron detection system. Photoelectrons were excited by using a standard Al K_α excitation source, while Auger experiments were carried out by using an electron gun LEG 200, operated at 10 keV energy and and 0.2 μm beam diameter. XPS spectra were registered at constant pass energy of 20 eV, while for AES spectra was used a constant retard ratio (1:2) analyzer mode. All these experiments were performed at a base pressure below to 1 x 10^{-10} mbar. The BE scale was calibrated by positioning the C 1s peak at 285.0 eV. Spatially resolved XPS measurements were performed at the ESCA microscopy beamline of the Elettra synchrotron in Trieste, where a scanning photoelectron microscope (SPEM) is hosted. It operates in both imaging and spectroscopy modes by using a zone plate focusing optics which produces an X-ray microprobe with a diameter of 150 nm. Photoemission spectra of selected regions and chemical maps were acquired with 0.2 eV energy resolution by using 500 eV photon energy. More details on this microscope have been reported elsewhere [57,58].

3.3.1 Auger Measurements

The Auger measurements were collected in the two different zones: untransformed and transformed one, as it can be observed in figure 3.19.

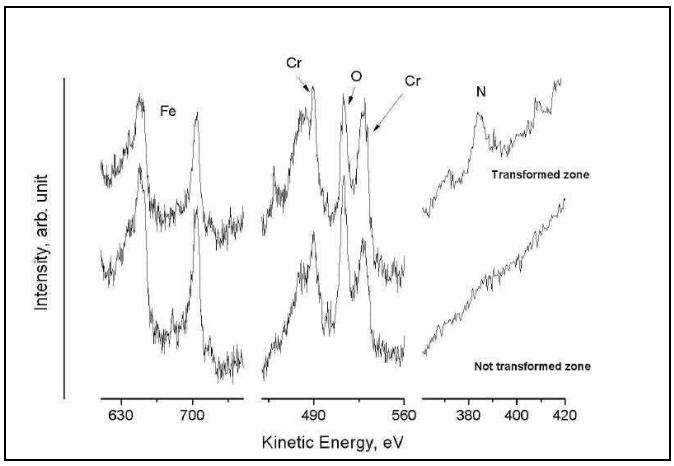

Fig. 3.19 Auger spectrum of the transformed and untransformed zones of the sample treated 23 hours at 850 °C (Fe LMM, Cr LMM, O KLL and N KLL)

From the collected spectrum it is possible a comparison between the N medium content of the transformed and untransformed zones examined. As it can be observed in figure 3.19 the N KLL peak is very weak in the untransformed zone while it is very high in the modified zone.

The calculation of Cr : N atomic ratio from Auger spectra in two different points (supersaturated and transformed zones) has also been carried out by using previous Auger measurements of CrN sample [59] as a reference for chromium and nitrogen sensitivity factors. The intensities of principal Auger peaks of Cr LMM (kinetic energy KE = 531 eV) and N KLL (KE = 389 eV) have been used in this quantification. In this way, the atomic ratios 5.9 and 2.9 were obtained for the supersaturated and transformed zones respectively. This result is a first confirmation of the nitrogen enrichment in the transformed zone: the N/Cr ratio increases to 1/3 in the transformed zone so it is not possible that there is only an equal division of N in the zones without a long range migration.

So the long range migration hypothesis supposed by Santhi Srinivas et al. [17] e Kikuchi et al. [42] is reinforced. The XRD and microhardness results also sustain this hypothesis.

However there is a difference between the theories of the two researches. For Kikuchi et al., as it will be explained (3.3.2.2.), the Cr diffusion stops the cellular precipitation, on the contrary the hypothesis sustained in this work and in agreement with Santhi Srinivas et al. is concerned with the decreasing of the gradient of nitrogen concentration with the increasing time: the cellular precipitation stops when this gradient is near to zero [60]. The hypothesis is also in agreement with the second Fick's law: the diffusion that depends on a chemical gradient stops when this gradient is deleted. Only if there is an external factor that obstructs the phenomenon the diffusion process stops before.

Auger tests were not exhaustive for demonstrating this hypothesis and so direct measurements of the N concentration were necessary.

3.3.2 EDX and XPS spatially resolved Measurements

3.3.2.1 Nitrogen concentration

The nitrogen concentration was measured in the different zones: untransformed and transformed ones and in the interlamellar distance. As already observed the

microstructure of a treated sample is characterized by the austenitic primary phase in the untransformed zone and by the secondary austenite plus Cr_2N precipitates in the transformed one.

EDX and XPS measurements were carried out in all the zones described and the results can be compared with the initial composition of the steel as related in table 3.4 and 3.5.

Table 3.4: Composition of the as-prepared sample

	Cr	Mo	Mn	C	N	Fe
wt.%	**20**	**2.5**	**17**	**0.2**	**0.8**	**59.5**
% atomic	**20.75**	**1.4**	**16.61**	**0.914**	**3.1**	**57.26**

Table 3.5: Concentration ratios related to Fe

	Cr	Mo	Mn	C	N	Fe
Solute/Fe % atomic	**0.36**	**0.024**	**0.29**	**0.016**	**0.054**	**1**

The atomic ratios related to the iron were calculated in order to make comparing with the EDX and XPS tests. The measurements were carried out on the samples treated 23 hours at 850 °C.

The figure 3.20 shows the microstructure of the sample analysed.

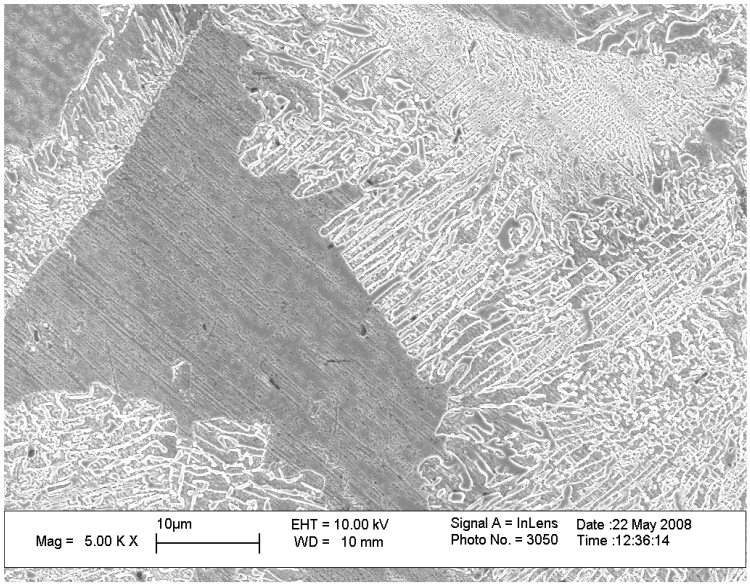

Fig.3.20 SEM image of a sample treated 23 h at 800°C: it is clear the difference between the transformed and not-transformed zones

For this analysis a Hitachi SEM was used with an analyser EDX NORAN A SYSTEM SYX and a tension of acceleration of 10.000 KV and a time of acquisition of 60 s.
Through these measurements a medium ratio of N/Fe in the untransformed matrix was calculated and it was about 0.025 (about half of the initial content of N). This ratio corresponds to a value of **0.34 wt.%.**

Table 3.6. EDS microanalysis in the not transformed zone

Element	*Net Counts*	*Weight Conc %*	*Weight % Error*	*Atom Conc %*	*Line Type*
C	369	1.67	+/-0.12	6.97	K
N	84	0.45	+/-0.23	1.61	K
O	445	1.05	+/-0.21	3.30	K
Si	357	0.42	+/-0.05	0.75	K
Cr	2707	19.16	+/-0.79	18.47	K
Mn	1458	17.03	+/-1.41	15.54	K
Fe	3535	58.38	+/-2.18	52.39	K
Mo	814	1.83	+/-0.20	0.96	L

Table 3.7. EDS microanalysis in the transformed zone

Element	*Net Counts*	*Weight Conc %*	*Weight % Error*	*Atom Conc %*	*Line Type*
C	445	1.93	+/-0.12	7.88	K
N	143	0.75	+/-0.23	2.61	K
O	493	1.13	+/-0.21	3.47	K
Mg	122	0.18	+/-0.05	0.37	K
Si	435	0.49	+/-0.05	0.86	K
Cr	2840	19.44	+/-0.50	18.34	K
Mn	1522	17.19	+/-1.39	15.34	K
Fe	3586	57.24	+/-2.17	50.28	K
Mo	758	1.64	+/-0.20	0.84	L

So it is the necessity to make other tests that confirm the decreasing in the γ matrix with the increasing time of treatment.
The other measurements were so carried out through no conventional XPS using a SPEM (photoemission spectro-microscopy) with a higher spatial resolution than the conventional XPS. In this way it was possible to obtain an analysis spot of 100 nm and it gave the possibility to analyze the N concentration in the inner parts of the transformed zone and so in the inter-lamellar space.
The image that represents where the measurements were carried out is the figure 3.21.
This is a Fe 3p chemical image and so from the brightness of the image it is possible to know where Fe is concentrated. So corresponding to the absence of the Fe (black field, point C) there is the presence of lamellae of Cr_2N.

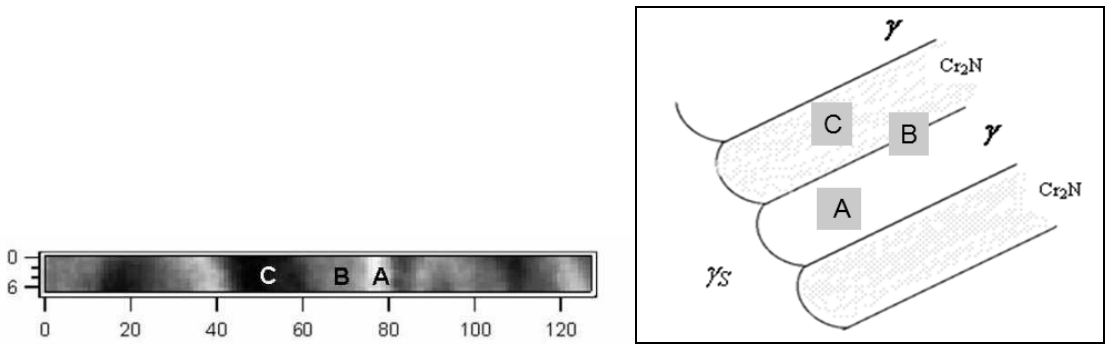

a) ***b)***

Figure 3.21. SPEM Fe 3p chemical image of the transformed zone (3.84 µm x 0.24 µm), a). Schematic structure of the transformed (lamellar) and not transformed regions (γ_s), b)

In table 3.7 are reported the values measured of the atomic ratio (related to the iron) in the interesting areas examined: A,B,C,D.

Through a comparing with the table 3.5 it is possible to know the effect of the precipitation on the composition of the steel in the different zones.

Table 3.7. XPS spatially resolved measures through SPEM

Exp	Spot Ø	Sample	Cr/Fe	Mn/Fe	N/Fe
SPEM	~0.1 µm	not transformed (D)	0.32	0.18	0.015
SPEM	~0.1 µm	transformed (A)	0.42	0.28	0.008
SPEM	~0.1 µm	transformed (C)	3.8	0.29	0.30
SPEM	~0.1 µm	transformed (B)	0.37	0.25	0.021

The table 3.7 shows that:

- The ratio N/Fe in the matrix not modified is lower (0.015) than the initial ratio N/Fe (0.054)

- the **N/Fe** average in the transformed zone is about **0.11,** higher than this ratio in the untransformed austenite (0.015).

These values are in agreement with the microanalysis results and with the initial hypothesis of the long range nitrogen migration from the untransformed to the transformed one.

The EDX and XPS results are also coherent with the limit of solubility of the N in the Cr-Mn steels. In fact for these steels the solubility of the untransformed matrix is about 0.4 wt.% in agreement with the XPS (0.22 wt%) and EDX results (0.34 wt%).

Another purpose of the XPS measurements was to verify the change of the Cr content after the exposition of the austenitic HNS steel to the temperature range of 800-850°C.

In particular the tests were carried out for verifying if the diffusion of Chromium limits the complete transformation of the steel as some researchers had supposed. For Vandeschaeve et al. [35] the cellular precipitation is incomplete because the substitutional diffusion of Cr is too low and this causes the stop of the process. This theory is supported by the presence of a nitrogen sovrasaturation in the untransformed matrix also after long time of treatment.

Related to the sovrasaturation of the nitrogen (after a treatment of 23 h at 850 ° C), as already showed by the XPS and EDX results it was not observed a N content in the untransformed austentite higher the solubility in these steels (tables 3.6, 3.7).

Moreover if the quantitative XPS data are used for calculating the reticular parameters of the austenites with the relation (1.7), [17]:

$$a(nm) = 0.3578 + 0.00006Cr + 0.000095Mn + 0.0033C + 0.0029N \text{ (wt.\%)}$$

the values obtained are in good agreement with the XRD results [50]. In fact XRD value for the austenitic phases are 3.615 Å (γ) , 3.627Å (γ_S), while with the formula (1.7) are ***a* = 3.617 Å *(γ)*** and *a* = 3.612 Å *(*γ_s).

The incongruent value of the $a_{\gamma S}$ depends probably on the XPS content of Mn (lower than the initial one) that it is still not clear. If it is used the started Mn content, the value is **3.618 Å** obtaining a more consistent result with XRD measurements. In addition it must be underlined that after long times of treatment it is very difficult to calculate the γ_S parameter because the highest peak related to the plane (111) of the secondary austenite is very close to the primary austenite one (fig. 3.22).

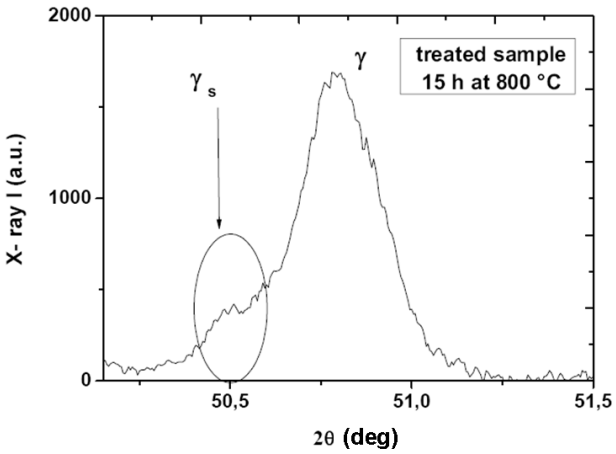

Fig.3.22 XRD high precision spectrum of the plane (111) of two austenitic phases after 15 h at 800°C

The result that it would be deepened, however, is the discrepancy between the two values of the cell austenite parameters after long times of treatment. If the content of nitrogen is close

between γ and γ_s phases, why are the parameters of the lattice on the contrary so different? One of the possible hypothesis is that together to the Chromium nitrides precipitate the Chromium carbides or carbo-nitrides and this leads to a decreasing of Carbon in solid solution that decreases the γ cell parameter (1.7). This result is supported by the analysis on the extracted residue that contains carbo-nitrides and carbides and not only nitrides (fig. 3.8).

In adding it must be underlined that the C content (0.2 wt.%) is higher than the solubility limit in these steels (0.02 wt.% [27]), and so it is possible the precipitation of carbides.

3.3.2.2 Chromium concentration

About the Cr content (calculated on the base of the SPEM results carried in table 3.7) as shown in table 3.8 that after long heat treatment time its content measured in the untransformed austenite is lower than the initial content (18 wt.% related to 20 wt.% of the as-prepared steel).

Table 3.8. Chromium, Nitrogen XPS spatially resolved concentrations in the untransformed matrix

Solute concentrations	**As prepared material**	**Untransformed matrix (D)**
Cr (% atomic)	**20 %**	**18,3 %**
N (% atomic)	**3,1 %**	**0,86 %**

This decreasing is related to the migration of Cr from the untransformed zone to the transformed one. A simple calculation shows that the hypothesis is compatible with times and temperatures of the examined heat treatments. The mean random walk Γ of Chromium can be written as:

$$\Gamma \approx (6Dt)^{1/2} \qquad (3.3)$$

where D is the diffusion coefficient of Cr in austenite and t the time of diffusion.

Being $D \cong 3 \times 10^{-17}$ m^2 s^{-1} at 850°C [35], a value of Γ = 6 μm, comparable to the grain size, is obtained for $t = 1.8 \times 10^6$ s.

The results confirm that the Cr diffusion does not compromise the complete transformation of the material and that the difference of the chemical potentials of the two austenitic phases can be the “driving force” of the transformation as supposed by Santhi Srinivas et al.

About the depletion of Cr in the transformed zone it was seen that in the interlamellar space, through the XPS spatially resolved measurements its value is not lower than the transformed zone (table 3.7). This phenomenon is in agreement with the observations of other researchers [61]. In high nitrogen stainless steels, in addition, the “Healing” phenomenon, typical for the carbon steels, was observed with the increasing treatment time at high temperature: the Cr content is not constant with increasing time but it decreases up to a minimum value in the first hours and then it begins to increase.

So it can be said that after long time of treatment at 850 °C there is not the limit concentration of Cr that sensitizes the steel. For the sensitization, in fact, it is important to remember that for austenitic stainless steels (for example 304 and 316) the limit of Cr content is around 13 wt.% [61].

Corrosion tests are necessary to verify the corrosion resistance of the steel after precipitation and the Cr concentration at the interface between the two zones.

Chemical maps were collected with the SPEM microscopy with different magnification. The figure 3.23 displays the SPEM Cr 3p image of the sample heated at 850 °C for 23 hours. The source of the contrast in the as acquired image (a) is the sum of sample topography and chemistry. When this image is corrected for sample topography (b), the main remaining contrast represents the chemical image. In the transformed zone, Cr is concentrated in the lamellae (bright features), whereas its low concentration is uniformly distributed in the untransformed (darker) regions.

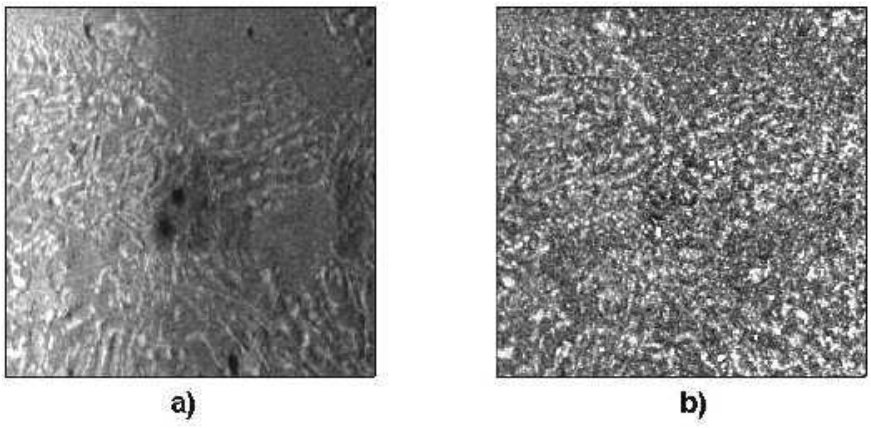

Figure 3.23. SPEM Cr 3p chemical image (51.2 µm x 51.2 µm) of the treated sample: (a) as acquired, (b) corrected for the sample topography by calculating the ratio peak/background for Cr 3p. 154x73mm (96 x 96 DPI)

The figure 3.24 shows the chemical maps of the Cr, Fe, Cr/Fe of the lamellar zone. The lamellae can be distinguished in particular if the Cr/ Fe ratio is considered, in fact the brightest zones represent the lamellae that have a clear enrichment of Cr [62].

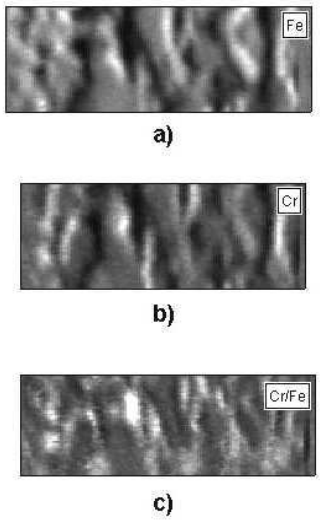

Figure 3.24. SPEM chemical maps (6.4 µm x 3.2 µm) of the transformed (lamellar) zone: Fe 3p (a), Cr 3p (b) and topographically corrected image (c) of the ratio between Cr and Fe.

Conclusions

The microstructural evolution of a high nitrogen austenitic steel, produced by PESR following successive steps of heat treatment at 800 and 850 °C up to 23 hours, has been investigated.

The results obtained through the XRD, Optical and SEM microscopy, microhardness tests and the superficial analysis (XPS, AES, spatially resolved XPS measurements) can be summarized so follows:

- The nitrogen supersaturated matrix γ_S decomposes into an austenitic secondary phase γ and Cr_2N through cellular precipitation. The γ phase is characterized by a lower nitrogen content than γ_S and its lattice parameter *a* (3.615 Å) is smaller than the initial value of γ_S (3.636 Å). After successive heating steps the parameter *a* of γ remains constant, whereas that of γ_S decreases.

- The progressive decreasing of the lattice parameter *a* and of the hardness in γ_S phase, the decreasing of the N content in the matrix not transformed (analyzed through XPS measurements) following successive steps of heat treatment, can be explained by nitrogen migration from the supersaturated γ_S phase to the transformed zones. These results support the following theory: the main force behind boundary migration is the nitrogen concentration gradient between the γ and γ_s phases. When the phases reach the same nitrogen concentration, the precipitation stops even if the transformation of the matrix has not been completed yet.

- The precipitation kinetics is faster at 850 °C and produces larger interlamellar distances in the cells.

- A migration of Chromium occurs across the interface, between not transformed and transformed zones of the steel while the super-saturation of nitrogen in the untransformed austenite was not observed for long times of treatment as supposed by by Kikuki et al..

Moreover, IF and dynamic modulus measurements have been carried out on the high nitrogen austenitic steel from room temperature to 800°C and the conclusions are the following:

- In as-prepared material the microstructure consists of a N supersaturated γ_S phase so the IF spectrum is resulted by the sum of two contributions due to the re-orientation of N-Mn and C-Mn pairs. These results are confirmed by the Activation Energies of the two relaxation processes that well agree with the Diffusion Activation Energies of nitrogen and carbon in Fe γ.

- After the first test run, when part of the material has been transformed, there are two austenitic phases γ and γ_S. Therefore, in the IF spectra of cycled samples it is necessary to consider all the contributions of the phenomena that cause the relaxation processes. Hence, there is a further contribution to IF spectra related to the as-prepared material spectrum due to the re-orientation of N-Mn pairs in the "new" γ phase.

Bibliography

[1] G.Stein, I.Hucklenbroich, H.Feichtinger, Materials Science Forum 318-320 (1999) 151-160.

[2] H.K. Feichtinger and G. Stein. – HNS98 – Materials Science Forum, 318-320 (1999) p.261.

[3] Bulletin of Alloy Phase Diagrams, Vol.8 (1987), No.4, 355.

[4] J.W.Simmons, Materials Science and Engineering A207 (1996), 159-169.

[5] H.K. Feichtinger, G. Stein, High Nitrogen Steel ’98 “Melting of high nitrogen steel”.

[6] T. Isomoto, H. Ikeda, T. Kouda, K. Ichii, T. Oishi-High Nitrogen Steel 1998, “Mechanical properties and corrosion resistance of PM high nitrogen stainless steel consolidated by hot extrusion”.

[7] F.S. Biancaniello, R.D. Jiggetts, R.E.Ricker, S.D. Ridder, “Powder Metallurgy high nitrogen stainless steel”, - High Nitrogen Steel ’98.

[8] J.Tervo, A.Tarasenko, H.Hanninen, Materials Science Forum 318-320 (1999) 41-46.

[9] Valentin G. Gavriljuk, ISIJ International, Vol. 36 (1996), No. 7, pp. 738-745.

[10] G. Saller, K. Spiradek-Hahn, C. Scheu, H. Clemens, Materials Science and Engineering A 427 (2006) 246–254.

[11] I. A. Yakubtsov, A. Ariapour and D. D. Perovic, Acta Mater. Vol. 47, No. 4, pp. 1271-1279, (1999).

[12] Andrea Carosi, Alberto Tamba Centro Sviluppo Materiali SpA, Steel Master 2002

[13] H. Hanninen, J. Romu, R. Ilola, J. Tervo, A. Laitinen, Materials Processing Technology 117 (2001) 424-430.

[14] A. Van Bennekom – Stainless Steel Word, Dic 98, “New low nichel, nitrogen containing duplex stainless steels find industrial application”.

[15] Manutenzione Tecnica e Managment Anno 9° N° 6, Giugno 2002 Editore Elsevier Thomas Italia.

[16] 4th International Conference on Launcher Technology "Space Launcher Liquid Propulsion" 3- (12-2002) Liege, (Belgium).

[17] N.C. Santhi Srinivas, V.V. Kutumbarao, Scripta Mater. Vol. 37 (1997), No. 3, p.285.

[18] F.Ruffini, O.Tassa, A.Carosi, F.Arcobello, B.Giambi, AIM 20 (2007) 11-17.

[19] Z.Z.Yuan, Q.X. Dai, X.N. Cheng, K.M.Chen, Materials Characterization 58 (2007) 87-91.

[20] J.N.Tarbaton, L.M.Matthews, A. Sutliffe, C.M.P. Frost, J.P. Wessels, Materials Science Forum 318-320 (1999) 777-784.

[21] H.K. Feichtinger, G. Stein, High Nitrogen Steel ’98 “Melting of high nitrogen steel”.

[22] A. Rechsteiner, M.O. Speidel, Innovation Stainless Steel (1993) 2107-2112 “New methods for the production of high nitrogen steels”.

[23] Tae-Ho Lee, Sung-Joon Kim and Setsuo Takaki, Metallurgical and materials transactions A 3452, Vol. 37 A (2006).

[24] Z.Z. Yuan, Q.X. Dai, X.N. Cheng, K.M. Chen, Materials Characterization 58 (2007) 87–91.

[25] T.H. Chen, J.R. Yang, Materials Science and Engineering A311 (2001) 28–41.

[26] Darlene Yuko Kobayashi, Stephan Wolynec, Materials Research 2 (1999) No. 4 239-247.

[27] T.Sourmail, Materials Science and Techology Vol. 17 (2001), 1.

[28] G. Balachandran, M. L. Bhatia, N.B. Ballal P. Krishna RAO, ISIJ International, Vol. 41 (2001), No. 9, pp. 1018–1027.

[29] Erneman, M. Schwind, P. Liu, J.-O. Nilsson, H.-O. Andren, J. Agren, Acta Materialia 52 (2004) 4337–4350 J.

[30] Q.X. Dai, Z.Z. Yuan, X.M. Luo, X.N. Cheng, Materials Science and Engineering A 385 (2004) 445–448.

[31] A.F. Padilha and P. R. Rios ISIJ International, Vol. 42 (2002), No.4, 325-337

[32] Darlene Yuko Kobayashia, Stephan Wolynec, Materials Research, Vol. 2, No. 4, 239-247, (1999).

[33] Y.Okazaki, M. Mochizuki, K. Miyahara, Y. Hosoi, Reduced Activation Materials for Fusion Reactors, ASTM STP 1047, (1990) 80-92.

[34] T.P.S. Gill, J. B. Gnanamoorthy, Journal of Materials Science 17 (1982) 1513-1518.

[35] F.Vanderschaeve, R. Taillard, J. Foct Journal of Materials Science, 30 (1995) 6035-604.

[36] M. Balbi, W. Nicodemi, “LA MECCANICA ITALIANA” n. 167 novembre 1982 Dipartimento di Chimica Fisica Applicata Politecnico di MILANO.

[37] F. Bonollo, A. Tiziani, P. Ferro la metallurgia italiana (02-2005) p.27.

[38] Yong Jun Oh, Jun Hwa Hong, J. Nucl. Mater. 278 (2000) 242.

[39] P. Shankar, H. Shaikh, S. Sivakumar, S. Venugopal, D. Sundararaman, H.S. Khatak], Journal of Nuclear Materials 264 (1999) 29-34.

[40] A. Redjaimia, A. Proult, P. Donnadieu, J. P. Morniroli, Journal of Material Science 39 (2004) 2371 – 2386.

[41] F. Shi, L.J. Wang, W.F. Cui, and C.M. Liu, Acta Metall. Sin. Vol. 20 No.2 pp 95-101 (2007).

[42] M. Kikuchi, M. Kjihara, S.Choi, Mat. Sci. Eng. A (1991), 146, 131.

[43] T.S. Kê and C.T. Tsien, Sci. Sinica, 5 (1956) 625.

[44] G. Gavriljuk et al., Scripta Materialia 37 (1997)12 1889-1894.

[45] R.M. Banov, I.M. Parshorov, Ts.S. Kamenova, (1978 a,b) Izv Acad Metalli 3:178-182, 1:126-129.

[46] M.S. Blanter, I.S. Golovin, H. Neuhauser, H.-R. Sinning (pp 28-29), Internal Friction in Metallic Materials A Handbook, Springer Series in Materials Science.

[47] Roberto Montanari, "Tecniche sperimentali per la caratterizzazione dei materiali, dal laboratorio alla produzione", AIM (2005).

[48] 85th Steelmaking Conference Proceedings, ISS-AIME, Warrendale, PA, 2002 pp. 431-452.

[49] Riccardo Donnini "Metal Matrix Composites: structure and technologies", Verlag Dr.Muller (VDM) publishing.

[**50] L. Rovatti, R. Montanari, N. Ucciardello, A. Mezzi, S. Kaciulis and A. Carosi, Materials Science Forum Vols. 638-642 (2010) pp. 3597-3602.**

[51] L. Rovatti, R. Montanari, N. Ucciardello, A. Carosi, 32° Convegno Nazionale AIM, Ferrara 2008.

[52] T.P. Gill, J. B. Gnanamoorthy, Journal of Materials Science 17 (1982) 1513-1518

[53] P. Deodati, R. Montanari, L. Rovatti, N. Ucciardello, A. Carosi, Advanced Materials Research Vols. 89-91 (2010) pp. 485-490.

[54] S. Amadori, E.G. Campari, A.L. Fiorini, R. Montanari, L. Pasquini, L. Savini, E. Bonetti, Materials Sci. & Eng., A 442 (2006) 543-546.

[55] S. Mandl, B. Rauschenbach, Journal of Applied Physics 91, No 12 (2002) 9737-9742.

[56] R.Ilola, M. Kemppainen, H. Hanninen, Materials Science Forum 318-320 (1999) 407-412.

[57] S. Gunther, B. Kaulich, L. Gregoratti, M. Kiskinova, *Prog. Surf. Sci. (*2002); *70,* 187.

[58] A.W. Potts, G.R. Morrison, L. Gregoratti, A. Barinov, B. Kaulich, M. Kiskinova, Surf. Rev.Lett. (2002) 9, 705.

[59] S. Kaciulis, A. Mezzi, G. Montesperelli, F. Lamastra, M. Rapone, F. Casadei, T. Valente, G. Gusmano, Surf. Coat. Technol. (2006) 201, 313.

[60] N.C. Santhi Srinivas, V.V. Kutumbarao, Scripta Materialia 51 (2004) 1105–1109.

[61] W. Simmons, B.S. Covino Jr., J.A. Hawk e J. S. Dunning ISIJ International. Vol, 36 (1996). No. 7. pp. 846-854.

[62] A. Carosi, L. Gregoratti, S. Kaciulis, A. Mezzi, R. Montanari, L. Rovatti, N. Ucciardello; Surface and Interface Analysis, Ecasia 2009.